Fluid-fluid displacement in porous-media microfluidics

by

Yu Qiu

B.S., Jilin University, 2018
S.M., Massachusetts Institute of Technology, 2021

Submitted to the Department of Civil and Environmental Engineering
in partial fulfillment of the requirements for the degree of

DOCTOR OF PHILOSOPHY

at the

MASSACHUSETTS INSTITUTE OF TECHNOLOGY

September 2024

© 2024 Yu Qiu. All rights reserved.

The author hereby grants to MIT a nonexclusive, worldwide, irrevocable, royalty-free license to exercise any and all rights under copyright, including to reproduce, preserve, distribute and publicly display copies of the thesis, or release the thesis under an open-access license.

Authored by:	Yu Qiu Department of Civil and Environmental Engineering August 9, 2024
Certified by:	Ruben Juanes Professor of Civil and Environmental Engineering, Professor of Earth, Atmospheric and Planetary Sciences, Thesis Supervisor
Accepted by:	Heidi Nepf Donald and Martha Harleman Professor of Civil and Environmental Engineering Chair, Graduate Program Committee

Fluid-fluid displacement in porous-media microfluidics

by

Yu Qiu

Submitted to the Department of Civil and Environmental Engineering
on August 9, 2024, in partial fulfillment of the
requirements for the degree of
Doctor of Philosophy

Abstract

Immiscible fluid-fluid displacement under geometric confinement is a key physical process in large-scale subsurface energy technologies such as geologic carbon sequestration and in small-scale microfluidic techniques. Research over the past few decades has provided improved understanding of the fluid-fluid displacement patterns on the macroscopic scale, which range from compact displacement to fractal pattern. Many questions remain, however, regarding how the macroscopic displacement patterns are controlled by the microscale interactions between the fluid interface and the solid surface in systems under geometric confinement like microfluidic devices and porous media. This fluid-solid interaction—exacerbated by the roughness inherent to all natural and engineered surfaces—introduces a large energy dissipation near the solid boundary that challenges our ability to interpret laboratory experiments and develop mathematical models.

In Part I of this Thesis, we study the motion of a fluid-fluid interface at the scale of a single capillary through mathematical modeling and laboratory experiments. We first develop a phase-field model to simulate two-phase flow with moving contact lines in the partial wetting regime. We construct a self-consistent formulation of fluid-solid surface energy which allows prescribing arbitrary static contact angles. We then propose a formulation to account for nonequilibrium conditions near the contact line and demonstrate the ability of our model to simulate dynamic configurations, from spontaneous imbibition to wetting transition and interface pinch-off.

We then experimentally study the shape of a moving interface in a capillary tube prewetted with the invading liquid. For viscously favorable displacements (when the invading fluid is more viscous than the defending fluid), we find a universal behavior of the dynamic contact angle—a macroscopic descriptor of interface shape—which increases monotonically with capillary number. In contrast, for viscously unfavorable displacements, we observe a sharp wetting transition where the dynamic contact angle shoots to 180° over a narrow range of flow rates. Above the transition, a trailing film of viscous defending fluid is left behind the displacement front and the invading fluid propagates along the tube center as a finger. We rationalize the emergence of this sharp, trailing-film type of wetting transition by means of a minimal-ingredients

hydrodynamic theory that exhibits bifurcated solutions.

In Part II of this Thesis, we investigate the role of surface roughness on two-phase displacements. We do so in a microfluidic device with a precisely controlled structured surface as an analogue for a rough fracture. In the drainage regime, we show that the roughness induces two types of liquid films entrained on the solid surfaces behind the displacement front: the classical Bretherton "thick film", and a new type of "thin film" that is confined within the roughness. Each type of liquid film is characterized by distinct stability criteria and dewetting dynamics. In the imbibition regime, we show that surface roughness promotes that the wetting liquid preferentially advances within the roughness layer. The formation of a leading film stabilizes the displacement front as the flow rate increases, which would otherwise—that is, in a smooth confinement—become fractal. In summary, our work sheds light on the microscale physics and macroscopic pattern formation in rough confinement that may control long-term mixing and reactivity in geological systems and lab-on-a-chip applications.

Thesis Supervisor: Ruben Juanes
Title: Professor of Civil and Environmental Engineering

Acknowledgments

Completing this PhD thesis has been a long and challenging journey, and I owe its realization to the contributions of numerous individuals who have supported and inspired me along the way.

First of all, I would like to express my deepest gratitude to my advisor, Professor Ruben Juanes. He provided me with the invaluable opportunity to pursue my graduate studies at MIT and has consistently shown me support, kindness, and patience over the past six years. He always encourages me to lead my own projects and pursue ambitious intellectual challenges, but lifts me up when I am low and lost. Without his mentorship, I would not be the person I am today, both professionally and personally. Ruben will continue to be a role model in my future academic life, prioritizing his students' growth and well-being over research output or metrics.

My sincere gratitude goes to my thesis committee members, Professor Lydia Bourouiba, Professor Gareth McKinley, and Professor Ching-Yao Lai, for their time and continuous support. The inspiring comments and suggestions in my annual research meetings have significantly enriched the quality of my thesis.

My heartfelt appreciation goes to my mentors and collaborators, Amir Pahlavan, Bauyrzhan Primkulov, Luis Cueto-Felgueroso, and Ke Xu, whose generosity in sharing knowledge and ideas has been invaluable. Amir has been helping me throughout the whole PhD thesis and showing me the wonderful world of fluid dynamics with a good sense of humor. Bauyrzhan's contributions to my experimental work and his unwavering emotional support have been truly instrumental. He has been one of the kindest people I have ever met. Luis provided valuable technical help on the phase-field model development. This project would not have progressed smoothly without the weekly meetings with him. Ke helped with my first project on microfluidics and patiently explained many basic concepts at the beginning of my study at MIT.

I am also indebted to the members of the Juanes Research Group, past and present, for their friendship, encouragement, and many great memories shared over Friday lunches (specifically, Hawaii Pizza), tea breaks, and conference travels. I am

particularly grateful to have shared this special journey with Bauyrzhan Primkulov (again), Maryam Alghannam, Luis Salo, Rebecca Liyanange, and Hannah Lu, who have become my lifelong friends.

In addition, I am grateful to my friends Haoran Cai, Ruijiao Sun, Baichuan Mo, and Huanhuan Tian for their companion and the joy they brought to my time at MIT. I started playing badminton two years ago and am very fortunate to have made wonderful friends there: Yuelai Wang, Quincy Kuang, Haoheng Tang, Qifan Yu, and Kaihua Liu. Their patience, kindness and athleticism not only improved my badminton techniques but also helped me survive the periodic stress of research and study.

Last but not least, I would like to thank my parents, Wu Qiu and Xianfang He, for their endless love, support, and everything they have done to give me a better life. I explore the world on their shoulders, and this thesis is dedicated to them.

Contents

List of Figures

Chapter 1

Introduction

Immiscible fluid-fluid displacement in porous media is a key physical process in many natural phenomena and industrial applications, ranging from geologic carbon sequestration (Szulczewski *et al.*, 2012; Krevor *et al.*, 2023) to water infiltration in soil (Hill & Parlange, 1972; Cueto-Felgueroso & Juanes, 2008; DiCarlo, 2013), and microfluidics (Stone *et al.*, 2004; Whitesides, 2006). Predicting and controlling these processes require a thorough understanding of the fluid-fluid displacement mechanisms and patterns on both macroscopic and microscopic scales.

The classic study of pattern formation during two-phase displacement dates back to the Saffman-Taylor instability observed in Hele-Shaw cells consisting of two parallel plates that are separated by a thin layer (Saffman & Taylor, 1958). This instability refers to the formation of viscous fingers — preferential flow paths for the invading fluid — when a less viscous fluid displacements a more viscous fluid. The Hele-Shaw cells preserves the similarity of fluid flow equations but greatly reduces the complexity of geometry compared with real porous media. As a consequence, extensive research has focused on characterizing viscous fingering in Hele-Shaw cells, exploring factors such as fluid properties (Lindner *et al.*, 2002; Bischofberger *et al.*, 2014; Zhang *et al.*, 2023), electric fields (Mirzadeh & Bazant, 2017; Gao *et al.*, 2019*b*), geometric gradients (Al-Housseiny *et al.*, 2012; Zheng *et al.*, 2015), and solid elasticity (Pihler-Puzović *et al.*, 2012; Juel *et al.*, 2018).

A fundamental study of fluid-fluid displacement in porous media led to what we

now know as the Lenormand diagram using micromodels made of interconnected capillaries (Lenormand *et al.*, 1988). Through network modeling and laboratory experiments, Lenormand *et al.* (1988) classified the displacement patterns as stable displacement, viscous fingering and capillary fingering depending on the competition between viscous forces and capillary forces. Such micromodels more closely mimic real porous media geometry and allow for a more detailed investigation of displacement regimes

So far, those previous studies have provided us with a fairly good understanding of the fluid-fluid displacement patterns on the macroscopic scale but predominantly assume complete fluid displacement at the scale of a single pore (Lenormand *et al.*, 1988; Cieplak & Robbins, 1988, 1990; Holtzman & Segre, 2015). In the presence of moving contact lines where fluid interface meets solid surface, however, the pore-scale displacements could be incomplete with the formation of films consisting of either invading phase or defending phase (Levaché & Bartolo, 2014; Zhao *et al.*, 2016; Odier *et al.*, 2017; Zhao *et al.*, 2018). The microscale complexities lead to a wealth of pattern formation regimes, which are evident in a recent phase diagram of fluid-fluid displacements in quasi-2D microfluidics (Zhao *et al.*, 2016).

Many questions still remain regarding how the macroscopic displacement patterns are controlled by the microscale interactions between the fluid interface and the solid surface in systems under geometric confinement like microfluidic devices and porous media. This fluid-solid interaction—exacerbated by the roughness inherent to all natural and engineered surfaces—continues to challenge our ability to interpret laboratory experiments and develop mathematical models.

Part I of this Thesis targets the physics of fluid-fluid displacement on the microscale, conceptualized as a single capillary tube. The fluid displacement in a capillary tube is a classic problem in fluid mechanics that has attracted vast experimental, theoretical and modeling efforts for decades (Bretherton, 1961; Hoffman, 1975; Huh & Mason, 1977; Zhou & Sheng, 1990; Zhao *et al.*, 2018; Ruiz-Gutiérrez *et al.*, 2022). Here, the presence of moving contact lines offers complex dynamics that are not yet fully understood.

In Chapter 2, we present a phase-field model to study two-phase displacement with moving contact lines in a capillary tube. We construct a diffuse-interface formulation of solid-liquid surface energy by enforcing a consistent structure of the fluid-fluid interface between the bulk fluid and the solid surface. We first show, via simulation of equilibrium liquid slugs in a capillary tube, that this formulation allows prescribing arbitrary static contact angles. We then propose a formulation to account for out-of-equilibrium near the contact line and demonstrate the ability of this generalized formulation to simulate spontaneous imbibition as well as viscously unstable, constant-rate displacements in a capillary tube. We show that our phase-field model captures the imbibition dynamics described by a theoretical model that combines classic Lucas-Washburn theory with Cox's law of dynamic contact angle. It also predicts wetting transition, thin-film formation and interface pinch-off that quantitatively agree with hydrodynamic theories and experiments. This chapter has been submitted for publication as a research article.

In Chapter 3, we experimentally study the shape of a moving interface in a capillary tube prewetted with the invading liquid. For viscously favorable displacements where the invading fluid is more viscous than the defending fluid, we find a universal behavior of the dynamic contact angle—a macroscopic descriptor of interface shape—which increases monotonically with capillary number under different prewetting layer thickness and fluid's viscosity. In contrast, for viscously unfavorable displacements, we observe a sharp wetting transition where the dynamic contact angle abruptly jumps to 180° at a critical flow rate. Above the transition, a trailing film of viscous defending fluid is left behind the displacement front and the invading fluid propagates along the tube center as a finger. We rationalize the emergence of this sharp, trailing-film type of wetting transition by means of a minimal-ingredients hydrodynamic theory that exhibits bifurcated solutions. Our work demonstrates that, in a confined geometry with smooth surface, the wetting transition universally occurs via deformation of the interface and trailing film formation, which resolves the conflicting views existing in current literature (Hoffman, 1975; Levaché & Bartolo, 2014; Zhao *et al.*, 2018). This chapter is being prepared for publication as a research article.

Part II of this Thesis investigates the influence of surface roughness on fluid-fluid displacement patterns in confined geometries. Most previous research has focused on viscously favorable displacements—viscous liquid invading air—and has shown that the presence of surface roughness leads to statistically anomalous features of advancing front including kinetic roughening and avalanches (Queralt-Martín *et al.*, 2011; Soriano *et al.*, 2002; Geromichalos *et al.*, 2002). However, the role of roughness on viscously unfavorable fluid-fluid displacement has been much less studied and is currently not well understood. Here, we conduct laboratory experiments on patterned microfluidic cells with a precisely controlled structured surface to elucidate the fundamental role of surface roughness on two-phase displacement in confined geometries.

In Chapter 4, we study the drainage regime where the invading phase is less wetting to the solid substrate than the defending phase. In contrast to the better-understood case of smooth confinement, we show that surface roughness induces two types of liquid films entrained on the solid surfaces behind the displacement front: the classical Bretherton "thick film", and a new type of "thin film" that is confined within the roughness. The thin films may be discontinuous or remain energetically stable depending on the degree of roughness. We delineate these distinct displacement regimes—complete displacement, thin-film (unstable, dewetting, stable), and thick-film—in the form of a phase diagram and explain theoretically the cross-overs among the regimes. We then show that the different hydrodynamic regimes lead to different late-time morphologies of the undisplaced (trapped) defending fluid. This chapter appeared as a research article in *PNAS* (Qiu *et al.*, 2023).

In Chapter 5, we study the imbibition regime where the invading phase is more wetting to the solid substrate than the defending phase. We show that surface roughness promotes that the wetting liquid preferentially advances within the roughness layer. The formation of a leading film stabilizes the displacement front as the flow rate increases, which would otherwise—that is, in a smooth confinement—become fractal. Our work demonstrates the powerful control of the interplay between wetting and roughness on the pattern formation in rough confinement, which may influence long-term mixing and reactivity in geological systems and lab-on-a-chip applications.

This chapter is being prepared for publication as a research article.

Part I

Moving interfaces and contact lines in a capillary tube

Chapter 2

Phase-field modeling of two-phase displacement in a capillary tube

Abstract

We present a phase-field model to study two-phase displacement with moving contact lines in a capillary tube. We construct a diffuse-interface formulation of solid-liquid surface energy by enforcing a consistent structure of the fluid-fluid interface between the bulk fluid and the solid surface. We first show, via simulation of equilibrium liquid slugs in a capillary tube, that this formulation allows prescribing arbitrary static contact angles. We then propose a formulation to account for out-of-equilibrium near the contact line and demonstrate the ability of this generalized formulation to simulate spontaneous imbibition as well as viscously unstable, constant-rate displacements in a capillary tube. We show that our phase-field model captures the imbibition dynamics described by a theoretical model that combines classic Lucas-Washburn theory with Cox's law of dynamic contact angle. It also predicts wetting transition, thin-film formation and interface pinch-off that quantitatively agree with hydrodynamic theories and experiments.

2.1 Introduction

The displacement of one fluid by another immiscible fluid in a capillary tube is a classic problem in fluid mechanics that has attracted vast experimental, theoretical and modeling efforts for decades (Bretherton, 1961; Hoffman, 1975; Huh & Mason, 1977; Zhou & Sheng, 1990; Zhao *et al.*, 2018; Ruiz-Gutiérrez *et al.*, 2022). This flow

geometry is directly relevant for technological applications like microfluidics (Stone *et al.*, 2004; Whitesides, 2006), and is key to understanding the formation of complex patterns in porous media (Saffman & Taylor, 1958; Paterson, 1981; Måløy *et al.*, 1985; Lenormand *et al.*, 1983, 1988; Levaché & Bartolo, 2014; Zhao *et al.*, 2016). Immiscible two-phase flow in a capillary tube involves a moving contact line, where the fluid-fluid interface meets the solid substrate. Moving contact lines are associated with a stress singularity due to no slip boundary condition (Huh & Scriven, 1971; Qian *et al.*, 2004; Pahlavan *et al.*, 2015). The dynamics of contact lines plays an essential role in the description of two-phase flow, from spontaneous imbibition (Delannoy *et al.*, 2019; Primkulov *et al.*, 2020*a*; Ruiz-Gutiérrez *et al.*, 2022) to forced displacement (Zhou & Sheng, 1990; Ledesma-Aguilar *et al.*, 2013; Zhao *et al.*, 2018).

In the context of spontaneous imbibition, the pioneering work by Bell & Cameron (1906), Lucas (1918) and Washburn (1921) studied the penetration of a liquid into a dry tube with circular cross-section. By balancing a constant capillary force with the viscous resistance force in the invading phase, the meniscus position $z(t)$ was found to behave similarly to a diffusive front, advancing in time according to a square root scaling. However, many experiments have demonstrated that the classic Lucas-Washburn theory overestimates the imbibition rate (Siebold *et al.*, 2000; Wu *et al.*, 2017; Delannoy *et al.*, 2019; Ruiz-Gutiérrez *et al.*, 2022). This is because the apparent contact angle (see the schematic in Fig. 2-1), which quantifies the shape of advancing interface at a macroscopic scale, would deviate from its equilibrium value and change with the contact-line speed (Siebold *et al.*, 2000; Popescu *et al.*, 2008; Ruiz-Gutiérrez *et al.*, 2022).

In the context of forced displacement, the apparent contact angle has been shown to increase with flow rate up to π (Hoffman, 1975, 1983; Fermigier & Jenffer, 1991). This critical threshold triggers a wetting transition above which films of the defending fluid may be left behind on the solid wall (Snoeijer & Andreotti, 2013). Most of the work on dynamic wetting transition has focused on unconfined systems, such as when a plate is withdrawn from a liquid bath (Eggers, 2004, 2005; Snoeijer *et al.*, 2006; Chan *et al.*, 2012). Recently the study of wetting transition has been extended

to confined geometries (Levaché & Bartolo, 2014; Zhao *et al.*, 2018): Levaché & Bartolo (2014) revisited the Saffman-Taylor instability in a Hele-Shaw cell, while Zhao *et al.* (2018) conducted a series of constant-rate displacement experiments in capillary tubes. The latter work shows that, beyond the wetting transition, the advancing interface becomes unstable and forms a finger that advances along the center of the tube while thin films of the viscous defending fluid are deposited on the tube wall. This fingering instability is different from viscous fingering in Hele-Shaw cells introduced by Saffman & Taylor (1958): the viscous thin films later dewet on the substrates, which leads to the pinch-off of the interface and the formation of disconnected bubbles and droplets (Zhao *et al.*, 2018; Pahlavan *et al.*, 2019; Gao *et al.*, 2019*a*; Esmaeilzadeh *et al.*, 2020; Giefer *et al.*, 2023). These findings may have significant implications for the predictive modeling of fluid-fluid displacement in geometric confinement.

Several computational approaches have been developed to model two-phase flow with moving contact lines in a capillary tube, including lattice/particle-based methods such as the lattice Boltzmann method (Fan *et al.*, 2001; Kang *et al.*, 2004; Latva-Kokko & Rothman, 2005, 2007; Yan & Zu, 2007; Akai *et al.*, 2018) and sharp-interface methods that solve the continuum equations for the fluid flow (e.g. the Navier-Stokes equations) at the macroscopic scale and employ contact-line models in the vicinity of contact lines (Spelt, 2005; Sui *et al.*, 2014; Zhang & Yue, 2020; Esmaeilzadeh *et al.*, 2020; Giefer *et al.*, 2023). Alternatively, diffuse-interface models have emerged as a promising tool to simulate complex interfacial behaviors of two-phase flow (Jacqmin, 1999, 2000; Yue *et al.*, 2010; Yue & Feng, 2011; Gao *et al.*, 2019*a*; Prokopev *et al.*, 2019). Here, the fluid-fluid interface is treated as a diffuse layer of finite thickness over which the fluid properties vary continuously. The main advantages of diffuse-interface methods include: (1) topological changes of an interface, like pinch-off and reconnection, are naturally handled by the solutions of the governing equations without the need of interface-regularization techniques, as those required in sharp-interface methods (Anderson *et al.*, 1998; Kim, 2005; Giefer *et al.*, 2023); (2) the motion of contact lines takes place via higher-order diffusional flux across the interface, which resolves

the stress singularity even with traditional no-slip boundary condition (Jacqmin, 2000; Meakin & Tartakovsky, 2009; Yue & Feng, 2011; Sui *et al.*, 2014; Pahlavan *et al.*, 2015, 2018).

Whether a phase-field model produces the correct macroscopic configurations of two-phase displacement hinges on the appropriate formulation of the wetting boundary condition. Specifically, two issues remain to be explored: (1) how to prescribe the static contact angle, (2) how to represent nonequilibrium behaviors near contact lines.

The surface energy based approach is commonly used to prescribe the static (equilibrium) contact angle θ_e. Its theoretical foundation stems from the work by Cahn (1977), where the interactions between solids and fluids are assumed to be sufficiently short-ranged, so that the contribution to the free energy depends only on the order parameter ϕ near the solid surface, as $f_w(\phi)$. Seppecher (1996) further related the solid-liquid surface energy $f_w(\phi)$ to the solid-liquid surface tension that ultimately determines the static contact angle θ_e via Young's equation. However, the formulation of $f_w(\phi)$ remained unspecified: Cahn (1977) only graphically analyzed the influence of f_w on critical point wetting by drawing its qualitative structure, while Seppecher (1996) used a geometric boundary condition and back-extracted the θ_e by imposing zero velocity in the simulations. Since then, models have constructed the function $f_w(\phi)$ by smooth interpolation from the constraints that, in the bulk phases, f_w should equal the solid-fluid surface tension. Mathematically, these constraints are insufficient to uniquely determine the function $f(\phi)$. Multiple expressions have been used in the literature including linear interpolation (Briant *et al.*, 2004; Briant & Yeomans, 2004; Kusumaatmaja & Yeomans, 2007), cubic interpolation (Jacqmin, 2000; Carlson *et al.*, 2009; Yue & Feng, 2011; Gao *et al.*, 2019*a*), a 5th-order polynomial form (Ben Said *et al.*, 2014; Diewald *et al.*, 2017), a sine function (Qian *et al.*, 2006; Wang *et al.*, 2008), and a hyperbolic tangent function (Huang *et al.*, 2022). None of these surface energy functions guarantee producing the correct capillary pressure across the fluid-fluid interface, even at equilibrium.

The second issue related to the wetting boundary condition concerns the nonequi-

librium behaviors, including dynamic contact angle, wetting transition and interface pinch-off that are closely related to the motion of a contact line. One commonly used boundary condition in phase-field simulations has assumed local equilibrium that the fluid-fluid interface near the contact line always follows the equilibrium configuration (Jacqmin, 1999; Ding & Spelt, 2007; Yue *et al.*, 2010; Gao *et al.*, 2019*a*). For example, Gao *et al.* (2019*a*) used the equilibrium formulation to simulate forced dewetting in a capillary tube and compared with the theoretical calculation by Eggers (2004) that employed the Navier slip model. The direct match can be obtained only if an unrealistically large slip length is given, which leads to an overestimated transition threshold in their phase-field simulations (Gao *et al.*, 2019*a*).

Instead of enforcing a local equilibrium on the solid surface, Jacqmin (1999, 2000) introduced a nonequilibrium boundary condition that allows the fluid-fluid interface to deviate from the equilibrium configuration at the contact line. The deviation is controlled by the relaxation rate of the surface chemical potential $\mathcal{W}$. Qian *et al.* (2003, 2004) showed that this nonequilibrium formulation leads to a localized slip region where the slip velocity obeys a power-law decay as a function of the distance from the contact line. Using molecular-scale simulations of Couette flow, they showed that the interfacial and velocity profiles from the phase-field simulations can be matched with those from molecular dynamics (MD) simulations by extracting phase-field model parameters from MD. The theoretical foundation of the nonequilibrium boundary condition was then cast in the framework of Onsager's principle of minimum energy dissipation (Qian *et al.*, 2008). In the macroscale simulations, Carlson *et al.* (2009, 2011) pointed out that the nonequillibrium boundary condition is essential to capture the dynamics of rapid droplet spreading in strong wetting regimes where the equilibrium formulation fails. Yue & Feng (2011) later proposed a mechanism of such relaxation near contact lines to generate a microscopic contact angle that deviates from its static equilibrium value, providing an extra tunable parameter to fit the simulated dynamic contact angles with experimental data. However, this nonequilibrium boundary condition has not been explored in simulations of spontaneous imbibition as well as wetting transition and interface pinch-off where the system is far from

equilibrium.

In addition to the surface relaxation rate, two additional phenomenological parameters in the phase-field model need to be properly chosen: interface thickness ϵ and mobility M, which control the rate of higher-order diffusion. In a physical fluid-fluid system, $\epsilon \sim 10^{-9}$ m and $M \sim 10^{-17}$ m^3 s kg^{-1}(Jacqmin, 2000; Magaletti *et al.*, 2013). This scale of parameter values is not affordable in computations for a macroscale system. Instead, much larger values of ϵ and M are often used. It is thus important to evaluate whether the phase-field simulation results for a macroscopic system depend on the model parameters ϵ and M. Scaling arguments (Yue *et al.*, 2010; Kusumaatmaja *et al.*, 2016) and asymptotic analysis (Magaletti *et al.*, 2013) suggest that the mobility has to be chosen proportional to the square of interface thickness $M \propto \epsilon^2$. However, the prefactor of this scaling is not universal, and the model parameters have to be specified according to the simulated physical setting.

In this work, we develop a phase-field model that addresses the aforementioned two issues of wetting boundary conditions and provides practical simulations for two-phase displacements in a capillary tube. We construct the solid-liquid surface energy $f_w(\phi)$ by enforcing the consistency of the internal structure of the fluid-fluid interface from the bulk down to solid surface at equilibrium. The resulting formulation of f_w incorporates the descriptions of bulk energy density and higher-order stiffness function that weights the energy gradients. We illustrate the ability of this self-consistent formulation to prescribe an arbitrary static contact angle through the simulation of equilibrium configurations of a liquid slug. Comparing it with interpolated formulations, we show that a lack of consistency in the internal structure leads to non-physical contact line behavior and incorrect capillary pressure. Furthermore, we showcase its generalization to other complex two-phase systems through the simulations of polymer mixture described by nonconstant higher-order stiffness (de Gennes, 1980).

We then demonstrate the ability of our model to capture the dynamics of spontaneous imbibition, by comparing the simulation results with a theoretical model that combines Lucas-Washburn theory with Cox law which is validated against experiments in Wu *et al.* (2017). While decreasing bulk mobility slows the imbibition

dynamics towards the theoretical prediction, its selection is bounded by the interface width ϵ for the convergence to the sharp-interface limit. We propose to use a nonequilibrium formulation on the solid walls to resolve the mismatch between phase-field simulations and theoretical predictions, where the surface relaxation rate is shown to control the slip near the contact line

We further demonstrate the importance of accounting for a nonequilibrium boundary condition by means of simulations of viscously unstable constant-rate displacement. As the capillary number increases, the phase-field model produces an increasing apparent contact angle that follows the Cox law (Cox, 1986). At a critical threshold, the apparent contact angle reaches π, triggering a wetting transition. This threshold, when simulated by our model with nonequilibrium boundary condition, agrees with the well-established hydrodynamic theory used in Zhao *et al.* (2018), an agreement that cannot be achieved using an equilibrium condition. Our model shows that, beyond the wetting transition, a thin film of viscous defending liquid forms on the tube walls, the thickness of which agrees with the extended Bretherton law (Klaseboer *et al.*, 2014). The thin film dewets on the tube wall, with a fluid rim forming and growing in the vicinity of the moving contact lines, which finally leads to interface pinch-off under geometric confinement. Our simulations, with nonequilibrium boundary condition, capture the flow behavior inside the thin film and produce the rim height growing with 1/5 power-law scaling in time, in accordance with the theory recently established in Pahlavan *et al.* (2019).

An outline of the paper is as follows. In section 2, we describe the thermodynamic framework with focus on the construction of solid-liquid surface energy $f_w(\phi)$, introduce the governing equations and discuss the details of the numerical simulations. In section 3, we show the simulations of equilibrium liquid slugs. In section 4, we show the phase-field simulations of spontaneous imbibition, which achieves a good match with theoretical predictions using nonequilibrium boundary condition. In section 5, we show the simulations of constant-rate displacements with nonequilibrium formulation and compare the numerical simulations with hydrodynamic theories.

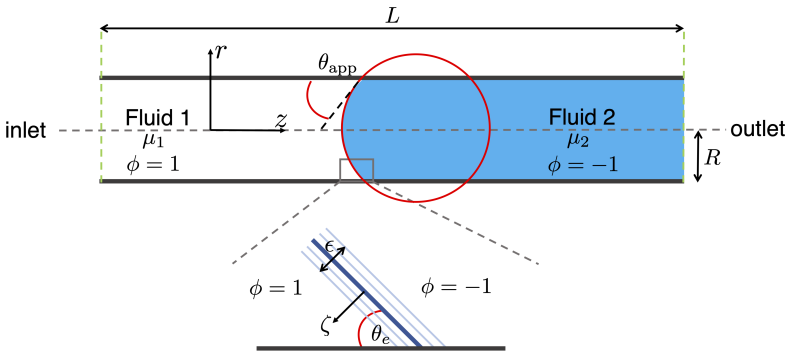

Figure 2-1: Phase-field model setup to simulate two-phase displacements in a capillary tube.

2.2 Mathematical model

2.2.1 Diffuse-interface description

We consider two immiscible fluids in a capillary tube, as is shown in Fig. 2-1. We introduce the order parameter ϕ to denote fluid 1 ($\phi = 1$) and fluid 2 ($\phi = -1$). These two fluids are separated by an interface with finite thickness ϵ, over which the fluids are mixed and ϕ varies continuously. The free energy functional of such system is expressed as: (Seppecher, 1996; Jacqmin, 1999, 2000):

$$\mathcal{F}(\phi, \nabla\phi) = \int_\Omega \left[f(\phi) + \frac{\kappa(\phi)}{2} |\nabla\phi|^2 \right] dV + \int_{\partial\Omega} f_w(\phi) dS, \tag{2.1}$$

where Ω is the fluid domain and $\partial\Omega$ is the solid-fluid surface.

The volume integral term in Eq. (2.1) represents the free energy of nonuniform binary fluids, proposed by Cahn & Hilliard (1958). It accounts for both short-ranged and long-ranged intermolecular forces, which are approximated to depend on the local composition and composition gradient respectively. The bulk energy density $f(\phi)$ has two minima at $\phi = \pm 1$ that models the existence of two stable fluid phases. We will take the standard double-well form for the calculations in our study $f(\phi) = \frac{\lambda}{4}(1-\phi)^2(1+\phi)^2$, where λ is the energy per unit volume. The *higher-order stiffness* $\kappa(\phi)$ that weights the gradient term determines the energy cost of creating and maintaining the fluid-fluid interfaces (Cueto-Felgueroso & Juanes, 2012, 2014; Benzi *et al.*, 2011;

Cirillo *et al.*, 2016; Pahlavan *et al.*, 2015, 2018). In general, it could be an non-constant that depends on the order parameter (Cahn & Hilliard, 1958; de Gennes, 1980; Benzi *et al.*, 2011). In the standard model for simple binary mixtures, stiffness is a positive constant (Cahn & Hilliard, 1958):

$$\kappa = \lambda\epsilon^2. \tag{2.2}$$

We will use this constant form throughout the simulations in this paper, while an non-constant form will be used in section 2.3.3 to illustrate the ability of our model to simulate other complex fluid systems.

The surface integral term in Eq. (2.1) represents the solid-liquid surface energy. As proposed by Cahn (1977), the interactions between solid and liquid are assumed to be sufficiently short-ranged, so that the contribution to the free energy of the surface only depends on the order parameter as $f_w(\phi)$. The original work by Cahn (1977) graphically analyzed the influence of f_w on critical point wetting, but did not give an explicit expression for it. In the following subsection, we will derive a generalized formulation of solid-fluid surface energy given arbitrary $f(\phi)$ and $\kappa(\phi)$.

The variation of the total free energy (Eq. (2.1)) with respect to the order parameter, $\delta\mathcal{F}/\delta\phi$, leads to two quantities: the bulk chemical potential

$$\mathcal{G} = \frac{df(\phi)}{d\phi} - \sqrt{\kappa(\phi)}\nabla\cdot(\sqrt{\kappa(\phi)}\nabla\phi), \tag{2.3}$$

and surface chemical potential

$$\mathcal{L} = \frac{df_w(\phi)}{d\phi} + \mathbf{n}\cdot(\kappa(\phi)\nabla\phi). \tag{2.4}$$

where $\mathbf{n}$ points outward normal to the tube wall. The equilibrium configuration of this system exists at energy minimization with $\mathcal{L} = 0$ and $\mathcal{G} =$ constant (Jacqmin, 2000). Here we take $\mathcal{G} = 0$. Given that the interfacial thickness is much smaller than the radius of the curved fluid-fluid interface, Eq. (2.3) may be reduced to the

dimension across the interface in the local coordinate whose origin aligns with $\phi = 0$:

$$\frac{df(\phi)}{d\phi} = \sqrt{\kappa(\phi)}\frac{d}{d\zeta}\left(\sqrt{\kappa(\phi)}\frac{d\phi}{d\zeta}\right), \tag{2.5}$$

where ζ denotes the axis normal to the interface (Fig. 2-1, bottom). Multiplying both sides by $d\phi/d\zeta$ and rearranging, this nonlinear second-order differential equation can be written as:

$$\frac{d\phi}{d\zeta} = \sqrt{\frac{2f(\phi)}{\kappa(\phi)}}, \tag{2.6}$$

the solution of which, $\phi(\zeta)$, gives the internal structure of the fluid-fluid interface at equilibrium.

The fluid-fluid interfacial tension can be evaluated as the excess free energy due to the gradient of ϕ in the interfacial region (Cahn & Hilliard, 1958):

$$\gamma = \int_{-\infty}^{\infty}\left[\frac{1}{2}\kappa(\phi)\Big(\frac{d\phi}{d\zeta}\Big)^2\right]d\zeta, \tag{2.7}$$

through which the parameter λ in Eq. (2.2) is related to γ.

2.2.2 Formulation of the solid-fluid surface energy

At equilibrium, where $\mathcal{L} = 0$, we rewrite Eq. (2.4) as:

$$df_w/d\phi = -\kappa(\phi)\mathbf{n}\cdot\nabla\phi. \tag{2.8}$$

We require that the microscopic contact angle near contact line is always equal to the imposed static value, which leads to the geometric condition:

$$\mathbf{n}\cdot\nabla\phi = \cos\theta_e|\nabla\phi|. \tag{2.9}$$

To ensure the consistency between the fluid-fluid interface structure on the solid surface and that in the bulk, we require that the term $|\nabla\phi|$ to be evaluated using the equilibrium solution in Eq. (2.6). Combining Eq. (2.8) and Eq. (2.9), we arrive at an

expression for the derivative of the solid-fluid interface energy :

$$\frac{df_w}{d\phi} = -\sqrt{2\kappa(\phi)f(\phi)}\cos\theta_e. \tag{2.10}$$

We integrate Eq. (2.10) to obtain $f_w(\phi)$. Here, the constant of integration is evaluated using the energy constraint that, in the bulk phase, f_w should represent the solid-liquid surface energy γ_{s1} for fluid 1 ($\phi = 1$) and γ_{s2} for fluid 2 ($\phi = -1$). Using Young's equation, $\gamma_{s2} - \gamma_{s1} = \gamma\cos\theta_e$, we obtain the liquid-solid energy density as:

$$f_w(\phi) = -\int \left(\sqrt{2f(\phi)\kappa(\phi)}\cos\theta_e\right)d\phi + \frac{\gamma_{s1}+\gamma_{s2}}{2}. \tag{2.11}$$

We note that the formulation of $f_w(\phi)$ is determined by the bulk energy density $f(\phi)$ and stiffness $\kappa(\phi)$ together.

2.2.3 Governing equations

Mass balance leads to the advective Cahn-Hilliard equation that governs the spatial-temporal distribution of ϕ:

$$\frac{\partial\phi}{\partial t} + \mathbf{u}\cdot\nabla\phi - M\nabla^2\mathcal{G} = 0, \tag{2.12}$$

where M is the mobility, assumed to be constant. The transport equation (2.12) describes the interface motion simultaneously driven by the convection under an external velocity field and the diffusion due to the gradient of a chemical potential, the rate of which is controlled by M. The velocity field $\mathbf{u}$ is the solution of the continuity equation and Navier-Stokes equation, given respectively as:

$$\nabla\cdot\mathbf{u} = 0, \tag{2.13}$$

$$\rho\left(\frac{\partial\mathbf{u}}{\partial t} + \mathbf{u}\cdot\nabla\mathbf{u}\right) = -\nabla P + \nabla\cdot\left[\mu\left(\nabla\mathbf{u} + (\nabla\mathbf{u})^T\right)\right] - \mathcal{G}\nabla\phi, \tag{2.14}$$

where P is the pressure field and μ is the dynamic viscosity. The last term $\mathcal{G}\nabla\phi$ is the continuum representation of the capillary effects, which is a local stress proportional to surface tension and interface curvature in hydrodynamic models (Jasnow & Vinals, 1996; Verschueren *et al.*, 2001). The density of the two liquids are assumed to be equal and fixed as $\rho = 10^3$ kg/m^3. The viscosity is assumed to vary linearly with the order parameter:

$$\mu = \mu_1 \frac{\phi + 1}{2} - \mu_2 \frac{\phi - 1}{2}. \tag{2.15}$$

2.2.4 Boundary conditions on the solid wall

We impose a no-slip and no-penetration boundary condition on the solid walls such that the contact line motion is only driven by the higher-order diffusion across the interface:

$$\mathbf{u} = \mathbf{0}. \tag{2.16}$$

Zero normal diffusive flux across the solid wall is used to ensure mass conservation of the fluids:

$$\mathbf{n} \cdot \nabla\mathcal{G} = 0. \tag{2.17}$$

To prescribe the contact angles, we use the surface-energy based approach that accounts for the nonequilibrium near contact lines (Jacqmin, 1999, 2000; Yue & Feng, 2011; Carlson *et al.*, 2009):

$$\frac{\partial\phi}{\partial t} = \mathcal{W}\left[\frac{df_w(\phi)}{d\phi} + \mathbf{n} \cdot (\kappa(\phi)\nabla\phi)\right], \tag{2.18}$$

where $\mathcal{W}$ is a phenomenological parameter that controls the relaxation rate of surface chemical potential. This nonequilibrium condition allows for the establishment of a local structure of fluid-fluid interface on the solid surface (Carlson *et al.*, 2009). A larger value of $\mathcal{W}$ leads to faster relaxation of the interface to its equilibrium configuration. As $\mathcal{W}$ increases to infinity, Eq. (2.18) reduces to the classic equilibrium condition. We note that the equilibrium structure, described by θ_e, is related to the solid-fluid interface energy function $f_w(\phi)$. Given a finite $\mathcal{W}$, this nonequilibrium

formulation may lead to a contact angle that deviates from θ_e on the solid wall. In our study, we aim to understand the influence of this parameter on the behavior of two-phase displacement in a capillary tube, especially on those far from equilibrium like wetting transition and interface pinch-off.

2.2.5 Nondimensionalization and model implementation

We nondimensionalize the governing equations as follows:

$$\begin{aligned} &\tilde{\mathbf{u}} = \mathbf{u}/U_c, \quad \tilde{t} = t/T_c, \quad \tilde{r} = r/R, \quad \tilde{z} = z/R, \\ &\tilde{\kappa} = \kappa/\lambda\epsilon^2, \quad \tilde{P} = PR^2/\mu_1 U_c L, \quad \tilde{f}_w = f_w/\gamma, \end{aligned} \tag{2.19}$$

where U_c is the characteristic velocity that will be prescribed for each physical setting investigated in the following sections; $T_c = L/U_c$ is the characteristic time required for the fluid to be convected through the tube; the characteristic length is the tube radius R; the characteristic pressure is $P_v = \mu_1 U_c L/R^2$. Dropping the tildes, the governing equations become:

$$\mathcal{G} = (\phi^2 - 1)\phi - \mathrm{Cn}^2\sqrt{\kappa(\phi)}\nabla\cdot(\sqrt{\kappa(\phi)}\nabla\phi), \tag{2.20}$$

$$\frac{\partial\phi}{\partial t} + l_a\left(\mathbf{u}\cdot\nabla\phi\right) - \frac{l_m^2 l_a}{\mathrm{CaCn}}\nabla^2\mathcal{G} = 0, \tag{2.21}$$

$$\nabla\cdot\mathbf{u} = 0, \tag{2.22}$$

$$\frac{\mathrm{Re}}{l_a^2}\left(\frac{\partial\mathbf{u}}{\partial t} + l_a\mathbf{u}\cdot\nabla\mathbf{u}\right) = -l_a\nabla P + \nabla\cdot\left[\bar{\mu}\left(\nabla\mathbf{u} + (\nabla\mathbf{u})^T\right)\right] - \frac{1}{\mathrm{CaCn}}\mathcal{G}\nabla\phi, \tag{2.23}$$

$$\bar{\mu} = \frac{\phi+1}{2} - \eta\frac{\phi-1}{2}, \tag{2.24}$$

and the boundary conditons are written as:

$$\mathbf{u} = \mathbf{0}, \tag{2.25}$$

$$\mathbf{n}\cdot\nabla\mathcal{G} = 0, \tag{2.26}$$

$$\mathbf{n} \cdot (\kappa(\phi)\nabla\phi) = \frac{\mathrm{Ca}\ \mathcal{S}}{\mathrm{Cn}\ l_a}\frac{\partial\phi}{\partial t} - \frac{\cos\theta_e}{\mathrm{Cn}} f'_w(\phi), \tag{2.27}$$

where we have identified eight dimensionless numbers:

$$\begin{aligned}
\text{Reynolds number:} \quad & \mathrm{Re} = \rho U_c L/\mu_1 \\
\text{Viscosity ratio:} \quad & \eta = \mu_2/\mu_1 \\
\text{Capillary number:} \quad & \mathrm{Ca} = \mu_1 U_c/\gamma \\
\text{Static contact angle:} \quad & \theta_e \\
\text{Tube aspect ratio:} \quad & l_a = L/R \\
\text{Cahn number:} \quad & \mathrm{Cn} = \epsilon/R \\
\text{Diffusion length:} \quad & l_m = \sqrt{\mu_1 M}/R \\
\text{Surface relaxation time:} \quad & \mathcal{S} = (\mu_1 \mathcal{W} R)^{-1}.
\end{aligned} \tag{2.28}$$

We note that the Reynolds number is vanishingly small, $\mathrm{Re} \to 0$, given the low velocity in our system, such that Eq. (2.23) reduces to the Stokes equation as:

$$0 = -l_a \nabla P + \nabla \cdot \left[\bar{\mu}\left(\nabla\mathbf{u} + (\nabla\mathbf{u})^T\right)\right] - \frac{1}{\mathrm{CaCn}}\mathcal{G}\nabla\phi. \tag{2.29}$$

The physical parameters that could be controlled in lab experiments are [θ_e, Ca, η, l_a], the first three of which have been known to influence the interfacial configurations and displacement dynamics from hydrodynamic analysis. The remaining three [Cn, l_m, $\mathcal{S}$] are the numerical parameters that control the convergence of diffuse-interface model and contact-line velocity. Here we explore their roles on the macroscopic behaviors in each physical setting.

The axisymmetric geometry of a capillary tube allows us to reduce the dimensionality of the governing equations. The evolution equations for the order parameter (2.20) and (2.21) take the following forms, respectively:

$$\mathcal{G} = (\phi^2 - 1)\phi - \mathrm{Cn}^2\sqrt{\kappa(\phi)}\left[\frac{\sqrt{\kappa(\phi)}}{r}\frac{\partial\phi}{\partial r} + \frac{\partial}{\partial r}\left(\sqrt{\kappa(\phi)}\frac{\partial\phi}{\partial r}\right) + \frac{\partial}{\partial z}\left(\sqrt{\kappa(\phi)}\frac{\partial\phi}{\partial z}\right)\right], \tag{2.30}$$

$$\frac{\partial \phi}{\partial t} + l_a \left(u_r \frac{\partial \phi}{\partial r} + u_z \frac{\partial \phi}{\partial z} \right) - \frac{l_m^2 l_a}{\mathrm{CaCn}} \left(\frac{1}{r} \frac{\partial \mathcal{G}}{\partial r} + \frac{\partial^2 \mathcal{G}}{\partial r^2} + \frac{\partial^2 \mathcal{G}}{\partial z^2} \right) = 0, \tag{2.31}$$

which are implemented in the `General Form PDE` interface of `COMSOL Multiphysics` software along with the boundary conditions Eq. (2.17) and Eq. (2.18). The continuity equation (2.22) and momentum equation (2.29) in 2D axisymmetric form reduce to:

$$\frac{\partial u_r}{\partial r} + \frac{u_r}{r} + \frac{\partial u_z}{\partial z} = 0, \tag{2.32}$$

$$0 = -l_a \frac{\partial P}{\partial r} + \left[2 \frac{\partial}{\partial r} \left(\mu \frac{\partial u_r}{\partial r} \right) + \frac{2\mu}{r} \frac{\partial u_r}{\partial r} + \frac{\partial}{\partial z} \left(\mu \frac{\partial u_r}{\partial z} \right) + \frac{\partial}{\partial z} \left(\mu \frac{\partial u_z}{\partial r} \right) \right] - \frac{1}{\mathrm{CaCn}} \mathcal{G} \frac{\partial \phi}{\partial r}, \tag{2.33}$$

$$0 = -l_a \frac{\partial P}{\partial z} + \left[\frac{\partial}{\partial r} \left(\mu \frac{\partial u_r}{\partial z} \right) + \frac{\partial}{\partial r} \left(\mu \frac{\partial u_z}{\partial r} \right) + \frac{\mu}{r} \frac{\partial u_r}{\partial z} + \frac{\mu}{r} \frac{\partial u_z}{\partial r} + 2 \frac{\partial}{\partial z} \left(\mu \frac{\partial u_z}{\partial z} \right) \right] - \frac{1}{\mathrm{CaCn}^2} \mathcal{G} \frac{\partial \phi}{\partial z}. \tag{2.34}$$

With boundary condition Eq. (2.16) these equations are solved in the `COMSOL Creeping Flow` interface. The initial condition and boundary conditions at the tube inlet and outlet will be specified for each physical setting investigated in the following sections.

2.3 Steady-state configuration of a liquid slug

To study the effect of wetting on two-phase flow, a fundamental and practical issue is whether our model can predict the equilibrium configuration of a liquid slug that is prescribed by an arbitrary contact angle. Here we place fluid 1 (white color) inside the capillary tube surrounded by fluid 2 (black color), as is shown in Fig. 2-2A. The aspect ratio of tube length to radius l_a is 16. At the initial state, the two fluids are separated by two flat interfaces where the distribution of the phase variable is given as:

$$\phi(t=0) = -\max\{-\tanh(\frac{z - z_{0,l}}{\delta_0}), \tanh(\frac{z - z_{0,r}}{\delta_0})\}, \tag{2.35}$$

where $z_{0,l} = 4$ and $z_{0,r} = 12$ are the initial positions of the fluid-fluid interface on the left and right hand side respectively, and $\delta_0 = 2\text{Cn}$ is the initial interface thickness. We simulate the spontaneous relaxation of the interface by applying zero flux and zero pressure boundary conditions at tube inlet and outlet:

$$\nabla\phi = \mathbf{0}, \quad \nabla\mathcal{G} = \mathbf{0}, \quad P = 0. \tag{2.36}$$

The viscosity ratio is fixed as $\eta = 1/500$ and the characteristic velocity is chosen as $U_c = 1$ in this physical setting. Since this system evolves towards equilibrium, the surface relaxation time $\mathcal{S}$ and bulk diffusion length l_m do not influence the final configurations. We thus set the model parameters as $\mathcal{S} = 0$, $l_m = 0.07$ and $\text{Cn} = 0.03$.

For contact angles different from 90°, the liquid slug with such initial configuration (Fig. 2-2A) is out-of-equilibrium. In the absence of external forces, the fluid configuration gradually relaxes towards the equilibrium state where the interfaces are curved and intersect the tube walls at the prescribed equilibrium contact angle θ_e. As a result, the pressure within fluid 1 should match the value given by the Young-Laplace equation as $P_c = 2\gamma/R\cos\theta_e$.

2.3.1 Equilibrium slugs for different wettability conditions

We test the ability of our model with constant stiffness in Eq. (2.2) to prescribe arbitrary static contact angle. In this case, the explicit expression for the interfacial tension (Eq. (2.7)) is $\gamma = \frac{2\sqrt{2}\lambda}{3\epsilon}$, and the solid-liquid surface energy (Eq: (2.11)) in the dimensionless form is:

$$f_w(\phi) = \frac{\cos\theta_e}{4}(3\phi - \phi^3) + \frac{\gamma_{s1} + \gamma_{s2}}{2\gamma}. \tag{2.37}$$

Here we vary the static contact angle θ_e from 10° to 170°. Fig. 2-2B shows the equilibrium configurations for 6 wettability conditions ranging from wetting to nonwetting cases. The corresponding pressure distribution along the center of the tube is shown in Fig. 2-2C. The agreement with the theoretical P_c demonstrates that the model can

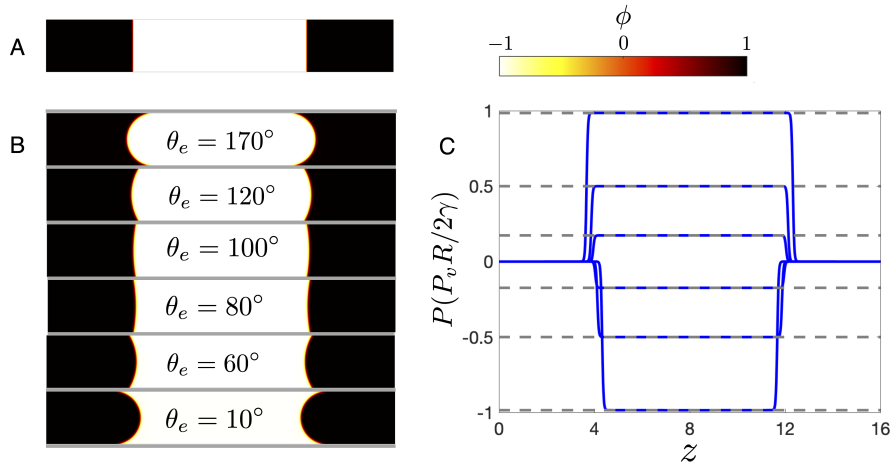

Figure 2-2: (A) Initial configuration of a liquid slug. (B) Equilibrium configurations of the liquid slug prescribed by static contact angles $\theta_e = 170°$, $120°$, $100°$, $80°$, $60°$ and $10°$. (C) The corresponding pressure distribution along the tube center line.

produce the correct capillary effects at equilibrium for arbitrarily prescribed θ_e.

2.3.2 Influence of solid-liquid surface energy formulation

In our formulation we specify the function form of the solid-liquid surface energy by enforcing the consistency between the fluid-fluid interface structure on the solid surface and that in the bulk, instead of using an arbitrary interpolation. The latter approach leads to multiple expressions that, as we will see, fail to produce the interfacial configurations. We simulate equilibrium slugs using interpolations existing in the current literature at two static contact angles: $\theta_e = 80°$ and $\theta_e = 10°$. Most of the interpolations are based on the constraints that, in the bulk phases, f_w should equal to the solid-liquid surface tension γ_{s1} and γ_{s2} respectively and the derivative $df_w/d\phi$ should vanish, which leads to expressions including the hyperbolic tangent form with scale factor k (Huang *et al.*, 2022):

$$f_w^{\tanh}(\phi) = -\frac{\gamma \cos\theta_e}{2\gamma} \tanh(k\phi) + \frac{\gamma_{s1} + \gamma_{s2}}{2\gamma}, \tag{2.38}$$

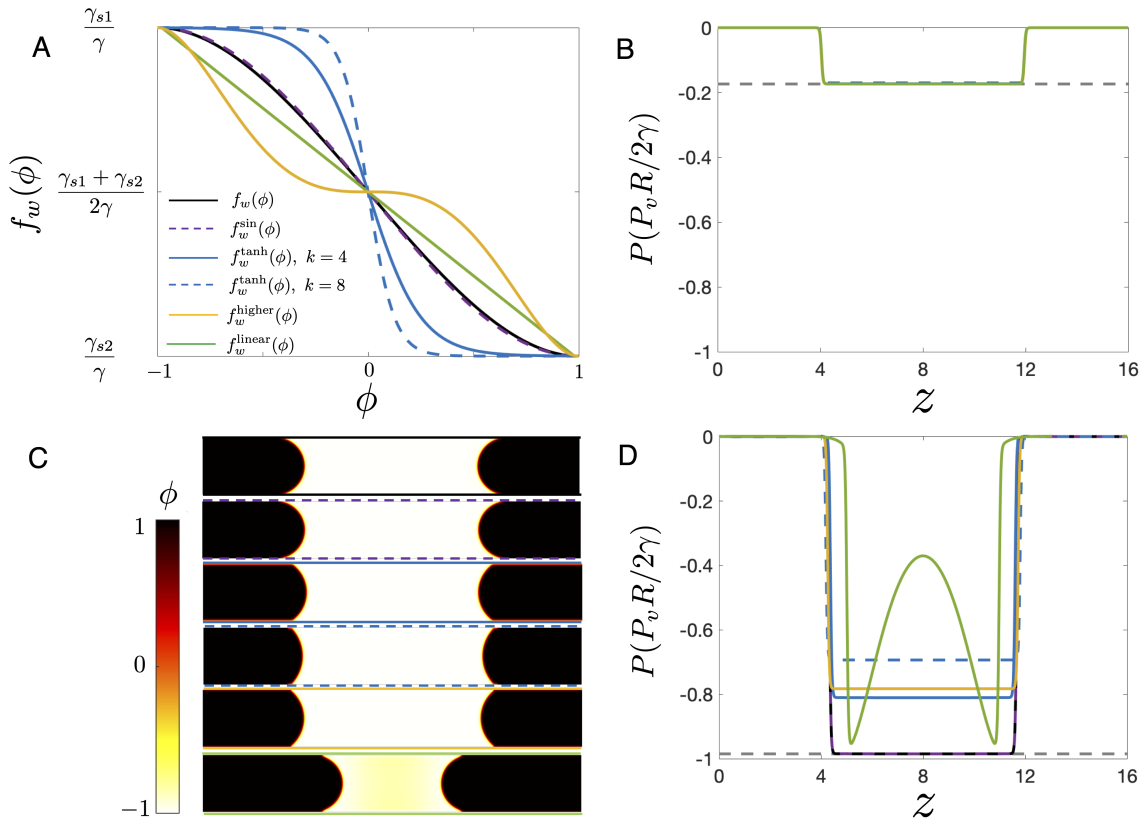

Figure 2-3: (A) Different formulations of the solid-fluid surface energy function, $f_w(\phi)$. The black solid line represents the cubic form derived in section 2.2.2 (Eq. (2.37)). The purple dashed line represents the interpolated sinusoidal function (Eq. (2.39)). The blue solid line represents the hyperbolic tangent form with scale factor 4 and the blue dashed line with scale factor 8 (Eq. (2.38)). The yellow solid line represents the fifth-order polynomial form (Eq. (2.40)). The green solid line represents the linear form (Eq. (2.41)). (B) The pressure distribution along the tube center at static contact angle $\theta_e = 80°$, simulated using the six formulations of f_w shown in (A). The gray dashed line is the theoretical P_c. (C) Equilibrium configurations of a liquid slug at $\theta_e = 10°$ from the six formulations of f_w shown in (A). The outline style of each configuration are noted in the legend of (A). (D) The pressure distribution along the tube center from the simulations in (C).

the sinusoidal form (Qian *et al.*, 2006; Wang *et al.*, 2008):

$$f_w^{\sin}(\phi) = -\frac{\cos\theta_e}{2}\sin\left(\frac{\pi}{2}\phi\right) + \frac{\gamma_{s1}+\gamma_{s2}}{2\gamma}, \tag{2.39}$$

and the 5th-order polynomial form (Ben Said *et al.*, 2014; Diewald *et al.*, 2017):

$$f_w^{\text{higher}}(\phi) = -\frac{\cos\theta_e}{4}(5\phi^5 - 3\phi^3) + \frac{\gamma_{s1}+\gamma_{s2}}{2\gamma}. \tag{2.40}$$

The other commonly-used formulation is linear form (Briant *et al.*, 2004; Briant & Yeomans, 2004; Kusumaatmaja & Yeomans, 2007):

$$f_w^{\text{linear}}(\phi) = -\frac{3\cos\theta_e}{4}\omega\phi + \frac{\gamma_{s1}+\gamma_{s2}}{2\gamma}, \tag{2.41}$$

where the constant ω is the root of the nonlinear function $\cos\theta_e = \frac{1}{2}[(1+\frac{\sqrt{2}\omega}{\lambda\epsilon})^{3/2} - (1-\frac{\sqrt{2}\omega}{\lambda\epsilon})^{3/2}]$. These interpolation functions are shown in Fig. 2-3A. The shape of sin form (Eq. (2.39)) is nearly identical to that of the derived equation (Eq. (2.37)) since the Taylor series of sin function takes the cubic form: $\sin(\phi) = \phi - \phi^3/6 + O(\phi^5)$. The tanh type of equations have sharper transition from γ_{s1} to γ_{s2}. The 5th-order polynomial form has a zero slope near $\phi = 0$. And the linear form does not satisfy the conditions that the derivative of f_w should vanish in the two bulk phases. Fig. 2-3B shows the capillary pressure along the tube center simulated using these formulations at fixed $\theta_e = 80°$. The overlapping curves indicate that all of the interpolation formulations can produce the correct capillary pressure at *weak* wetting. However, at *strong* wetting with $\theta_e = 10°$, the interpolated formulations lead to unphysical contact-line behavior (Fig. 2-3C). For the tanh function with $k = 4$ and the higher-order polynomial function, the contact line slides along the tube wall that forms a thin layer of mixtures. For the tanh with $k = 8$ and linear form, the interface is unrealistically curved near the contact line region. The linear form even causes a problem of mass conservation. These incorrect interface shapes lead to a capillary pressure that deviates significantly from the theoretical value (Fig. 2-3D).

2.3.3 Extension to complex two-phase system with non-constant higher-order stiffness

For simple liquid-liquid systems, we take the stiffness function κ in Eq. (2.2) as constant. In other situations, however, it could be a non-constant that depends on the order parameter. Examples include phase separation of polymer mixtures (de Gennes, 1980; Witelski, 1998), ultraslow relaxation and dynamical arrest of glassy systems like colloids and foams (Benzi *et al.*, 2011) and one-dimension model of liquid-gas interface in a capillary tube (Cueto-Felgueroso & Juanes, 2012). Here we borrow the form from de Gennes (1980), nondimensionalized as:

$$\kappa(\phi) = 1/(1-\phi^2), \tag{2.42}$$

to demonstrate the ability of our $f_w(\phi)$ to produce the correct equilibrium configurations for complex fluids. Given the stiffness function in Eq. (2.42), the fluid-fluid interfacial tension becomes $\frac{\pi\lambda}{2\sqrt{2}\epsilon}$, and then the dimensionless solid-liquid surface energy is written as:

$$f_w(\phi) = \frac{\cos\theta_e}{\pi}\left[\sin^{-1}(\phi) + \phi\sqrt{1-\phi^2}\right] + \frac{\gamma_{s1}+\gamma_{s2}}{2\gamma}. \tag{2.43}$$

It is neither a polynomial nor a trigonometric function that is frequently-used for interpolation. Fig. 2-4A shows that it takes a smaller slope than the one derived using constant stiffness (Eq. (2.37)). Here we simulate the equilibrium slugs governed by the non-constant stiffness using the corresponding solid-liquid surface energy function in Eq. (2.43). The results at Fig. 2-4B and C show that the model produces the correct interface shape and capillary pressure at both *weak* wetting $\theta_e = 80^\circ$ and *strong* wetting $\theta_e = 10^\circ$. However, if we do not consider the change of interface structure by stiffness function and use instead the form of f_w derived for constant stiffness, the model leads to incorrect configurations where the capillary pressure is larger than the theoretical value for a wide range of θ_e.

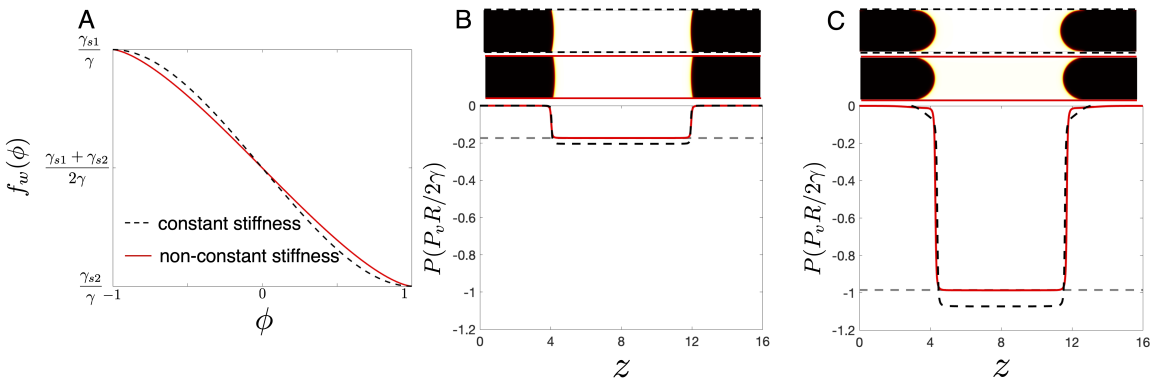

Figure 2-4: (A) Formulations of the solid-fluid surface energy function, $f_w(\phi)$, for constant stiffness (black dashed line, Eq. (2.37)) and non-constant stiffness (red solid line, Eq. (2.43)). The equilibrium configurations of complex binary fluids described by non-constant stiffness function, and the pressure distribution at static contact angles $\theta_e = 80°$ (B) and $10°$ (C).

2.4 Spontaneous imbibition

In this section, we test the ability of our model to capture the dynamics of spontaneous imbibition where a more viscous and more wetting liquid flows into a capillary tube filled with another liquid, for which a theoretical model is derived.

2.4.1 Theoretical model

We derive a one-dimensional model to describe the capillary displacement of viscous liquids with different wettability conditions θ_e and viscosity contrast η (Fig. 2-5A). By assuming Poiseuille flow, the liquid motion is driven by the viscous resistance force in the bulk of the two fluids, which is $F_v = -8\pi\mu_1 Z dZ/dT - 8\pi\mu_2(L - Z)dZ/dT$, and by the capillary force $F_c = \gamma\cos\theta_{\text{app}} 2\pi R$. Note that we account for the effect of dynamic contact angle of the advancing fluid-fluid interface via the macroscopic parameter θ_{app}, which is expected to differ from its static value θ_e at nonzero contact-line speed. In physical experiments, θ_{app} is measured by extrapolating the interface to the solid wall assuming a spherical meniscus shape (Hoffman, 1975; Fermigier & Jenffer, 1991; Primkulov *et al.*, 2020*a*). Neglecting the effect of inertia, we obtain the

equation of motion based on Newton's second law, the dimensional form of which is:

$$0 = \gamma \cos\theta_{\text{app}} \frac{2}{R} - \frac{8}{R^2}\mu_1[Z + \eta(L - Z)]\frac{dZ}{dT}. \tag{2.44}$$

On a smooth and homogeneous solid surface, the relation between apparent contact angle θ_{app} and the speed U of moving interface should follow the Cox law (Cox, 1986):

$$g(\theta_{\text{app}}, \eta) - g(\theta_e, \eta) = \frac{\mu_1 U}{\gamma} \ln\Big(\frac{R}{h_s}\Big), \tag{2.45}$$

where h_{s} is the slip length near the contact line, $U = dZ/dT$ is the advancing interface velocity and $g(\theta, \eta)$ is an algebraic function given by Cox (1986):

$$g(\theta, \eta) = \int_0^\theta \frac{\eta(\beta^2 - \sin^2\beta)(\pi - \beta + \sin\beta\cos\beta) + ((\pi - \beta)^2 - \sin^2\beta)(\beta - \sin\beta\cos\beta)}{2\sin\beta\big[\eta^2(\beta^2 - \sin^2\beta) + 2\eta(\beta(\pi - \beta) + \sin^2\beta) + (\pi - \beta)^2 - \sin^2\beta\big]} d\beta.$$

When $\eta \ll 1$, it reduces to the commonly used Cox-Voinov relation (Voinov, 1976; Cox, 1986):

$$\theta_{\text{app}}^3 - \theta_e^3 = 9\frac{\mu_1 U}{\gamma} \ln\Big(\frac{R}{h_s}\Big). \tag{2.46}$$

The initial conditions for these differential equations are $Z = Z_0$, $U = dZ/dT = 0$ and $\theta_{\text{app}} = \theta_e$. This theoretical model, which couples the classic Lucas-Washburn theory with Cox law, has been used to predict the dynamics of capillary rise by including a term of gravity force and validated against experimental measurements (Wu *et al.*, 2017). By adjusting the slip length h_s/R for different testing liquids, Wu *et al.* (2017) achieved a good match between model predictions and experimental data. Specifically, they found that, $h_s/R \approx 1 \times 10^{-5}$ provided the best match for silicone oils at very wetting condition $\theta_e \approx 10^\circ$ (Wu *et al.*, 2017). This Lucas-Washburn-Cox model has recently been extended to incorporate inertial effects (Ruiz-Gutiérrez *et al.*, 2022).

To make the equation dimensionless, we choose $U_c = \frac{P_m L}{8\mu_1}$ as the characteristic velocity, where $P_m = 2\gamma/R$ is the maximum Young-Laplace capillary pressure in a capillary tube. Consistent with the definition in Eq. (2.19), we choose the tube

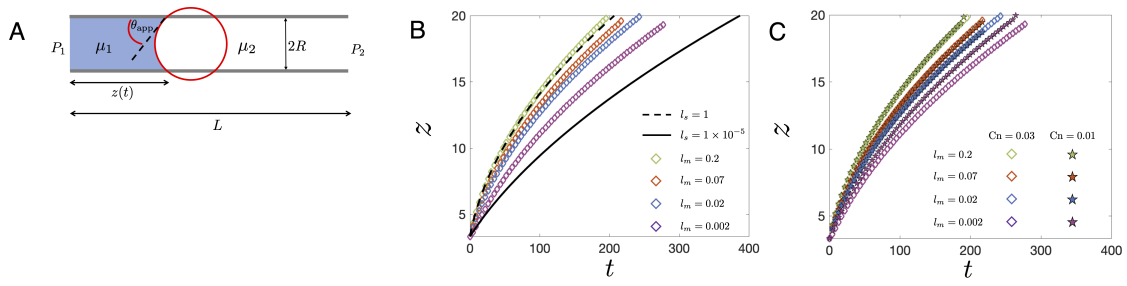

Figure 2-5: (A) Schematic of spontaneous imbibition. (B) Dashed and solid lines are the theoretical predictions from Eq. (2.49) with hydrodynamic slip length $l_s = 1$ and $l_s = 1 \times 10^{-5}$, respectively. Diamonds are the phase-field simulation results with different values of the mobility parameter l_m but fixed Cn $= 0.03$. The physical parameters are set as: static contact angle $\theta_e = 20°$, viscosity ratio $\eta = 1/1000$ and tube geometrical parameters $l_a = 20$ and $z_0 = 10/3$. (C) Influence of Cahn number on the imbibition dynamics to test the convergence to the sharp-interface limit.

radius R as the characteristic length and $t_c = L/U_c = 4\mu_1 R/\gamma$ as the characteristic invasion time for spontaneous imbibition. We then write the differential equations that govern the meniscus motion in dimensionless form:

$$0 = \cos\theta_{\text{app}} - [z + \eta(l_a - z)]\frac{dz}{dt}, \tag{2.47}$$

$$\theta_{\text{app}}^3 - \theta_e^3 = \frac{9l_a}{4}u(t)\ln(l_s^{-1}), \tag{2.48}$$

$$\frac{dz}{dt} = l_a u(t), \tag{2.49}$$

where $l_s = h_s/R$ is the dimensionless slip length. The initial conditions become $z = z_0$, $\dot{z} = u = 0$ and $\theta_{\text{app}} = \theta_e$. No analytical solution exists for this system of differential-algebraic equations (DAEs). We numerically solve them using MATLAB function `ode15i`. Fig. 2-5B compares the solution for classic Lucas-Washburn theory ($l_s = 1$, dashed line) and the one that considers dynamic contact angle ($l_s = 1 \times 10^{-5}$, solid line), with physical parameters fixed as $\eta = 1/1000$, $\theta_e = 20°$, $l_a = 20$ and $z_0 = 10/3$. We observe that the dynamic contact angle significantly slows the imbibition dynamics and delays the breakthrough time at which the invading phase fully fills the tube.

We use our phase-field model to simulate the spontaneous imbibition in a capillary tube and compare with the above-mentioned theoretical model. We assume that the

invading phase occupies a small region near the tube inlet at the initial stage. Thus the initial distribution of the phase variable is:

$$\phi(z, t = 0) = -\tanh\left(\frac{z - z_0}{\delta_0}\right), \tag{2.50}$$

where the initial position of interface is $z_0 = 10/3$. The boundary conditions at the tube inlet are:

$$P = 0, \quad \phi = 1, \tag{2.51}$$

and at tube outlet are:

$$P = 0, \quad \nabla\phi = \mathbf{0}, \quad \nabla\mathcal{G} = \mathbf{0}. \tag{2.52}$$

2.4.2 Influence of model parameters on imbibition dynamics

Among those three models parameters, the Cahn number (Cn) directly determines the computation time since the mesh size has to be at least two times smaller than the interfacial width. We fix Cn = 0.03 throughout our simulations unless otherwise specified. We note that this choice of Cn has been shown to produce the correct interface shape and capillary pressure at equilibrium in Section 2.3.

We then select an optimal bulk mobility, dimensionless as l_m, by exploring its influence on imbibition dynamics using the equilibrium boundary condition where $\mathcal{S} = 0$. Fig. 2-5 shows the simulation results for four values of l_m, with the other physical parameters being the same as those used in the theoretical model: $\theta_e = 20°$, $\eta = 1/1000$, $l_a = 20$, and $z_0 = 10/3$. Larger bulk mobility leads to faster wicking, which even overshoots the classic Washburn theory ($l_s = 1$) when $l_m \geq 0.2$. Reducing l_m slows the imbibition dynamics towards the theoretical prediction with $l_s = 1\times10^{-5}$. However, the bulk mobility cannot be infinitely small given a fixed Cn. This is because, in order to achieve the sharp-interface limit where the solution is independent of Cn, the phase-field diffusion length l_m has to be larger than the interfacial width: $l_m \geq \alpha$Cn where α is a constant (Yue *et al.*, 2010; Magaletti *et al.*, 2013). We test this sharp-interface limit by decreasing Cn from 0.03 to 0.01 while fixing l_m. The results

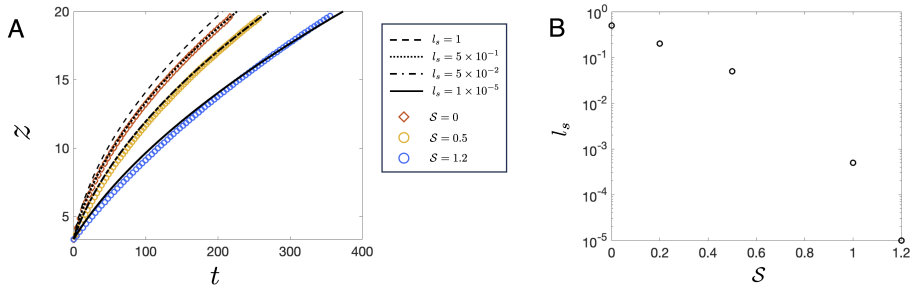

Figure 2-6: (A) Influence of surface relaxation time $\mathcal{S}$ on the imbibition dynamics, with fixed model parameters $l_m = 0.07$ and Cn $= 0.03$ and physical parameters same as those in Fig. 2-5. The black lines are the theoretical predictions from Eq. (2.49) with different hydrodynamic slip length l_s. (B) Best-fitted slip length l_s for the results produced by different $\mathcal{S}$.

are shown in Fig. 2-5C. For the smallest $l_m = 0.002$, the imbibition dynamics increases as Cn decreases, indicating the results strongly depend on Cn. While for the other three values of l_m, the solutions are invariant and the sharp-interface limit is achieved using Cn $= 0.03$. We further note that the convergence criterion for $\eta = 1/1000$ used here is consistent with the analysis in Yue *et al.* (2010) where $\alpha = 4$ is proposed.

Fig. 2-5B shows that, with equilibrium boundary condition, even the smallest mobility that converged at Cn $= 0.03$ would produce a result far from the the theoretical prediction with $l_s = 1 \times 10^{-5}$. This discrepancy has to be resolved using the nonequilibrium boundary condition.

We vary the dimensionless relaxation number $\mathcal{S}$ from 0 to 10 while keeping the mobility unchanged as $l_m = 0.07$. As is shown in Fig. 2-6A, the influence of $\mathcal{S}$ on the imbibition dynamics is much stronger than that of bulk mobility. Each value of $\mathcal{S}$ leads to a result that could be matched with different hydrodynamic slip length l_s. The corresponding l_s monotonically decreases as $\mathcal{S}$ increases in Fig. 2-6B. It indicates that longer relaxation time on the solid wall behaves as to decrease the slip length which equivalently increases the contact-line friction $\ln(l_s^{-1})$ in the hydrodynamic descriptions. The choice of model parameter set Cn $= 0.03$, $l_m = 0.07$ and $\mathcal{S} = 1.2$ seems to provide the best match between simulations and the expected dynamics with $l_s = 1 \times 10^{-5}$ for static contact angle $\theta_e = 20°$.

We further use the phase-field model to study the dynamics of spontaneous im-

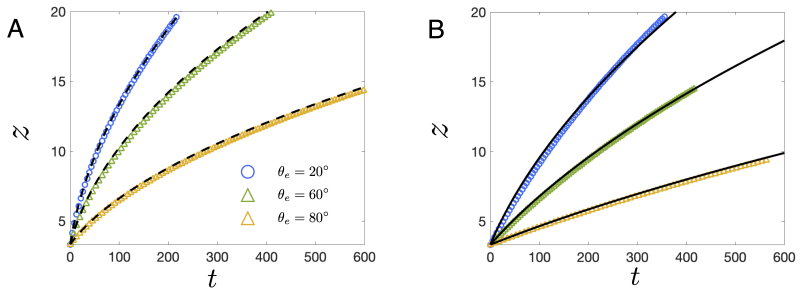

Figure 2-7: (A) Spontaneous imbibition for three different wettability conditions using equilibrium boundary condition $\mathcal{S} = 0$. The other two model parameters are $l_m = 0.07$ and Cn $= 0.03$. The dashed line shows the theoretical prediction from Eq. (2.49) with same hydrodynamic slip length $l_s = 5 \times 10^{-1}$. (B) Spontaneous imbibition for three different wettability conditions using nonequilibrium boundary condition $\mathcal{S} = 1.2$. The other two model parameters are same with these in (A). The solid lines show the theoretical prediction with different hydrodynamic slip length l_s that best fits the simulated data, which are $l_s = 1 \times 10^{-5}$ for $\theta_e = 20°$, $l_s = 1 \times 10^{-9}$ for $\theta_e = 60°$ and $l_s = 5 \times 10^{-12}$ for $\theta_e = 80°$.

bibition for different wettability conditions. Fig. 2-7A shows the results for three different θ_e using equilibrium boundary condition $\mathcal{S} = 0$ and $l_m = 0.07$. All of them are well described by the theoretical prediction with the same hydrodynamic slip length $l_s = 5 \times 10^{-1}$, which indicates that the selection of mobility l_m is not affected by the static contact angle. We then apply the nonequilibrium boundary condition with the optimal $\mathcal{S} = 1.2$ tested above to these three wettability conditions, the results of which are shown in Fig. 2-7B. The hydrodynamic slip length l_s that best fits the phase-field simulations increases from 1×10^{-5} to 1×10^{-9} and 5×10^{-12} as θ_e increases from 20° to 60° and 80°. This decreasing relation between slip length l_s and θ_e in spontaneous imbibition remains as an open question to be confirmed with experiments.

2.5 Constant-rate displacement: wetting transition and interface pinch-off

One fundamental aspect of fluid-fluid displacement in confined geometries is the wetting transition: the displacement rate above which thin films of the defending fluid are

deposited on the confining surfaces (Zhao *et al.*, 2018). These films may later dewet, which leads to interface pinch-off and generation of disconnected bubbles and drops even in uniform capillaries (Zhao *et al.*, 2018; Pahlavan *et al.*, 2019). Here we use our phase-field model to simulate viscously unstable constant-rate displacement in a capillary tube. The initial distribution of the order parameter is given by Eq. (2.50). The additional boundary conditions at tube outlet are specified in Eq. (2.52), while at tube inlet are set as:

$$v = v_{\text{inj}}, \quad \phi = 1. \tag{2.53}$$

The unfavorable viscosity ratio is fixed as $\eta = 1000$.

2.5.1 The selection of bulk mobility

Before investigating the influence of nonequilibrium boundary condition on constant-rate displacements, we have to choose an optimal combination of Cahn number Cn and bulk diffusion length l_m. As is mentioned in the Section 2.4, we fix Cn = 0.03 for the purpose of keeping the computation time reasonable. We then select l_m via the simulations with equilibrium boundary condition $\mathcal{S} = 0$ and fixed static contact angle $\theta_e = 112°$. Fig. 2-8A shows an example of displacement patterns from low to high capillary numbers, with model parameters $l_m = 0.002$ and Cn = 0.03. At low Ca numbers, the fluid-fluid interface deforms slightly from the equilibrium shape but remains stable while moving downstream. Above a critical threshold, the interface becomes unstable as a finger propagating along the tube center with a thin film of defending fluid deposited on the tube wall. We measure the contact-line velocity $\text{Ca}_{\text{cl}} = v_{\text{cl}}\mu_1/\gamma$ in each constant-rate simulation, shown in Fig. 2-8B. The gray dashed line indicates $\text{Ca}_{\text{cl}} = \text{Ca}$. The contact line of a stable interface moves at a constant speed given by the displacement rate Ca. Beyond the wetting transition where the interface forms a finger, the contact-line velocity deviates from the one-to-one line but remains fixed at a constant value that is smaller than the imposed Ca. This constant value is referred to as the maximum speed of contact line $\text{Ca}_{\text{cl},m}$. The observations of wetting transition and drop-off of contact-line velocity qualitatively agree with the

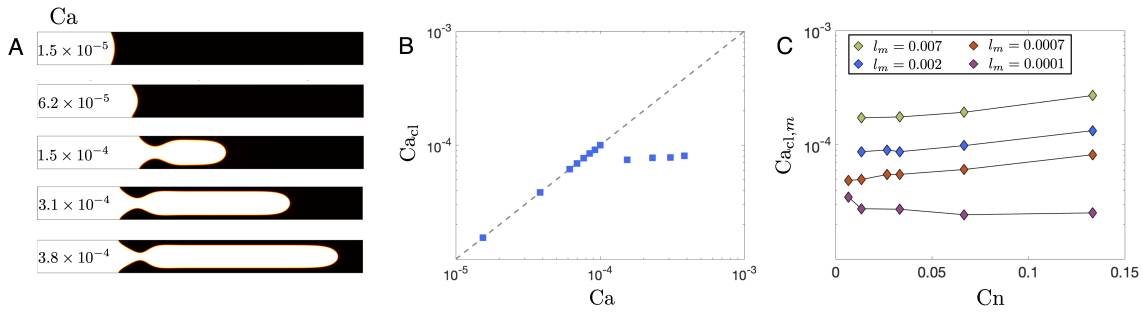

Figure 2-8: (A) Displacement patterns for fixed wettability condition $\theta_e = 112°$ and various capillary numbers, simulated using equilibrium boundary condition, $\mathcal{S} = 0$. (B) Contact-line capillary number $\mathrm{Ca_{cl}}$ as a function of bulk displacement capillary number Ca, measured from the simulations shown in (A). The gray dashed line indicates $\mathrm{Ca} = \mathrm{Ca_{cl}}$. (C) Maximum contact-line velocity for different l_m and Cn numbers under fixed $\mathcal{S} = 0$ and $\theta_e = 112°$. For $l_m = 0.0001$, $\mathrm{Ca_{cl}}$ is measured at the displacement rate $\mathrm{Ca} = 3.8 \times 10^{-5}$. For the other three l_m values, $\mathrm{Ca_{cl}}$ is measured at $\mathrm{Ca} = 3.8 \times 10^{-4}$.

experiments by Zhao *et al.* (2018).

We then justify the selection of l_m based on $\mathrm{Ca_{cl,}}_m$, for two reasons: (1) from a modeling point of view, with an equilibrium boundary condition, the bulk mobility l_m determines the contact-line dynamics, as the contact-line motion is purely driven by the higher-order diffusion (see Cahn-Hilliard equation in Eq. (2.12)); (2) from a physical point of view, the maximum speed that the contact line can sustain determines the wetting transition threshold and controls the subsequent thin-film dewetting and interface pinch-off (Zhao *et al.*, 2018; Pahlavan *et al.*, 2019). Fig. 2-8C shows shows the $\mathrm{Ca_{cl,}}_m$ measured from constant-rate simulations with different l_m and Cn numbers. Generally, a smaller mobility l_m slows the higher-order diffusion and thus decreases the maximum contact-line speed $\mathrm{Ca_{cl,}}_m$. However, we also observe that l_m cannot be infinitely small given a fixed $\mathrm{Cn} = 0.03$. For the $l_m = 0.007$ or $l_m = 0.002$, $\mathrm{Ca_{cl,}}_m$ converges to an asymptotic value with Cn decreasing to around 0.03. For the $l_m = 0.0007$, Cahn number has to decrease to $\mathrm{Cn} = 0.01$ in order to produce an converged $\mathrm{Ca_{cl,}}_m$. For the smallest $l_m = 0.0001$ tested here, $\mathrm{Ca_{cl,}}_m$ does not change much at large Cn values but increases as Cn approaches 0.003, indicating that convergence to the sharp-interface limit has not been reached. This criterion for sharp-interface convergence is consistent with the analysis in Yue *et al.* (2010). We

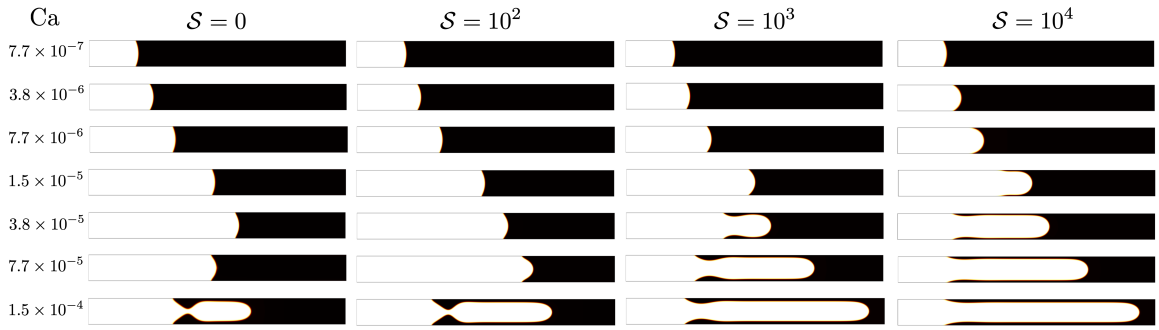

Figure 2-9: Visual phase diagram of displacement patterns for four surface relaxation times $\mathcal{S}$ and a wide range of capillary numbers Ca. Here the wettability condition is fixed as $\theta_e = 112^o$ and invading phase is much less viscous than the defending phase $\eta = 1000$.

will use $l_m = 0.002$ and Cn $= 0.03$ as the optimal parameter set for the following simulations of constant-rate displacements.

2.5.2 Influence of the nonequilibrium boundary condition

We then account for a nonequilibrium boundary condition in the simulations of constant-rate displacements. Fig. 2-9 shows a visual phase diagram of displacement patterns at four values of surface relaxation time $\mathcal{S}$ that span two orders of magnitude and a wide range of displacement rates. The static contact angle is fixed at $\theta_e = 112°$. The leftmost column $\mathcal{S} = 0$ represents the equilibrium boundary condition (same as those in Fig. 2-8A). The prescribed relaxation time on the solid surface increases from left to right column, which allows a stronger deviation of the fluid-fluid interface structure from the equilibrium configuration near contact lines. We still observe the occurrence of the dynamic wetting transition, beyond which the interface becomes unstable with a thin film of defending fluid on the tube walls. However, the transition threshold significantly decreases with increasing surface relaxation time. The dewetting of the thin film later leads to interface pinch-off, the dynamics of which also depend on $\mathcal{S}$.

Apparent contact angle and wetting transition threshold

We characterize the deformation of the fluid-fluid interface by the apparent contact angle θ_{app}, described in section 2.4.2. Fig. 2-10A shows that θ_{app} increases from its static value θ_e and reaches π at a critical capillary number Ca^*. We describe the relation between θ_{app} and Ca using generalized Cox's equation in Eq. (2.45), given the viscosity ratio $\eta = 1000$. Fig. 2-10B shows that the data simulated using the equilibrium boundary condition ($\mathcal{S} = 0$) is best fitted with slip length $l_s = 0.14$. However, in reality, the slip length is usually in the order of nanometers (Joseph & Tabeling, 2005), which corresponds to l_s in the range between 10^{-5} and 10^{-4}. Using the nonequilibrium boundary condition decreases the l_s and brings it to this realistic range. For the simulations with $\mathcal{S} = 10^3$, a linear regression to the simulation data gives $l_s = 5 \times 10^{-5}$.

The critical threshold, Ca^*, that marks the onset of wetting transition decreases with increasing $\mathcal{S}$, as is shown in Fig. 2-10C. We compare the Ca^* for four simulations with the well-established hydrodynamic theory (Chan *et al.*, 2013; Levaché & Bartolo, 2014; Zhao *et al.*, 2018). Here, the Laplace pressure jump across the fluid-fluid interface is balanced by the normal viscous stress discontinuity. The latter is the analytical solution of the Stokes flow in a wedge under the generalized lubrication approximation (Huh & Scriven, 1971; Snoeijer, 2006). We then arrive at the differential equation describing the shape of a stable interface used in Zhao *et al.* (2018):

$$\frac{d^2\theta}{ds^2} = \frac{3\text{Ca}F(\theta,\eta)}{z(z+3l_s)}, \tag{2.54}$$

where θ is the local interface slope, s is the arc length along the interface and the algebraic function $F(\theta, R)$ is (Chan *et al.*, 2013):

$$F(\theta,\eta) = \frac{2\sin^3\theta\big[\eta^2(\theta^2-\sin^2\theta)+2\eta(\theta(\pi-\theta)+\sin^2\theta)+(\pi-\theta)^2-\sin^2\theta\big]}{3\big[\eta(\theta^2-\sin^2\theta)(\pi-\theta+\sin\theta\cos\theta)+((\pi-\theta)^2-\sin^2\theta)(\theta-\sin\theta\cos\theta)\big]}.$$

The differential equation is solved with the boundary conditions: $\theta|_{s=0} = \theta_e$, $z|_{s=0} = l_s$, $\theta|_{s=1} = \pi/2$ and $z|_{s=1} = 1/2$. The prediction for $\theta_e = 112^\circ$ is shown as dashed line

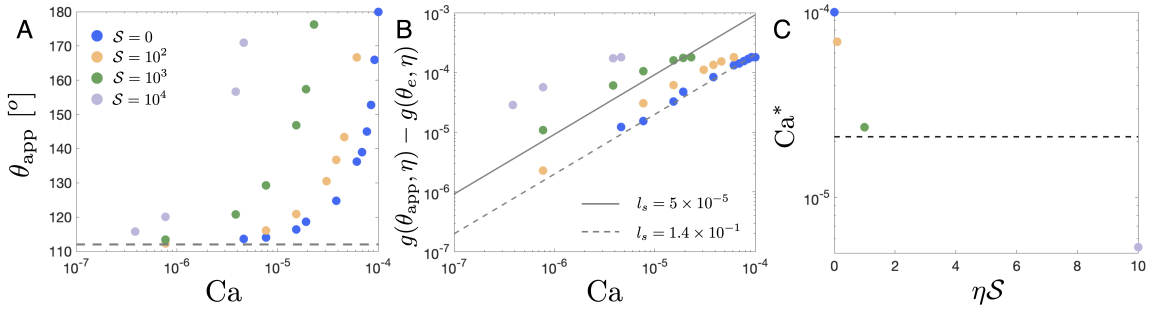

Figure 2-10: (A) Apparent contact angle $\theta_{\rm app}$ as a function of capillary number Ca for different surface relaxation time $\mathcal{S}$. The dashed line indicates the static contact angle $\theta_e = 112°$. (B) The data shown in (A) follows the generalized Cox law in Eq. (2.45) with different slip lengths. The dashed line is fitted to the simulations using the equilibrium boundary condition $\mathcal{S} = 0$, which leads to a slip length $l_s = 0.14$. The solid line shows Cox's law with slip length $l_s = 5 \times 10^{-5}$. (C) Wetting transition threshold Ca*, defined as the Ca at which $\theta_{\rm app} = 0$, as a function of $\mathcal{S}$. The dashed line shows the theoretical Ca* for $\theta_e = 112°$, calculated using Eq. (2.54).

in Fig. 2-10C. The nonequilibrium boundary condition with $\mathcal{S} = 1$ matches well with the theory while $\mathcal{S} = 10$ turns out to undershoot the prediction.

Thin-film thickness

Above the wetting transition threshold Ca $>$ Ca*, the fluid-fluid interface forms a finger and a thin film of viscous defending liquid is entrained on the tube walls. The thickness of this thin film h_f increases with displacement rate, as is shown in Fig. 2-11. Bretherton (1961) derived a model to describe the interface profile based on the lubrication approximation for the thin film flow, where the driven pressure is given by the interface curvature. Using asymptotic analysis, the thickness h_f is found to be:

$$\frac{h_f}{R} = 1.34\mathrm{Ca}_f^{2/3}, \tag{2.55}$$

where Ca$_f$ is the finger capillary number. This equation was later empirically extended to high capillary numbers (Aussillous & Quéré, 2000; Klaseboer *et al.*, 2014):

$$\frac{h_f}{R} = \frac{1.34\mathrm{Ca}_f^{2/3}}{1 + 1.34 \times 2.5\mathrm{Ca}_f^{2/3}}. \tag{2.56}$$

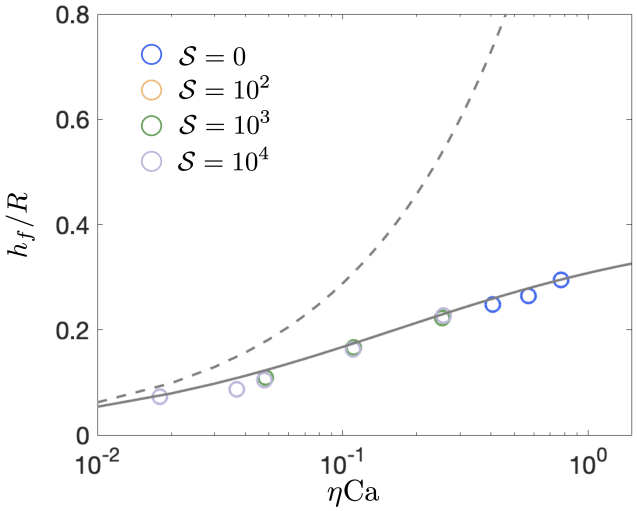

Figure 2-11: Thickness of the entrained thin film as a function of Ca, simulated with different values of the surface relaxation number $\mathcal{S}$. The dashed line indicates the original Bretherton law in Eq. (2.55) and the solid line indicates the extended Bretherton law in Eq. (2.56).

Although in these studies the bubble is a gas and the surrounding liquid is completely wetting to the solid wall, the relations can apply to our liquid-liquid system since the key assumption of the lubrication approximation is still valid for the large viscosity contrast $\eta = 1000$ in our system. Note that the finger capillary number $\mathrm{Ca}_f = v_f \mu_2/\gamma$ should be defined using the viscosity of defending liquid inside the thin film and the finger velocity v_f estimated by the conservation of mass:

$$\mathrm{Ca}_f = \frac{\mathrm{Ca}}{(R - h_f)^2}\eta. \tag{2.57}$$

The simulated h_f using different surface relaxation numbers $\mathcal{S}$ agree well with the theoretical prediction that combines Eq. (2.56) and (2.57), as is shown Fig. 2-11.

Thin-film dewetting and interface pinch-off

Here we discuss the dynamics of dewetting and pinch-off predicted by our phase-field model. Fig. 2-12A shows several snapshots of fluid-fluid interface evolution during thin-film dewetting in a frame comoving with the contact line for $\theta_e = 112°$, $\mathrm{Ca} = 3.9 \times 10^{-5}$ and $\mathcal{S} = 10^3$. Note that this $\mathcal{S}$ value captures the theoretical wetting

transition threshold (Fig. 2-10C). We observe that, as the contact line recedes, a rim forms in its vicinity and grows to collect the residual liquid until pinch-off at time t_p, at which point a bubble forms. The simulations also give us access to the velocity field inside the thin films. The arrows in Fig. 2-12A indicate that the motion of residual liquid mainly occurs inside the rim, while the fluid in the flat region remains stagnant. This feature is consistent with the classic viscous dewetting of a rim on an unconfined plate (Redon *et al.*, 1991; Gennes *et al.*, 2004).

Another important observation is the flow direction. At early times, far away from pinch-off (Fig. 2-12A1-3), the flow is mainly in the axial direction. The radial flow component gradually becomes more important as the rim grows (Fig. 2-12A4) and plays a dominant role when approaching the pinch-off time (Fig. 2-12A5). This feature of flow transition from axial direction to radial direction is consistent with the theory of pinch-off in capillary tubes by Pahlavan *et al.* (2019). The cross-over time is estimated as the visco-capillary time $\tau_{vc} = 2R\mu_2/\gamma$. Specifically, they established a $1/5$ power-law scaling of rim height as a function of time to pinch-off in the early-time regime based on the balance of capillary force and viscous force from axial flow. The green stars in Fig. 2-12B show the rim thickness evolution measured from the simulation in Fig. 2-12A, which matches with the $1/5$ scaling.

The results in Fig. 2-12B show that increasing the flow rate by 4 times changes the early-time dynamics as the scaling exponent becomes larger than $1/5$, given the same surface relaxation time $\mathcal{S} = 10^3$. Unlike the air-glycerin system used in Pahlavan *et al.* (2019) where pressure drop in the air is always negligible, the viscous force inside the invading phase in our liquid-liquid system may become important as the flow rate increases. In this case, the interface shape may be determined by not only the viscous force inside the rim but also that in the ambient liquid. Fig. 2-12B also shows that, given the same capillary number, faster surface relaxation increases the rate of rim growth.

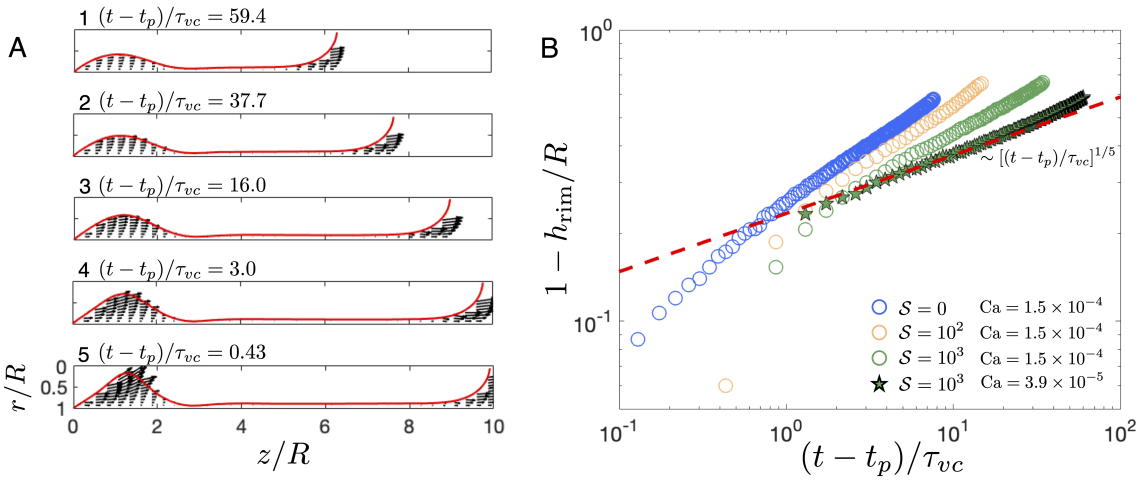

Figure 2-12: (A) Fluid-fluid interface evolution during thin-film dewetting in a moving reference frame for $\theta_e = 112°$, Ca $= 3.9 \times 10^{-5}$ and $\mathcal{S} = 10^3$. Here, t_p is the pinch-off time, and $\tau_{vc} = 2R\mu_2/\gamma$ denotes the visco-capillary time scale. The back arrows indicate the velocity vector in the defending phase normalized by the imposed injection rate U_c. (B) Evolution of the rim height versus time, measured from simulations with various capillary numbers and $\mathcal{S}$. The dashed red line denotes the $1/5$ power-law scaling of early-time pinch-off, proposed by Pahlavan *et al.* (2019).

2.6 Conclusions

We have developed a phase-field model to investigate two-phase displacements in a capillary tube. We present a generalized formulation of solid-liquid surface energy $f_w(\phi)$ that incorporates the descriptions of bulk energy density $f(\phi)$ and higher-order stiffness $\kappa(\phi)$, capable of simulating two-phase systems with complex thermodynamic descriptions. The key aspect of our formulation is to constrain the function by enforcing the consistency of the internal structure of the diffuse fluid-fluid interface from the bulk fluid to the solid surface. We show that this self-consistent definition of the surface energy function is essential to reproduce the correct fluid-fluid configuration and the correct Laplace pressure even at static equilibrium conditions

We illustrate the ability of our model to produce the dynamics of spontaneous imbibition of a viscous liquid into another one at arbitrary static contact angle, through the comparison with the theoretical model that couples the classic Lucas-Washburn theory with Cox law. While decreasing the bulk diffusion length l_m leads to a result closer to the theoretical predictions, its value is contrained by the Cn for convergence

to the sharp-interface limit. A good match between phase-field simulation and theoretical model with realistic slip length can only be achieved using a nonequilibrium formulation on the solid surface.

We further show the ability of our model to capture complex interfacial behavior of viscously unstable constant-rate displacement. Accounting for nonequilibrium boundary condition allows not only qualitative agreement with experimental observations, but also quantitative match with the hydrodynamic theory. At low capillary numbers, the fluid-fluid interface deforms from the equilibrium shape but remains stable. The deformation corresponds to an increasing apparent contact angle as Ca increases, the relation of which follows the Cox equation with slip length $l_s \sim O(10^{-5})$. At a critical threshold Ca^*, the apparent contact angle reaches π, triggering a wetting transition. Notably, this threshold Ca^* simulated by our model agrees with the well-established hydrodynamic theory used in Zhao *et al.* (2018), which cannot be achieved using the equilibrium boundary condition. Beyond the wetting transition, a thin film of viscous defending liquid is left behind the advancing meniscus wetting the tube walls, the thickness of which is described by an extended Bretherton law. The thin film dewets on the tube wall, with a rim forming and growing in the vicinity of the contact line, which finally leads to interface pinch-off under geometric confinement. Our simulations capture the detailed motion inside the thin film — the dominant flow component transitions from axial direction to radial direction around the visco-capillary time scale. The growth rate of rim height exhibits a $1/5$ power-law scaling in time, in agreement with the theory established in Pahlavan *et al.* (2019).

As a future extension, our model can be used to establish a comprehensive understanding of liquid-liquid displacement patterns as a function of wettability, viscosity ratio and capillary number. Specifically, it will allow us to explore the types of wetting transition and the pinch-off dynamics of a liquid-liquid interface, a fundamental aspect of fluid-fluid displacement in confined geometries that has remained elusive to computational modeling.

Chapter 3

Moving fluid-fluid interface in a prewetted capillary tube

3.1 Introduction

The displacement of one fluid by another immiscible fluid in small, confined geometries is an important process in many natural and industrial settings, including water infiltration into soil (Hill & Parlange, 1972; Cueto-Felgueroso & Juanes, 2008), enhanced oil recovery (Orr Jr & Taber, 1984), and microfluidics (Whitesides, 2006). One fundamental aspect of fluid-fluid displacement on the solid surface is to determine the moving interface shape as a function of pertinent dimensionless parameters, for examples, viscosity ratio of the two fluids and capillary number that characterizes the relative importance of viscous force over capillary force (Hoffman, 1975, 1983; Ledesma-Aguilar *et al.*, 2013; Levaché & Bartolo, 2014; Zhao *et al.*, 2018).

Much of the research on fluid-fluid displacement has focused on the partial wetting regime where the fluid interface intersects the solid surface at nonzero angle and forms a contact line at equilibrium condition (Levaché & Bartolo, 2014; Zhao *et al.*, 2018). The presence of contact line not only leads to stress singularity that challenges the mathematical modeling (Huh & Scriven, 1971; Alizadeh Pahlavan *et al.*, 2015), but also increases the sensitivity of the physical system to the subtle defects on the solid surface that plagues experimental measurements (Fermigier & Jenffer, 1991). As

a consequence, the description of moving interface shape in a smooth confinement remains puzzling for which conflicting views currently exist in the literature. The experimental observations by Ref. (Hoffman, 1975; Fermigier & Jenffer, 1991; Zhao *et al.*, 2018) demonstrate that the dynamic contact angle, which quantifies fluid-fluid interface shape on the macroscopic scale, increases with interface velocity up to π at a wetting transition threshold. Beyond this critical threshold, a *trailing* film of defending fluid is left on the solid wall while the invading fluid propagates along the tube center (Zhao *et al.*, 2018). However, a recent experiment by Ref. (Levaché & Bartolo, 2014) shows a completely different type of wetting transition: the invading fluid instead advances along the solid surface as a *pilot* film. The authors emphasized that the formation of pilot film is persistent in the regime of strong imbibition with unfavorable viscosity ratio.

In this work, we investigate the strong imbibition regime in a capillary tube prewetted by the invading phase, which not only ensures the consistency of static contact angle but also eliminates the potential contamination on the solid surfaces. We observe the universal behavior of dynamic contact angle monotonically increasing with capillary number, given different fluid viscosity and thickness of prewetting layer. Remarkably, we observe a sharp wetting transition for viscously unfavorable displacement where the dynamical contact angle abruptly jumps to π at a critical flow rate. Above the transition, the invading phase advances along the tube center as a finger while leaving behind a trailing film of viscous defending fluid. We rationalize the emergence of this sharp, trailing-film type of wetting transition by means of a minimal-ingredients hydrodynamic theory that exhibits bifurcated solutions. In the end of this chapter, we experimentally realized the formation of pilot film in a rough capillary tube, pointing out that the underlying mechanism is the combined effect of roughness amplitude and prewetting layer height.

3.2 Experimental method

We conduct fluid-fluid displacement experiments in precision-made borosilicate glass capillary tubes with inner diameter $d = 580$ μm (Fig. 5-1A). Before each experiment, we carefully clean the tube by soaking it in Piranha solution and then thoroughly rinsing it with DI water. To achieve strong imbibition regime, we prewet the capillary tube with a layer of invading by conducting a primary imbibition-drainage cycle. See the schematic in Fig. 5-1B. The right end of the capillary tube is always connected to a syringe pump of wetting liquid. During the primary imbibition, the capillary tube is open to the atmosphere on the left end and fully filled with the wetting liquid. During the primary drainage, we connect the wetting fluid-filled tube with an reservoir of nonwetting fluid. We withdraw the nonwetting fluid from the capillary tube so that nonwetting fluid displaces wetting fluid at a constant rate Q_{withdraw}. Since the wetting liquid is completely wetting to the tube wall, a thin film of wetting fluid is left behind the displacement front which is referred to as precursor film. The thickness of precursor film h_w is controlled by the withdrawing rate — higher Q_{withdraw} leads to thicker h_w. The relation between h_w and Q_{withdraw} can be quantified by extended Bretherton law (Klaseboer *et al.*, 2014) when the nonwetting fluid is less viscous than the wetting fluid $\mu_{\text{nonwetting}} \ll \mu_{\text{wetting}}$:

$$\frac{h_w}{R} = \frac{1.34\text{Ca}_{\text{withdraw}}^{2/3}}{1 + 1.34 \times 2.5\text{Ca}_{\text{withdraw}}^{2/3}}. \tag{3.1}$$

We define the withdrawing capillary number is defined as $\text{Ca}_{\text{withdraw}} = \mu_{\text{wetting}} U/\gamma$, where $U = 4Q_{\text{withdraw}}/(\pi d^2)$ is the displacement velocity and γ is the interfacial tension between wetting fluid and nonwetting fluid. While the nonwetting fluid is more viscous than the wetting fluid $\mu_{\text{nonwetting}} \gg \mu_{\text{wetting}}$, the relation is quantified by the anti-Bretherton law:

$$\frac{h_w}{R} = 0.643(12\text{Ca}_{\text{withdraw}})^{2/3}. \tag{3.2}$$

We then re-inject the wetting fluid to displacement the nonwetting fluid at a constant flow rate Q. This is a strong imbibition where the invading fluid completely wets and solid wall. We define the viscosity ratio as $\eta = \mu_{\text{nonwetting}}/\mu_{\text{wetting}}$, and the capillary number as $\text{Ca} = \mu_{\text{wetting}}U/\gamma$, where $U = 4Q/(\pi d^2)$.

3.3 Experimental results

3.3.1 Viscously favorable displacement

Fig. 3-2A shows the fluid-fluid interface profiles obtained under different capillary numbers Ca for the displacement of viscous oil ($\mu_{\text{wetting}} = 1000$ mPas) into air, without precursor film $h_w = 0$. As Ca increases, the interface deforms from its equilibrium state and travels downstream at a constant velocity, without changing its shape. Deformation of the fluid-fluid interface can be quantified by dynamic contact angle θ_{app} on the macroscopic scale, which monotonically and continuously increases with Ca (Fig. 3-2B). Our data matches well with measurements from classic Hoffman experiments which also studied the displacement of viscous liquid into air (Hoffman, 1975). When the solid surface is smooth and the invading phase is much more viscous than the defending phase, the dynamic contact angles are expected to follow the Cox-Voinov equation (Cox, 1986), which can be written as:

$$\theta_{\text{app}}^3 = 9\Gamma\text{Ca}, \tag{3.3}$$

given that the equilibrium contact angle in our system in 0°. Note that $\Gamma = \ln(R/h_{\text{micro}})$ where tube radius $R = d/2$ is the macroscopic length and h_{micro} is the microscopic cutoff length near the contact line. When using $h_{\text{micro}}/R = 10^{-4}$ ($\Gamma = 9.21$), the Cox-Voinov equation produces good agreement with our experimental measurements (Fig. 3-2B).

Fig. 3-2B also shows the dynamic contact angle as a function of capillary number under five values of precursor film thickness. Here we keep the viscosity of wetting phase as $\mu_{\text{wetting}} = 1000$ mPas, such that viscosity ratio $\eta = 1 \times 10^{-5}$. As h_w increases,

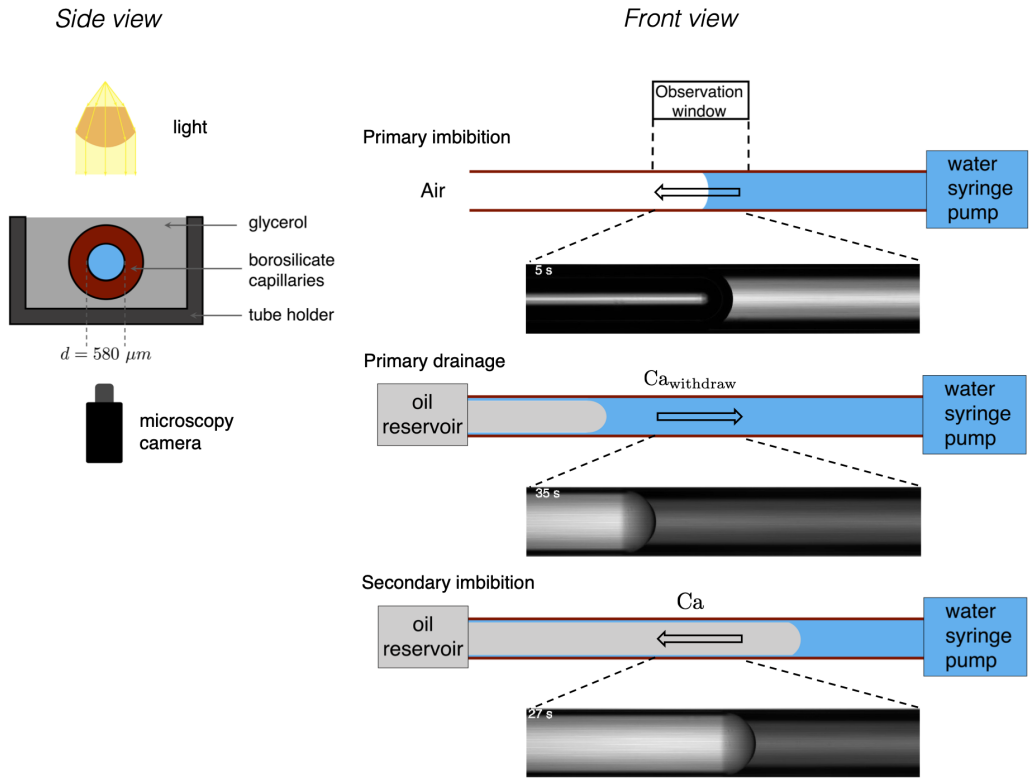

Figure 3-1: We study fluid-fluid displacement in circular capillary tubes. We use precision-made borosilicate glass capillary tubes with inner diameter $d = 580$ μm. The circular capillary tube is housed in a transparent square container filled with glycerol, which has the same refractive index as borosilicate glass. This combination reduces light refraction through the capillary tube, which enables clear, undistorted visualization of the fluid-fluid interface via a microscopy camera. To achieve fluid-fluid displacement in a tube prewetted by the invading phase, we use a three-stage injection method: (i) primary imbibition. The capillary tube is open to the atmosphere on the left end and connected to a syringe pump on the right end. We inject the more wetting invading liquid to displace air untill it fully fills the tube; (ii) primary drainage. We then connect the wetting-fluid-filled tube with an reservoir of defending fluid. We withdraw the defending liquid from the capillary tube so that nonwetting fluid displaces the wetting fluid at a constant rate Q_{withdraw}. Since the capillary tube is completely wetting to the wetting phase, a thin film of wetting fluid is left behind the displacement front with a thickness depending on Q_{withdraw}, which is referred to as precursor film. (iii) secondary imbibition. We then re-inject the wetting fluid to displace the nonwetting fluid at a constant rate Q. This is a forced imbibition where the invading fluid completely wets solid wall.

the relation of θ_{app} versus Ca shifts, highlighting that the deformation of fluid-fluid interface is delayed. The shifting demonstrates that the precursor film with viscous liquid plays a role of reducing viscous dissipation near the solid wall.

However, a precursor film of less viscous liquid does not provide enough lubrication effect for the moving interface. Fig. 3-2C shows the θ_{app} obtained under different capillary numbers Ca and different h_w for the displacement of less viscous oil ($\mu_{\text{wetting}} = 5$ mPas) into air. The $\theta_{\text{app}}(\text{Ca})$ relation does not change as h_w increases.

To understand the effect of the precursor film on the deformation of the interface, we rescale the capillary numbers by a factor Φ, $\widetilde{\text{Ca}} = \text{Ca}\Phi$, such that the dynamic contact angle measured at different values of h_w/R and viscosity ratio (Fig. 3-2B and C) are collapsed onto a single curve (Fig. 3-2D). This master curve is the Cox-Voinov law for $h_w/R = 0$ and $\eta = 0$ (Eq. 3.3). The scaling factor Φ depends on both the precursor film thickness h_w/R and the viscosity ratio η (see the table in Fig. 3-2E). We first establish the relation between Φ and h_w/R by fitting the data for a fixed $\eta = 1 \times 10^{-5}$, as is shown in Fig. 3-2F. The relation is best described by an exponential function $\Phi_{h_w} = e^{-\alpha h_w/R}$, with the coefficient $\alpha = 120$. Then we find the relation between between Φ and η by fitting the data for a fixed $h_w/R = 1 \times 10^{-2}$, as is shown in Fig. 3-2G. Given the limited data, the best fitted function takes the form $\Phi_\eta = a + b \log \eta$, with $a = 1.88$ and $b = 0.326$.

The above-mentioned scaling functions $\Phi_{h_w}(h_w/R)$ and $\Phi_\eta(\eta)$ can be extended to develop a complete description of $\Phi_{h_w,\eta}(h_w/R, \eta)$ that depends on h_w/R and η simultaneously. Moreover, we note that, with sufficiently thick precursor film (green dots in Fig. 3-2D), the current scaling does not collapse the data well. It indicates that Φ not only depends on h_w and η but may also depend on Ca.

3.3.2 Viscously unfavorable displacement: sharp wetting transition and fingering instability

We then investigate the pattern forming during viscously unfavorable displacement $\eta > 1$. Fig. 3-3 shows the fluid-fluid interface profiles obtained under different cap-

illary numbers and precursor film thickness for water ($\mu_{\text{wetting}} = 1$ mPas) displacing viscous oil ($\mu_{\text{nonwetting}} = 1000$ mPas). At low capillary number, the fluid-fluid interface deforms slightly from its equilibrium shape but remains stable as it moves downstream. When quantifying the interface deformation by θ_{app} (Fig. 3-3B), we observe a sharp wetting transition, where the dynamic contact angle jumps to 180° at a critical capillary number Ca^*. As precursor film increases from $h_w/R = 2 \times 10^{-4}$ to $h_w/R = 6 \times 10^{-4}$, the transition threshold Ca^* increases. For thicker precursor film ($h_w/R = 6 \times 10^{-3}$), we do not capture the wetting transition as the tested Ca is not high enough in our experiments. Remarkably, beyond the wetting transition, the fluid-fluid destabilizes and the wetting phase advances the tube center as finger, leaving behind a trailing film of the viscous defending phase. This fingering instability is in contrast with the observations in Ref. (Levaché & Bartolo, 2014) — given the presence of a prewetting layer on the tube wall, the invading wetting phase preferentially advances along the tube center with trailing-film formation instead of preferentially propagating along the tube wall with pilot-film formation.

3.4 Hydrodynamic model of moving interface

In this section, we use a minimal-ingredients hydrodynamic model to rationalize the experimental observations mentioned above. This model predicts the steady-state shape of a fluid-fluid interface given capillary number Ca, precursor film thickness h_w and viscosity ratio between the two fluids η.

3.4.1 Theoretical model

At steady-state, the flow dynamics is governed by the two-way coupling between the fluid-fluid interface shape and the flow field within the two phases (Zhao *et al.*, 2018). We construct the global interface profile based on a *local* pressure balance — the Laplace pressure jump is balanced with the viscous stress discontinuity across the interface at each point along the curve (Chan *et al.*, 2013; Zhao *et al.*, 2018). See the schematic in Fig. 3-4A. We compute the viscous stress discontinuity under generalized

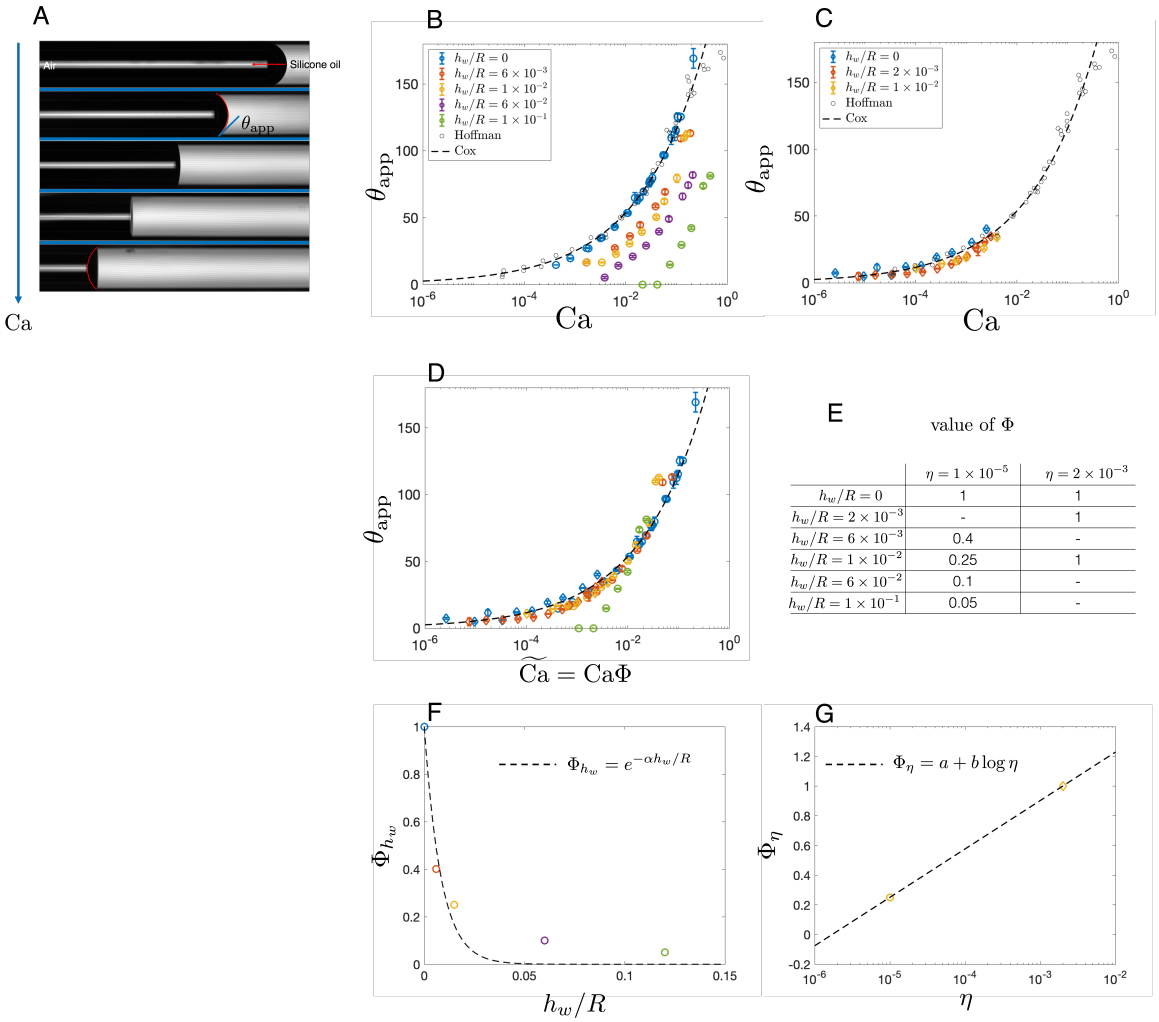

	$\eta = 1 \times 10^{-5}$	$\eta = 2 \times 10^{-3}$
$h_w/R = 0$	1	1
$h_w/R = 2 \times 10^{-3}$	-	1
$h_w/R = 6 \times 10^{-3}$	0.4	-
$h_w/R = 1 \times 10^{-2}$	0.25	1
$h_w/R = 6 \times 10^{-2}$	0.1	-
$h_w/R = 1 \times 10^{-1}$	0.05	-

Figure 3-2: (A) Fluid-fluid displacement of silicone oil displacing air under increasing capillary numbers (top to bottom) in a capillary tube without a precursor film. The interface shape can be quantified at a macroscopic scale by the dynamic contact angle θ_{app}. (B) Dynamic contact angle as a function of capillary number measured in experiments where the invading phase is viscous silicone oil with viscosity $\mu_{wetting} =$ 1000 mPas. The viscosity ratio is $\eta = 1 \times 10^{-5}$. We measure θ_{app} under five values of precursor film thickness h_w. The black dots indicate the data from Hoffman (Hoffman, 1975). The dashed line shows the Cox-Voinov relation in Eq. 3.3 (Voinov, 1976; Cox, 1986). (C) The invading phase is less viscous silicone oil $\mu_{wetting} = 5$ mPas. The viscosity ratio is $\eta = 2 \times 10^{-2}$. We measure θ_{app} under three values of precursor film thickness h_w. The black dots and dashed line are same with those in (A). (D) By rescaling the capillary number by a factor Φ, we collapse the data shown in (B) and (C) onto a single curve described by Eq. 3.3. (E) The table lists the value of scaling factor Φ for different values of the precursor film thickness and viscosity ratio. (F) The scaling factor Φ as a function of h_w/R for viscosity ratio $\eta = 1 \times 10^{-3}$. The dashed line is the best-fit exponential function with $\alpha = 120$. (G) The scaling factor Φ as a function of η for $h_w/R = 1 \times 10^{-2}$. The dashed line is the best-fit function with $a = 1.88$ and $b = 0.326$.

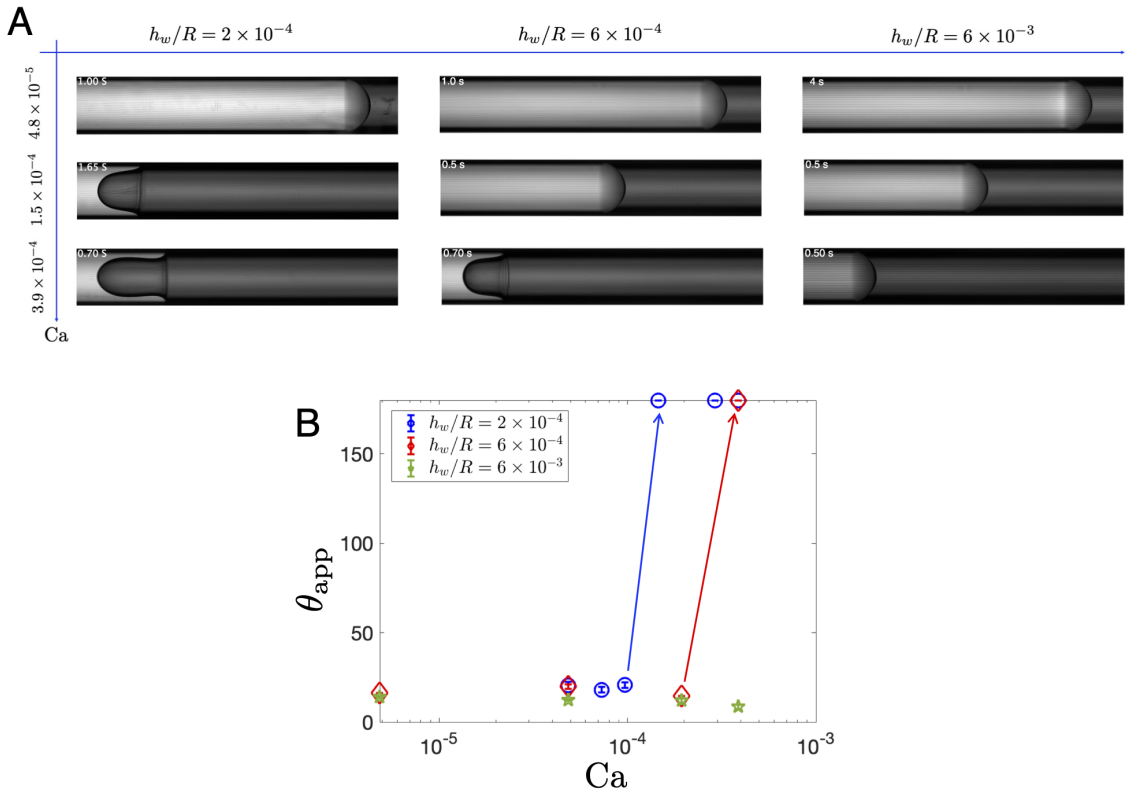

Figure 3-3: (A) Fluid-fluid interface of water (dark gray, $\mu_{\text{wetting}} = 1$ mPas) displacing silicone oil (light gray, $\mu_{\text{nonwetting}} = 1000$ mPas) under increasing capillary numbers (top to bottom) in a prewetted capillary tube with $h_w/R = 2 \times 10^{-4}$ (left column), $h_w/R = 6 \times 10^{-4}$ (middle column) and $h_w/R = 6 \times 10^{-3}$ (right column). The direction of interface displacement is from right end to left end. At small Ca, the meniscus deforms slightly from its equilibrium shape, but remains as a spherical cap. At sufficiently high Ca, however, a wetting transition occurs and the invading water forms a single finger that advances along the center of the tube, leaving behind a macroscopic trailing film of the viscous liquid. The critical capillary number Ca that onsets wetting transition increases with increasing thickness of precursor film. (B) The interface shape shown in (A) is quantified by the dynamic contact angle θ_{app}. As Ca increases, θ_{app} jumps to π abruptly at a critical value Ca*. Ca* is delayed as h_w/R increases from 2×10^{-4} to 6×10^{-4}. Ca* was not measured for 6×10^{-3} as much larger flow rate is needed to trigger the wetting transition.

lubrication approximation, which reduces the two-phase flow field to the Stokes flow in a wedge (Snoeijer, 2006). To the leading order approximation, we neglect the flow within the precursor film. Such that the *local* wedge tangential to the fluid-fluid interface all the way makes to the solid wall, where the no-slip boundary condition is applied. Under the local coordinate, the analytical solution for Stokes flow can be obtained using stream function (Huh & Scriven, 1971). In the moving reference frame, the governing equations for the dynamic interface shape can be written as (Zhao *et al.*, 2018; Chan *et al.*, 2013):

$$\frac{dh}{ds} = \sin\theta, \tag{3.4}$$

$$\frac{d\theta}{ds} = \kappa, \tag{3.5}$$

$$\frac{d\kappa}{ds} = \frac{\mathrm{Ca}}{h^2} F(\theta, \eta), \tag{3.6}$$

where s is the arc length along the interface, h is the local interface height, θ is the local interface slope and κ is the local interface curvature. The first two equations state the geometric relation while last equation states the pressure balance, where the algebraic function $F(\theta, \eta)$ denotes the viscous contribution (Cox, 1986; Chan *et al.*, 2013):

$$F(\theta,\eta) = \frac{2\sin^3\theta\left[\eta^2(\theta^2-\sin^2\theta) + 2\eta(\theta(\pi-\theta)+\sin^2\theta) + (\pi-\theta)^2 - \sin^2\theta\right]}{3\left[\eta(\theta^2-\sin^2\theta)(\pi-\theta+\sin\theta\cos\theta) + ((\pi-\theta)^2-\sin^2\theta)(\theta-\sin\theta\cos\theta)\right]}.$$

The hydrodynamic model is completed with four boundary conditions. At the precursor film surface, we prescribe the completely wetting condition and precursor film thickness:

$$\theta_{s=0} = 0, \quad h_{s=0} = h_w. \tag{3.7}$$

At the center of the tube, we apply the axisymmetric boundary condition:

$$\theta_{s=l} = \pi, \quad h_{s=l} = 1. \tag{3.8}$$

We solve this boundary value problem by shooting method. For a given set of parameter (Ca, h_w, η), we integrate the system of equations (Eq. 3.4-3.6) as an initial value problem, starting at the tube wall ($s = 0$). The initial values of local height and angle are given by the boundary conditions in Eq. 3.7. While we take a guess of the intial value for local curvature $\kappa_{s=0}^{\text{guess}}$. The integration is done using MATLAB `ODE45` function. Such that each $\kappa_{s=0}^{\text{guess}}$ leads to a solution of interface profile. We determine the proper initial value of initial curvature $\kappa_{s=0}$ by finding the solution with a trajectory that shoots the boundary condition in the tube center, given by Eq. 3.8. We develop the root-finding algorithm based on Bisection-Newton method.

3.4.2 Solutions: the emergence of bifurcation

Fig. 3-8B shows solutions of fluid-fluid interface under different capillary number for viscously favorable displacement with $\eta = 0$ and $h_w = 1 \times 10^{-5}$. As Ca increases, the interface gradually deforms from its equilibrium shape and eventually changes the sign of curvature. This is consistent with the experimental observations in Fig. 3-2A. We quantify the deformation of interface using dynamic contact angle in Fig. 3-8C, which is shown to continuously increase with Ca from 0 to 180°. As the precursor film becomes thicker, the $\theta_{\text{app}}(\text{Ca})$ shifts to right and larger Ca is needed for the interface deformation. This is consistent with the experimental observations in Fig. 3-2. Since the interface foot is fixed in the model ($x = 0$), we quantify the deformation using the horizontal location of fluid-fluid interface in the center of the tube x_c (Fig. 3-8D). As Ca increases, $-x_c$ increases from negative value (curve towards inlet) to positive value (curve towards outlet).

For viscously favorable displacement, the hydrodynamic model produces one solution only for one capillary number. While for viscously unfavorable displacement, the model exhibits saddle-node bifurcation — two branches of solutions could be obtained at one Ca. Fig. 3-5A shows the solutions of fluid-fluid interface at different capillary numbers for viscously unstable displacement $\eta = 1000$ and $h_w/R = 2 \times 10^{-4}$. At low capillary numbers, only one solution exists for a given Ca (black lines). In this region, the interface deforms from its equilibrium shape as Ca increases. Above

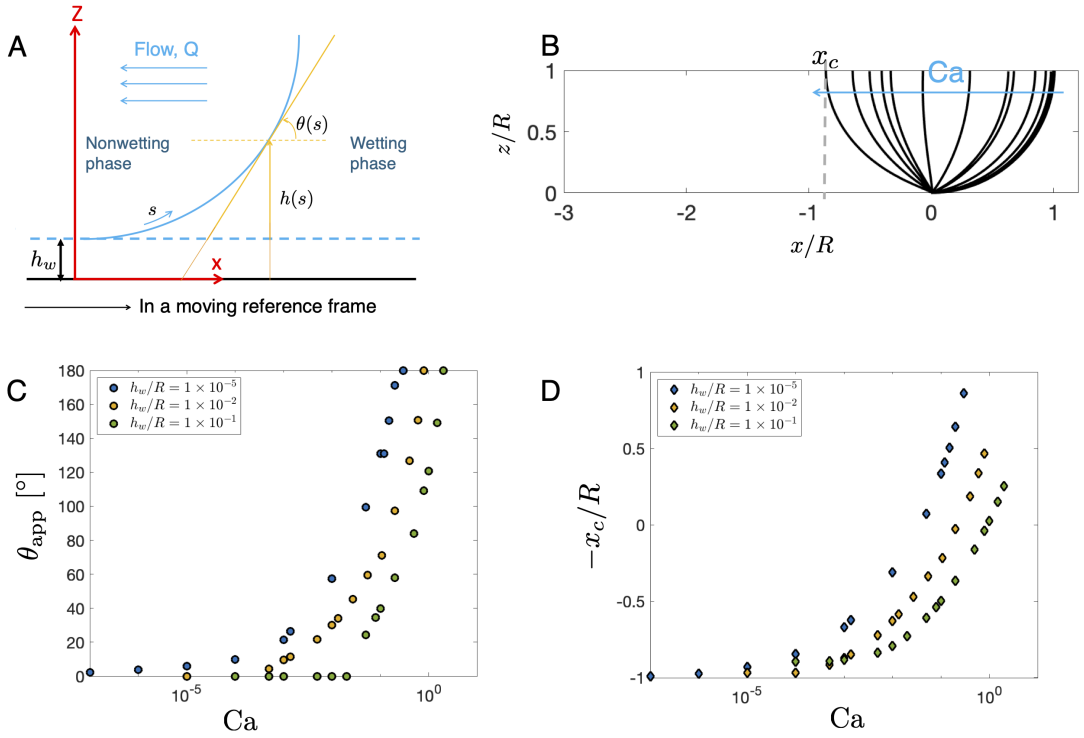

Figure 3-4: (A) Schematic of the interface shape (Blue solid line) in the frame co-moving with the fluid-fluid interface. The horizontal blue dashed line denotes the the surface of precursor film. The red lines denote the global [x,z] coordinate. The yellow solid line denotes the *local* wedge tangential to the interface, based on the generalized lubrication approximation. $\theta(s)$ and $h(s)$ are the local angle and local height along the interface. (B) Simulated fluid-fluid interface profiles for viscously favorable displacement, with viscosity ratio $\eta = 0$ and precursor film thickness $h_w = 1 \times 10^{-5}$. As Ca increases, the fluid-fluid interface deforms from its equilibrium shape and curves towards the outlet. (C) Deformation of the fluid-fluid interface can be quantified by the dynamic contact angle θ_{app}, which increases to 180° as Ca approaches the critical capillary number Ca. (D) Since the meniscus foot is fixed in the model, we quantify the deformation using the horizontal location of fluid-fluid interface in the center of the tube x_c. As Ca increases, $-x_c$ increases from negative value (curve towards inlet) to positive value (curve towards outlet).

a critical threshold Ca_b, we find two solutions for a given Ca: blue lines denote the lower branch of solution where the interface continues to deform as Ca increases; red lines denote the upper branch of solution, where interface shrinks back as Ca increases. We quantify the interface shape by dynamic contact angle in Fig. 3-5B. In the single-solution region, θ_{app} increases with Ca. In the bifurcation region, the lower branch of solution shows that θ_{app} continues to increase with Ca, while the upper branch of solution shows that θ_{app} shoots 180° abruptly. When quantifying the interface shape in terms of x_c, the horizontal location of interface in the tube center, one could observe two critical capillary numbers (Fig. 3-5C): Ca_b that onsets the transition from single solution to bifurcated solution, and $\mathrm{Ca}_{\mathrm{fold}}$ at which the two branches of solution collide with each other. Above $\mathrm{Ca}_{\mathrm{fold}}$, no steady-state solution can be obtained from the hydrodynamic model.

Fig. 3-5D and E show the map of $-x_c$ to demonstrate our solution-finding procedure. At each Ca, we search for the solution by guessing the interface curvature at the precursor film surface $\kappa_0^{\mathrm{guess}}|_{s=0}$. One value of $\kappa_0^{\mathrm{guess}}|_{s=0}$ determines one interface shape that is quantified by its location at the tube center x_c. The red colormap denotes the value of $-x_c$. While the light gray indicates that simulated interface does not reach the tube center, due to the improper guess of $\kappa_0^{\mathrm{guess}}|_{s=0}$ — too large or too small. In the single-solution region, $-x_c$ monotonically increases with $\kappa_0^{\mathrm{guess}}|_{s=0}$. In the bifurcation region, $-x_c$ first increases and then decreases with increasing $\kappa_0^{\mathrm{guess}}|_{s=0}$. The black circles denote the proper solution that satisfies the boundary condition in the tube center specified by Eq. 3.8.

We further increase the thickness of precursor film to $h_w/R = 6 \times 10^{-4}$ while fixing the viscosity ratio η. The results are shown in Fig. 3-6. We also observe the saddle-node bifurcation onsets at a critical capillary number Ca_b and ends at the folding capillary number $\mathrm{Ca}_{\mathrm{fold}}$. Fig. 3-6D and E show the map of solution finding. The initial values of interface curvature $\kappa_{s=0}$ are smaller, compared to the case with thinner precursor film (Fig. 3-5D and E).

We then show the influence of h_w on the fluid-fluid interface shape for viscously unfavorable displacement $\eta = 1000$ in Fig. 3-7. Both Ca_b and $\mathrm{Ca}_{\mathrm{fold}}$ increases as h_w

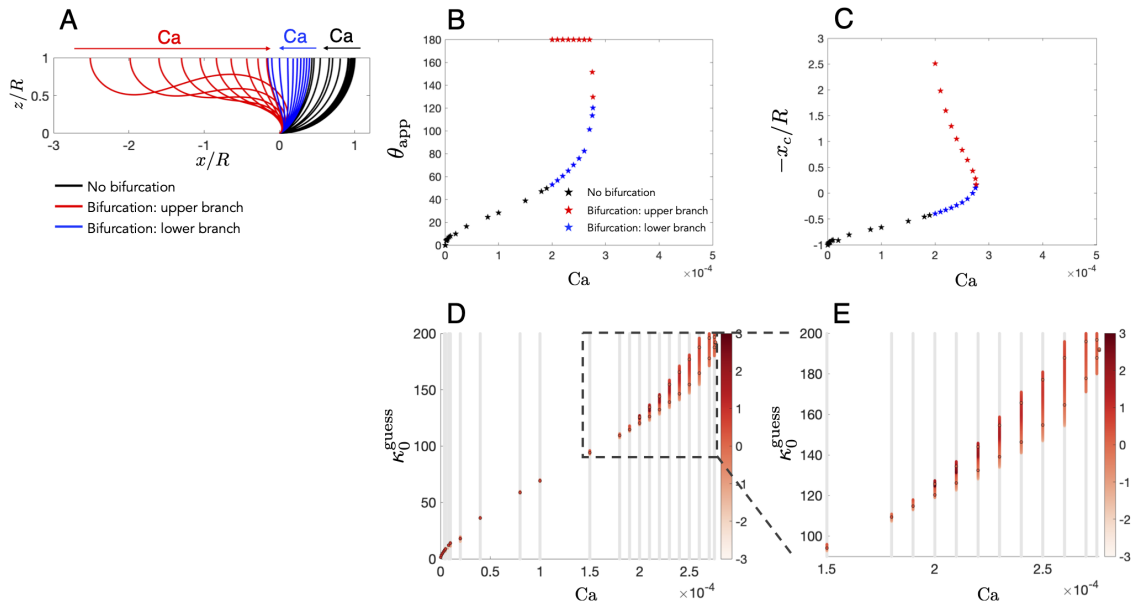

Figure 3-5: (A) Simulated fluid-fluid interface profiles for viscously unfavorable displacement, with viscosity ratio $\eta = 1000$ and precursor film thickness $h_w = 2 \times 10^{-4}$. At low capillary numbers, only one solution exists for a given Ca (black lines). It shows that the interface deforms from its equilibrium shape as Ca increases. Above a critical threshold Ca_b, we find two solutions for a given Ca: blue lines denote lower branch of solution where the interface continues to deform as Ca increases; red lines denote upper branch of solution, where interface shrinks back as Ca increases. (B) Dynamic contact angles θ_{app}, that quantify the fluid-fluid interfaces shown in (A), monotonically increases with Ca in single-solution region. In the bifurcation region, the lower branch of the solution shows that θ_{app} increases with Ca, while the upper branch of the solution shows that θ_{app} shoots 180° immediately. (C) The saddle-node bifurcation is represented by x_c, location of the interface at the tube center x_c, as a function of control parameter Ca measured from the results in (A). (D) The x_c map shows the solution finding procedure. At each Ca, we search for the solution by guessing the interface curvature at the precursor film surface $\kappa_0^{\mathrm{guess}}|_{s=0}$. One value of $\kappa_0^{\mathrm{guess}}|_{s=0}$ determines one interface shape that is quantified by its location at the tube center x_c. The black circles denote the proper solution that satisfies the boundary condition in the tube center specified by Eq. 3.8. The light gray denotes that simulated interface does not reach the tube center. (E) Enlarged view of the bifurcation region in (D).

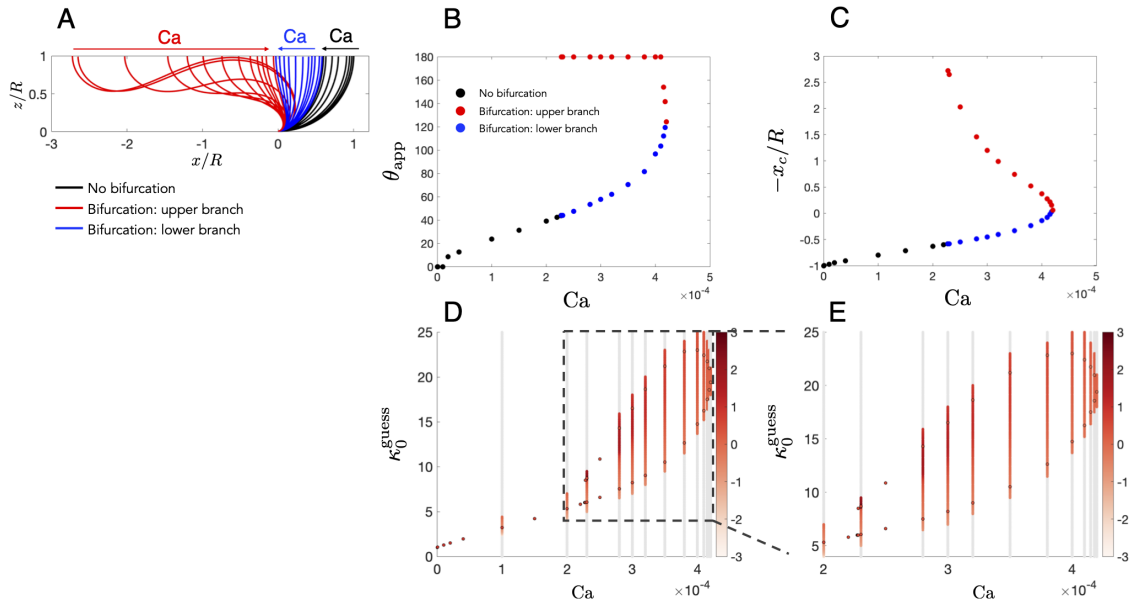

Figure 3-6: (A) Simulated fluid-fluid interface profiles for viscously unfavorable displacement, with viscosity ratio $\eta = 1000$ and precursor film thickness $h_w = 6 \times 10^{-3}$. The solution exhibits saddle-node bifurcation as we observed in Fig. 3-5. The saddle-node bifurcation is represented in terms of dynamic contact angle θ_{app} (B) and location of interface in the tube center x_c (C). (D) and (E) shows the x_c map of solution finding by guessing the interface curvature at the precursor film surface $\kappa_0^{\text{guess}}|_{s=0}$.

increases. The length bifurcation region $\text{Ca}_{\text{fold}} - \text{Ca}_b$ also increases with h_w.

3.4.3 Comparison with experimental observations

Here we compare the predictions from the hydrodynamic model with our experimental observations. Fig. 3-8A shows that our hydrodynamic model captures the dynamic contact angles well for viscously favorable displacement under different capillary numbers and thickness of precursor film. Using the scaling factors shown in Fig. 3-2E, we collapse the experimental data and modeling data onto a single curve that is described by Cox-Voinov's law in Eq. 3.3.

Fig. 3-9 shows the comparison between experiments (circles) and theory (stars) for viscously unfavorable displacement with $\eta = 1000$ and $h_w/R = 2 \times 10^{-4}$. Interestingly, the physical system does not follow the trajectory of lower branch. Instead, it skips all the bifurcated trajectories and jumps to the most unstable upper branch of the solutions. Beyond the transition, the fluid-fluid interface destabilizes as a finger

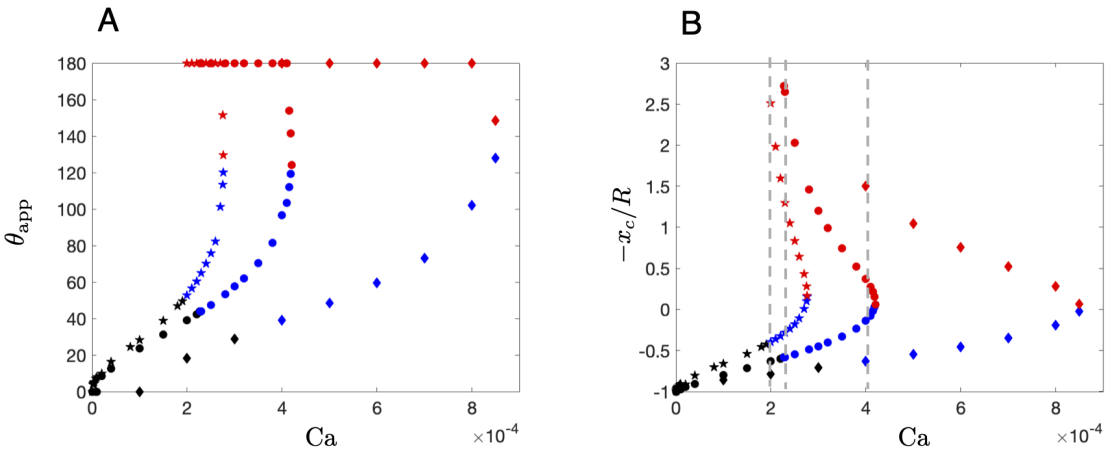

Figure 3-7: The influence of precursor film thickness on the viscously unfavorable displacements $\eta = 1000$. Simulated dynamic apparent contact angle θ_{app} as a function of capillary number for different precursor film thickness $h_w/R = 2 \times 10^{-4}$ (star symbol), $h_w/R = 6 \times 10^{-4}$ (circle symbol) and $h_w/R = 6 \times 10^{-3}$ (diamond symbol). Simulated x_c, the location of interface at the tube center, as a function of capillary number, with same parameters shown in (A). As h_w increases, the starting point of saddle-node bifurcation delays.

and the system enters the transient state. The experimentally measured transition threshold matches well with the Ca_b, which onsets the bifurcation solution, predicted by the hydrodynamic theory.

3.5 The formation of pilot film in a rough capillary tube

In a summary, we have experimentally observed and theoretically rationalized the emergence of sharp wetting transition accompanied by the formation of trailing film for viscously unfavorable imbibition in a smooth confinement. What causes the formation of pilot film, as is observed by Ref. (Levaché & Bartolo, 2014), remains unclear. To unravel the mechanism of this pattern formation, we conduct experiments in a capillary tube coated with NOA81 polymer. The coating technique can be found in Ref. (Primkulov *et al.*, 2020*b*). The NOA81 has recently be observed to exhibit some surface roughness. We use the same liquids and follow the same experimental

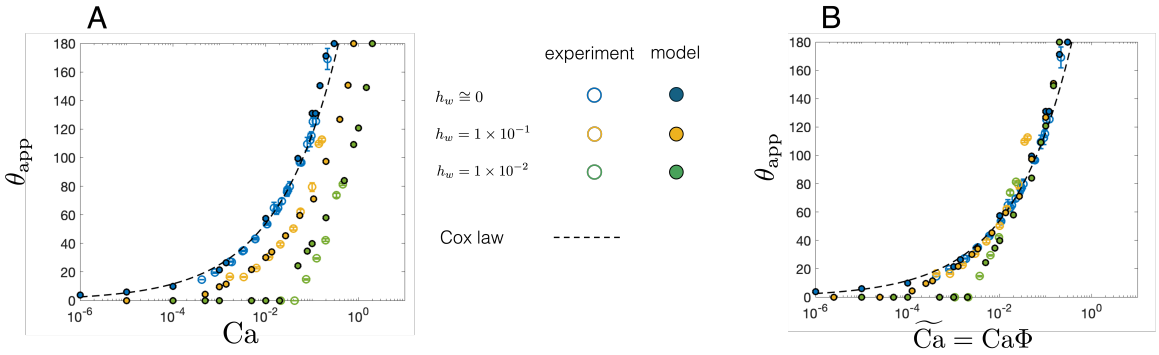

Figure 3-8: (A) Comparison between experimental measurements (open symbols) and predictions from hydrodynamic model (filled symbols), for viscously favorable displacement $\eta = 0$. The blue color denotes vanishingly thin precursor film ($h_w/R = 0$ for experiments and $h_w/R = 1 \times 10^{-5}$ for hydrodynamic model). Yellow color denotes the precursor film thickness $h_w/R = 1 \times 10^{-2}$ and green color denotes $h_w/R = 1 \times 10^{-1}$. (B) Rescale the capillary numbers using the factor shown in Fig. 3-2E.

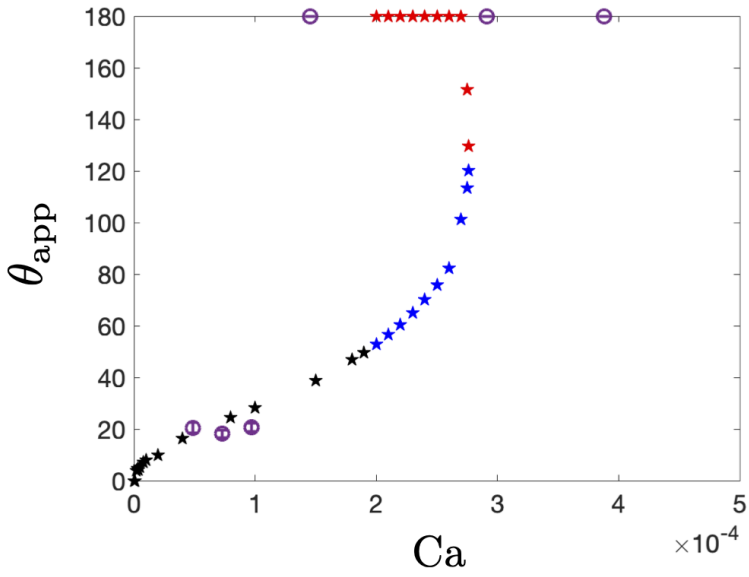

Figure 3-9: (A) Comparison between experimental measurements (open purple circles) and predictions from hydrodynamic model (filled stars) for viscously unfavorable displacement $\eta = 1000$ and precursor film thickness $h_w/R = 2 \times 10^{-4}$.

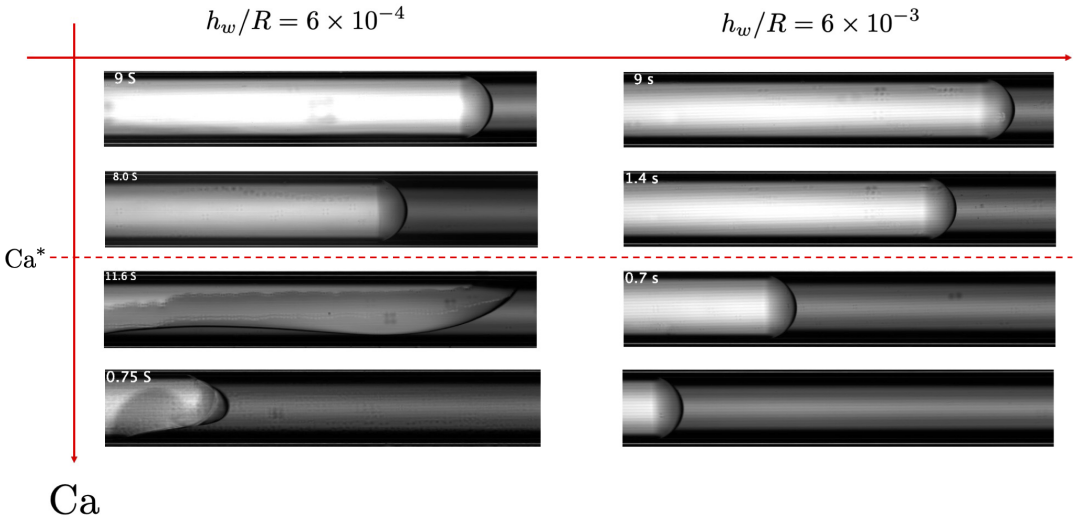

Figure 3-10: (A) Fluid-fluid interface of water (dark gray, $\mu_{\text{wetting}} = 1$ mPas) displacing silicone oil (light gray, $\mu_{\text{nonwetting}} = 1000$ mPas) in a NOA81-coated capillary tube. The phase diagram is obtained under increasing capillary numbers (top to bottom) and two different precursor film thickness $h_w/R = 6 \times 10^{-4}$ (left column) and $h_w/R = 6 \times 10^{-3}$ (right column). At low capillary numbers, the fluid-fluid interface moves with a stable shape. At sufficiently high Ca $>$ Ca*, for smaller h_w, the fluid-fluid interface destablizes and the invading liquid progates along the tube wall as a leading film. While for thick precursor film, the fluid-fluid interface remains stable at highest Ca tested in our experiments.

procedure as those described in Fig. 3-3. Fig. 3-10 shows the fluid-fluid interface of water displacing more viscous silicone oil in a rough capillary tube, under different capillary numbers and thickness of precursor film. At low capillary number, the fluid interface travels downstream with a stable shape, consistent with the observations in a smooth capillary tube (Fig. 3-3A). At high capillary number, we observe a remarkably different type of interface instability, where the invading fluid preferentially advances along the tube wall as a pilot film. This observation agrees with the experiment by Ref. (Levaché & Bartolo, 2014). In a rough capillary tube, the onset of pilot film instability delays as the precursor film becomes thicker (Fig. 3-10). This delay indicates that the formation of pilot film is governed by the interplay between roughness amplitude and prewetting layer height.

Part II

Fluid-fluid displacement patterns in a microfluidic fracture

Chapter 4

Drainage in a microfluidic fracture

Abstract

Immiscible fluid-fluid displacement in confined geometries is a fundamental process occurring in many natural phenomena and technological applications, from geological CO_2 sequestration to microfluidics. Current descriptions of fluid invasion often ignore the interactions between the liquid and the solid walls and assume complete fluid displacement on the microscale. If the displacement rate is sufficiently high, however, a wetting transition occurs, leaving thin films of the defending fluid on the confining surfaces. While most real surfaces are rough, fundamental questions remain about the type of fluid-fluid displacement that can emerge in a confined, rough geometry. Here, we study immiscible displacement in a microfluidic device with a precisely-controlled structured surface as an analogue for a rough fracture. We analyze the influence of the degree of surface roughness on the wetting transition and formation of thin films of the defending liquid. We show experimentally that roughness affects both the stability and dewetting dynamics of thin films, leading to distinct late-time morphologies of the undisplaced (trapped) fluid. Finally, we discuss the implications of our observations for geologic and technological applications.

4.1 Introduction

Immiscible fluid-fluid displacement in geometrical confinement occurs in many natural and engineering processes, including water infiltration into soil (Hill & Parlange, 1972), oil recovery (Orr Jr & Taber, 1984), fuel cell water management (Yang *et al.*, 2004), and microfluidics (Whitesides, 2006; Stone *et al.*, 2004).

Many experimental and computational studies have shown that the fluid invasion

during these processes can range from compact pattern to fractal pattern including viscous fingering and capillary fingering on the macroscopic scales (Saffman & Taylor, 1958; Paterson, 1981; Li *et al.*, 2009; Chen & Wilkinson, 1985; Lenormand *et al.*, 1988; Homsy, 1987; Stokes *et al.*, 1986; Zheng *et al.*, 2015; Gao *et al.*, 2019*b*). These coarse-grained descriptions of displacement often discard the details of the interactions between the liquids and the solid walls and assume complete fluid displacement on the microscale. It has recently been shown, however, that in the presence of moving contact lines the dynamics on the microscale are rate-dependent, with complete displacement at low displacement rates and incomplete displacement at sufficiently high displacement rates (Zhao *et al.*, 2018). The transition between these two regimes is accompanied by the formation of thin films of the defending liquid on the solid surface, which later dewet from the substrate and lead to pinch-off and the formation of disconnected bubbles and drops (Zhao *et al.*, 2018; Pahlavan *et al.*, 2019).

The consequences of this wetting transition on macroscopic patterns remain poorly understood. Previous studies focused on smooth surfaces (Snoeijer & Andreotti, 2013; Redon *et al.*, 1991; Oron *et al.*, 1997), while in fact most real surfaces and porous media are rough. Here we investigate the influence of roughness on the wetting transition on both microscopic and macroscopic length scales. We show that roughness leads to the emergence of new regimes that are absent on smooth surfaces.

We demonstrate that roughness significantly reduces the flow rate threshold for the onset of the wetting transition. Above this threshold, we observe two distinct regimes: (a) the thin-film regime, where the displaced fluid is trapped in the crevices of the rough surface, and (b) the thick-film regime, where the displaced fluid fully covers the rough surface. We delineate these three distinct regimes—complete displacement, thin-film and thick-film—in the form of a phase diagram, and explain theoretically the crossovers among the regimes. We then show that the different hydrodynamics regimes lead to different late-time morphologies of the undisplaced (trapped) defending fluid.

4.2 Experimental Setup

We conduct our experiments in radial Hele-Shaw cells (Fig. 5-1A), consisting of two parallel circular plates, separated by spacers of thickness B. The radial geometry has been used extensively in the study of nonlinear pattern formation (Paterson, 1981; Måløy *et al.*, 1985; Daccord *et al.*, 1986; Ben-Jacob & Garik, 1990; Bazant *et al.*, 2003; Li *et al.*, 2009; Bischofberger *et al.*, 2014; Zheng *et al.*, 2015; Gao *et al.*, 2019*b*). While it introduces some arbitrariness in the definition of the capillary number, it eliminates the boundary effects that plague the rectilinear cell experiments, both from the lateral walls and lack of uniformity in the "frontal" injection. We make one plate's surface rough by patterning it with a regular honeycomb array of cylindrical posts of height b (Zhao *et al.*, 2016) (SI Appendix, section 1.A). The dimensions of the pore throat $w = 0.2$ mm and post diameter $d = 0.8$ mm are fixed in our study, which yields two constant quantities: (1) post density, defined as the areal fraction taken by the posts $\phi_s = \frac{\pi}{2\sqrt{3}}(\frac{d}{w+d})^2 = 0.58$; (2) post-pattern porosity $\phi = 1 - \phi_s = 0.42$. The injection port is at the center of the rough plate, and is surrounded by a circular region without posts of diameter $w_{\text{inj}} = 4.4$ mm (Fig. 5-1B). We use silicone oil with viscosity $\mu_o = 500$ mPa·s as the defending liquid and deionized water with viscosity $\mu_w = 0.99$ mPa·s as the invading fluid. We measure the liquid-liquid interfacial tension to be $\gamma = 13$ mN/m. The static contact angle of water immersed in silicone oil is $\theta_E = 123 \pm 5°$, indicating that water is less wetting to the solid surfaces. We add a light-absorbing dye to the oil phase for visualization and quantification of the film thickness using the light intensity (SI Appendix, section 1.B).

We investigate the roles of three variables: (1) the injection rate (Q in the range $[2 \times 10^{-2}, 2 \times 10^{2}]$ mm^3/s), (2) the aperture of the fracture (gap thickness B in the range [0.15, 0.76] mm), and (3) the amplitude of the surface roughness (post height b in the range [0, 0.135] mm). The aperture B is the characteristic height of the flow channel, which determines the single-phase hydraulic conductivity (Zimmerman & Bodvarsson, 1996) and capillary pressure gradient along the displacement direction (Zheng *et al.*, 2015). The post height b is chosen as the characteristic roughness

height, a quantity that is known to impact the effective contact angle (Herminghaus, 2000; Yang *et al.*, 2006; Quéré, 2002) and slip length (Priezjev, 2007; Kamrin *et al.*, 2010; Vinogradova & Belyaev, 2011; Rothstein, 2010).

In each experiment, the cell is first saturated with silicone oil. Then, water is injected into the cell at a constant injection rate Q. We characterize the displacement dynamics of each experiment using the injection capillary number $\mathrm{Ca}_{\mathrm{inj}} = \frac{v_{\mathrm{inj}}\mu_o}{\gamma}$, where $v_{\mathrm{inj}} = \frac{Q}{\pi w_{\mathrm{inj}}(B+b\phi)}$ is defined at the entrance of the post pattern. We vary $\mathrm{Ca}_{\mathrm{inj}}$ from 10^{-3} to 4.2. Since water displaces oil radially outwards and the front velocity decays away from the center, we also define a local capillary number, $\mathrm{Ca} = \frac{v\mu_o}{\gamma}$, to represent the local competition between the viscous and capillary forces, where v is the measured local displacement front velocity (SI Appendix, section 1.C).

4.3 Experimental Results

We show images of a typical experiment (under conditions $\mathrm{Ca}_{\mathrm{inj}} = 0.725$, $b = 0.08$ mm and $B = 0.5$ mm) before water injection, shortly after water breakthrough, and at late times, in Fig. 5-1C. The displacement front is unstable to the viscous fingering instability due to the smaller viscosity of the invading fluid (Paterson, 1981; Homsy, 1987). Films of the viscous defending liquid are left behind the displacement front and deposited on both the rough and smooth substrates (red and green arrows in Fig. 5-1C). At late times, these films dewet from the substrates, forming persistent clusters along the pathway of the invading fluid (circled regions in Fig. 5-1C). The formation and evolution of films on the smooth surface have been well-studied (e.g., (Zhao *et al.*, 2018)), and we discuss them in the context of our hybrid smooth plate – rough plate system in the SI Appendix, section 7. Here we focus on analyzing the films on the rough surface of the cell.

4.3.1 Regimes of Fluid-Fluid Displacement

We demonstrate the different regimes of fluid-fluid displacement with three representative experiments conducted on the same geometry ($B = 0.5$ mm; $b = 0.08$ mm).

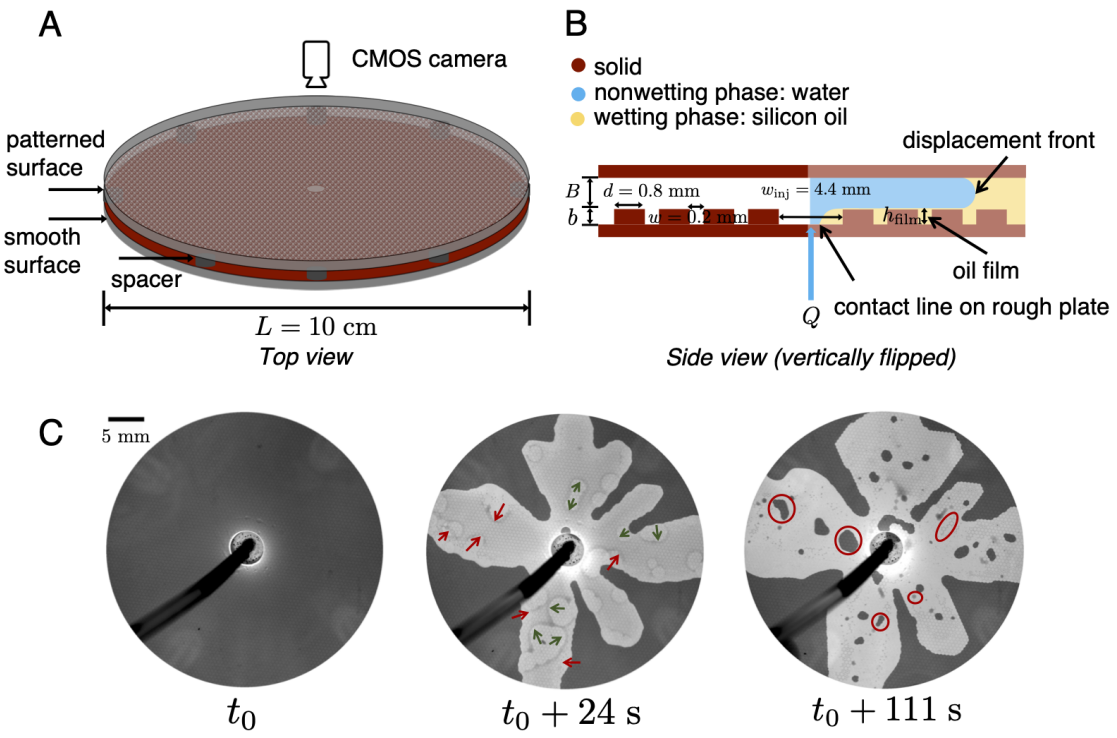

Figure 4-1: We inject water into a rough Hele-Shaw cell filled with viscous silicone oil at constant injection rate Q. (A) Schematic figure of experimental system. We take images of the experiment from above with a CMOS camera, measuring the gap-averaged oil saturation at high spatial and temporal resolution after calibration of the light intensity. (B) Cross-section of the rough Hele-Shaw cell. The rough plate is patterned with a regular honeycomb lattice of cylindrical posts with pore diameter $d = 0.8$ mm, pore throat $w = 0.2$ mm. The fluid is injected at the center of the cell, within a post-free circular region of diameter of $w_{\text{inj}} = 4.4$ mm. (C) Sequence of images from a typical experiment with $\text{Ca}_{\text{inj}} = 0.725$; $b = 0.08$ mm; $B = 0.5$ mm. Less viscous water displacing more viscous silicone oil results in viscous fingering. A film of undisplaced residual oil is left behind the displacement front. This film dewets on the rough surface (red arrows at $t_0 + 24$ s), and at late times leads to clusters of trapped oil (red circles at $t_0 + 111$ s).

At low capillary number (local Ca ≈ 0.0008 in Fig. 4-2A), we observe a complete displacement, with only very small droplets of oil trapped behind the posts (Lee *et al.*, 2017) (Fig. 4-2B-C, Movie S1).

At intermediate capillary number (local Ca ≈ 0.02 in Fig. 4-2D), we observe a thin film of undisplaced oil of thickness roughly equal to the post height b (see the measured thickness in circled red dot in Fig. 4-3): the top surface of the posts is exposed to the invading fluid. This film dewets with the residual viscous fluid retracting as a film of

uniform thickness and confined within the post pattern (Fig. 4-2E-F, Movie S2). In contrast with classical dewetting on smooth surfaces, this film dewets with sub-linear dynamics (SI Appendix, Fig. S3A). We call this regime the *thin-film* regime.

At sufficiently high capillary number (local Ca $\approx$ 0.05 in Fig. 4-2G), the film thickness increases to be larger than the post height b (see the measured thickness in circled red dot in Fig. 4-3), and the undisplaced oil completely covers the solid surface (SI Appendix, section 1.D). This film is not stable and dewets on the rough surface, similarly to how it dewets on a smooth surface (Redon *et al.*, 1991; Zhao *et al.*, 2018): the residual liquid retracts at a constant velocity (SI Appendix, Fig. S3B) and a rim is formed next to the dewetting front (Fig. 4-2H-I, Movie S3). We call this regime the *thick-film* regime.

4.3.2 Fluid Film Thickness and Transitions Among Regimes

In order to characterize the transitions among the three displacement regimes, we measure the local velocity v of the displacement front and employ the local capillary number Ca (SI Appendix, section 1.C), as well as the film thickness of the residual fluid h_{film} (SI Appendix, section 1.B).

In the absence of posts, i.e., for a smooth surface with $b = 0$, at low capillary numbers the displacement is complete and no film is left behind. As the capillary number increases beyond a critical value set by the onset of forced wetting transition (Zhao *et al.*, 2018) (blue dashed line in Fig. S9), a thin film of the defending fluid becomes entrained on the walls. The thickness of this film increases monotonically with capillary number, as predicted by the extended Bretherton model (blue stars and blue solid line in Fig. 4-3).

In the presence of roughness, the dependence of film thickness on the capillary number changes qualitatively. For the case with $b = 0.08$ mm and $B = 0.5$ mm (red dots in Fig. 4-3), at low capillary numbers we observe a complete displacement similar to that of smooth surface. Beyond a critical capillary number, $\text{Ca}_{\text{c,tf}}$, however, the entrained film thickness jumps discontinuously to a value slightly smaller than the post height ($h_{\text{film}} \approx b$). As the capillary number increases further beyond a

second critical capillary number, $\mathrm{Ca}_{\mathrm{c,Tf}}$, the film height becomes larger than the post height and thick films of the defending fluid coat the rough surface. This transition from the thin-film to the thick-film regime has also been observed in the context of the Landau–Levich–Derjaguin problem, where unconfined rough solid surfaces were withdrawn from a liquid bath (Seiwert *et al.*, 2011).

As we increase the roughness further, i.e., for the case with $b = 0.135$ mm and $B = 0.5$ mm (yellow diamonds in Fig. 4-3), we observe yet another qualitatively distinct coating behavior. In this case, the defending liquid becomes entrained in between the posts even at vanishingly small capillary numbers ($\mathrm{Ca} \to 10^{-4}$), i.e., the complete displacement regime is not observed. As the capillary number increases beyond the $\mathrm{Ca}_{\mathrm{c,Tf}}$ the entrained film becomes thicker than the post height and the thick film coating regime is observed.

4.4 Analysis and Discussion

Here, we distill our experimental observations and provide theoretical arguments that rationalize the different coating regimes as well as the late-time fluid trapping. We delineate them in the form of a phase diagram in terms of three dimensionless numbers: (1) the injection capillary number $\mathrm{Ca}_{\mathrm{inj}}$, (2) the roughness-to-aperture-height ratio b/B, and (3) the roughness factor $r = 1 + \frac{4(1-\phi)b}{d}$, which is defined as the ratio of the real area of the rough surface over its projected area. The experimental parameters and the dimensionless numbers of the data used in the phase diagrams (Fig. 4-4) are listed in Table 1 in the SI Appendix.

4.4.1 Fluid Configuration in the Microfluidic Roughness

We first discuss the influence of geometry (b/B and r) on the stability of the entrained thin films.

Geometric criterion for the formation of thin films

In the thin-film configuration (Fig. 4-2F), the oil bridges neighboring posts and the oil-water interface is pinned at the posts' edges with a local angle θ_{edge}, and bowing into the pattern with a penetration length δh due to the Laplace pressure (Keiser *et al.*, 2019; Queralt-Martín *et al.*, 2011). We assume pressure equilibrium between the oil meniscus in the post and the defending fluid ahead of the displacement front, such that the Laplace pressure is $P_{\text{Lap}} = 2\gamma \cos\theta / B$. Larger Laplace pressure or gap thickness would result in smaller local angle at the edge and deeper penetration that may destablize thin films. On one hand, the interface depins when the local angle is smaller than the equilibrium contact angle. On the other hand, when the penetration depth δh is larger than the post height b, the interface touches the bottom surface and the meniscus between the posts cannot form. Thus, two conditions must be simultaneously satisfied for the formation of thin films: $\delta h < b$ and $\theta_{\text{edge}} > 180^\circ - \theta_E$. To compute δh and θ_{edge}, we simulate the 3D shape of the meniscus in the post pattern based on energy minimization using `Surface Evolver` (Brakke, 1992). By setting $\theta_{\text{edge}} = 180^\circ - \theta_E$ and $\delta h = b$, we arrive at the following geometric criterion (SI Appendix, section 2):

$$r_{c,1} = \max\left\{\beta_1 \frac{b}{B} + 1, \quad \beta_2 \Big(\frac{1}{\cos\theta_E}\frac{B}{b} - 1\Big)^{-\frac{1}{2}} + 1\right\}, \tag{4.1}$$

in which $\beta_1 = 0.87$ and $\beta_2 = 0.55$. It indicates that thin films of the defending fluid can only form in the post patterns if the roughness factor is larger than this critical value, $r > r_{c,1}$ (Fig. 4-4A). Otherwise, the oil meniscus between posts quickly retracts from the center of each pore and moves along the pore throats, and thus no continuous thin film can be left behind the displacement front.

Energetic stability of the entrained thin films

Whether the entrained thin films of the defending liquid dewet from the rough surfaces is determined by comparing the free energy of the coated and dewetted states. The coated state is akin to the Cassie state (Quéré, 2008), where a water drop only touches

the top of the posts and does not fill the space between the post pattern. The dewetted state is akin to the Wenzel state (Wenzel, 1936), where the drop fills all the spaces between the post pattern. Therefore, the coated state is stable if the free energy of the Cassie state is lower than the free energy of the Wenzel state, i.e., the dewetted state (SI Appendix, section 3). Equating the free energy of these two states, we arrive at the following critical amplitude of roughness:

$$r_{c,2} = 1 - \frac{\phi(1+\cos\theta_E)}{\cos\theta_E}, \tag{4.2}$$

which suggests that if $r > r_{c,2}$, the entrained thin films are stable and will not dewet from the post pattern (Fig. 4-4A).

4.4.2 Forced Wetting Transition

Even when the geometric criterion (Eq. 4.1) is satisfied, a thin film is observed only when the capillary number is above a critical value (red symbols in Fig. 4-3). We rationalize the transition from complete displacement to thin film by calculating the critical threshold $\mathrm{Ca}_{\mathrm{c,tf}}$ for the onsets of the wetting transition (Zhao *et al.*, 2018). At $\mathrm{Ca}_{\mathrm{c,tf}}$, the meniscus of the fluid-fluid displacement front is deformed and the apparent contact angle of the nonwetting phase reaches 180°. Beyond this critical value, the defending oil is forced to wet the rough plate as a film.

To obtain the critical capillary number at the onset of the wetting transition, we solve the Stokes equations using the generalized lubrication approximation, and balance the viscous stresses and Laplace pressure jump across the interface to arrive at (Chan *et al.*, 2013; Levaché & Bartolo, 2014; Zhao *et al.*, 2018):

$$\frac{d^2\theta}{ds^2} = \frac{3\mathrm{Ca}f(\theta,R)}{z(z+3\lambda_s)}, \tag{4.3}$$

where θ is the local interface slope, s is the arc length along the interface, $M = \mu_w/\mu_o$ is the viscosity ratio between water and oil, λ_s is the slip length (on the order of nanometers) introduced to resolve the contact-line singularity (Huh & Scriven,

1971). The function $f(\theta, R)$ is from Cox's solution (Cox, 1986; Chan *et al.*, 2013). The differential equation is solved with the boundary conditions: $\theta|_{s=0} = \theta^*$, $z|_{s=0} = 0$, $\theta|_{s=1} = \pi/2$ and $z|_{s=1} = h^*$. Here, we account for the change in the apparent contact angle on a rough surface, which we denote as θ^* (SI Appendix, section 3; Fig. S6D). The height h^* represents the location across the gap, where the interface slope becomes $\pi/2$. Since only one of the plates in our cell is rough, the apparent contact angles at the top and bottom plates are different, leading to an asymmetric meniscus profile across the gap; h^* is no longer equal to the half-cell height. Instead, we determine h^* by pre-solving the meniscus shape across the whole channel at equilibrium (SI Appendix, section 4.A). We assume h^* is unchanged even if the capillary number changes.

The critical capillary number $\mathrm{Ca_{c,tf}}$ predicted by Eq. 4.3 for $b = 0.08$ mm is shown in Fig. 4-3 (SI Appendix, section 4.B). We note that the thin film generated near the injection port, where the front velocity is above the threshold $\mathrm{Ca_{c,tf}}$, would not catch up and merge with the advancing fluid-fluid front in a radial cell even though the front velocity decays with distance from the center. The viscous residual oil inside the thin film drains away slowly due to the high viscosity and low interfacial driving force (see the calculations in SI Appendix, section 5). Thus, to predict the occurrence of thin film in a radial cell experiment, we require the capillary number at injection to be larger than the critical threshold, i.e., $\mathrm{Ca_{inj}} > \mathrm{Ca_{c,tf}}$ (Fig. 4-4B).

For very rough surfaces, i.e., when $r > r_{c,2}$ (Eq. 4.2), the defending fluid cannot be removed from the post pattern, as these films become energetically stable. Therefore, the complete displacement regime cannot be observed on very rough surfaces even at vanishingly small capillary numbers, as shown in Fig. 4-3 and Fig. 4-4B.

4.4.3 Transition to a Thick Film

As the capillary number increases, the entrained film height becomes larger than the post height, indicating a transition from the thin-film to the thick-film regime. We calculate the film thickness in this transition using the lubrication approximation and assume that the flow in between the posts is horizontal, and that it is governed by

Darcy's law (see the derivation in the SI Appendix, section 6). Under this assumption, the flux of film flow is still linearly proportional to the pressure gradient and hence the presence of a rough surface only modifies the coefficient of the classical Bretherton law (Bretherton, 1961). Equating the film thickness to the post height, we obtain the critical capillary number for the onset of the thick-film regime: $\mathrm{Ca}_{\mathrm{c,Tf}} = \frac{\phi}{\tau}\left[\frac{b}{0.67(b+B)}\right]^{3/2}$, where $\tau = 1.8$ is the flow path tortuosity in our case (Duda *et al.*, 2011). The result for the case $b = 0.08$ mm is plotted in Fig. 4-3.

Since the front velocity decays with distance from the cell center, the thickness of the entrained film also decreases in a radial cell experiment. It indicates that the thick film generated near the injection port may transition to a thin film as the fluid-fluid front advances. In our experiments, we identify the displacement regime based on the observation window, which is placed at approximately half the cell radius. In such window, the velocity does not vary much, and we avoid observing two different displacement regimes. Thus, we require the capillary number at the radius $L/4$ to be larger than the critical value $\mathrm{Ca}_{\mathrm{c,Tf}}$, i.e., $\mathrm{Ca}_{\mathrm{inj}}\frac{4w_{\mathrm{inj}}}{L} \geq \mathrm{Ca}_{\mathrm{c,Tf}}$. We then obtain the second critical injection capillary number for the observation of thick film around the half radius of a cell:

$$\mathrm{Ca}_{\mathrm{inj,Tf}} = K\Big(\frac{b}{B+b}\Big)^{\frac{3}{2}}. \tag{4.4}$$

The constant coefficient is $K = 0.67^{-3/2}\frac{\phi}{\tau}\frac{L}{4w_{\mathrm{inj}}} = 4.8$. This critical Ca simultaneously depends on the varying experimental parameters b and B, in agreement with the experimental data in the phase diagram as a function of b/B and $\mathrm{Ca}_{\mathrm{inj}}$ (Fig. 4-4C).

4.4.4 Phase Diagram

We represent equations 4.1, 4.2, 4.3 and 4.4 in a 3-dimensional parameter space (Fig. 4-5), to demonstrate how the interplay between roughness factor r, vertical aspect ratio b/B and injection capillary number $\mathrm{Ca}_{\mathrm{inj}}$ govern the crossovers between the different regimes: complete displacement, thin film (dewetting, stable, unstable) and thick film.

The geometric parameters (b/B and r) determine the stability of the thin film: for $r < r_{c,1}$ (light blue plane), the thin film is unstable and cannot form at any flow rate (tf-u); for $r > r_{c,2}$ (gray plane), the thin film is energetically stable and does not dewet (tf-s); for $r_{c,2} > r > r_{c,1}$, the entrained thin film can dewet after it forms (tf-d).

The injection capillary number further controls the displacement regimes: complete displacement (cd) transitions to thin film (tf) when $\mathrm{Ca_{inj}} > \mathrm{Ca_{inj,tf}}$ (red plane), and then to thick film (Tf) when $\mathrm{Ca_{inj}} > \mathrm{Ca_{inj,Tf}}$ (green plane). $\mathrm{Ca_{inj,tf}}$ is vanishingly small in the tf-s region. We note that the entrainment behavior in the tf-u region is similar to that on smooth surfaces: above the critical threshold (red plane), complete displacement transitions to the classic Bretherton film.

4.4.5 Residual Fluid Morphology at Late Times

The different regimes in the phase diagram (Fig. 4-5) lead to distinct trapped residual fluid morphologies at late times (Fig. 4-6).

Residual microdroplets and throat-bridges (Fig. 4-6A) and residual lubrication films (Fig. 4-6B) are observed in the thin-film dewetting regime. Residual microdroplets and throat-bridges form as a result of snap-off events on the edge at the base of the cylindrical posts when the dewetting front of the thin film retracts through the throats. A residual lubrication film is an isolated cluster that is confined within the post pattern while the top of the post is exposed to the invading liquid. It is formed when the connection between the thin film and the bulk oil is cut off by dewetting and later the thin film retracts. When the thin film is stable (tf-s in Fig. 4-5), dewetting does not occur and the lubrication film remains within the roughness in the whole cell (Fig. 4-6C).

Residual liquid caps (Fig. 4-6D) and residual liquid bridges (Fig. 4-6E) are observed in the thick-film dewetting regime, during which a rim is formed to collect the retracting liquid that coats the patterned surface. A liquid cap is an isolated droplet that covers an entire post. It forms when the connection between thick film and bulk oil is cut off during dewetting and the disconnected thick film then retracts. When the oil volume in such disconnected film is sufficiently large, the rim in the dewetting

front grows to touch the smooth plate and forms a liquid bridge between the two plates.

4.5 Conclusion

In this study, we show the essential role of roughness in controlling the fluid-fluid displacement and fluid trapping in fractured media. We do so by means of laboratory experiments on patterned microfluidic cells that permit precise control over the confinement and degree of roughness of the fracture analogue. We inject a nonwetting, low-viscosity fluid (water) to displace a wetting, high-viscosity fluid (silicone oil), and identify different displacment regimes.

We demonstrate that roughness significantly lowers the critical capillary number for the onset of the wetting transition, and that for sufficiently strong roughness this wetting transition occurs at vanishingly small capillary number. Above this thershold capillary number, we uncover a heretofore unrecognized thin-film regime in which a film of undisplaced residual oil is left behind entirely within the posts that conform the roughness. This thin film may remain stable or dewet with uniform thickness, deviating from the behavior of classic viscous dewetting on smooth surfaces. The entrained thin film transitions to a thick-film regime at a second critical capillary number, where the liquid fully covers the rough surface. Beyond this critical capillary number, the film height increases with the capillary number according to Bretherton's law. Our theoretical arguments rationalize the crossovers among the displacement regimes—complete displacement, thin film and thick film—in good agreement with our experimental data.

We further show that the different displacement regimes lead to distinct residual fluid morphologies at late times: microdroplets, single-throat bridges and lubrication films in the thin-film regime, and liquid caps and liquid bridges between plates in the thick-film regime. The distribution and morphology of the trapped fluid affects the availability of the nucleation sites and interfacial area, thus possibly controlling long-term biogeochemical reactions in porous and fracture media, which could play

a profound role in natural and engineered subsurface flows like geothermal energy extraction, geological CO_2 sequestration and hydrogen geostorage.

4.6 Supplementary materials

4.6.1 Materials and Methods

Microfluidic Cell Fabrication

The microfluidic-fracture flow cell consists of a rough plate and a smooth plate separated by shims (McMASTER-CARR,Stainless Steel Ring Shim) of a given thickness (that is the gap thickness B). The roughness is created by an array of equal-sized posts arranged on a honeycomb lattice. We fabricate the cells via soft imprint lithography, following (Zhao *et al.*, 2016). Fig. 4-7 illustrates the fabrication processes: (1) we first generate a silicon master of the pre-designed post pattern and post height by photolithography. We spin coat a negative photoresist (SU-8, MicroChem) onto a silicon wafer with different speeds to achieve a film thickness equal to the desired post height (b). After soft baking, we expose the photoresist to UV light through a photomask of the post pattern, which selectively polymerizes the photoresist to form posts. We subject the photoresist to post-exposure-bake, and then dissolved the unexposed areas of the photoresist (pores). (2) We use the silicon master to create PDMS (Sylgard 184, Dow Corning) casts of the post pattern, which forms a negative complement of the silicon master. The posts in the silicon master become wells in the PDMS casts. We use the PDMS casts to structure the cell surface. (3) The surface material of the flow cells is a photocurable polymer (NOA81, Norland Optics). To make the rough plate, we first deposit a puddle of NOA81 onto a glass disc. We allow the NOA81 to spread across the glass disc and then carefully cover it with the PDMS cast such that the NOA81 fully fills the wells in the PDMS cast. Next we expose them to UV light (MA4-1, Karl Suss) for 2 minutes. After solidification, we peel off the PDMS mold, and the glass disc with NOA81 on the surface is ready. (4) The manufacturing of the flat plate is similar, using a flat silicon master (without pho-

tolithography) instead of the textured one. We evenly place 8 shims at the edge of the disks and bind the rough and smooth plates with 4 clamps. On the smooth surface of untreated NOA81, the contact angle of water in ambient silicone oil is $123 \pm 5°$.

Experimental Quantification of Oil-Film Thickness

We seed the injected silicone oil with a light-absorbing dye (ORCOSOLVE OIL RED SBSE, Organic Dyestuffs Corporation) at a concentration corresponding to full solubility. To guarantee the consistency of solubility, we mix the oil with an excess amount of dye and stir them over a magnetic hot plate for 3 hours at constant temperature and pressure. After cooling the oil for 24 hours, we filter the dyed silicone oil with a 0.25 μm mesh.

We experimentally measured transmitted light intensity under different oil thickness. The oil thickness is adjusted by saturating a Hele-Shaw cell with different gap thickness b to generate a calibration curve (Fig. 4-8A). This calibration is consistent with Beer-Lambert's law, which relates the transmittance I/I_0 to the system attenuation μ: $I/I_0 = e^{-\mu}$. ORCOSOLVE dye is the homogeneous attenuating species in the system, with $\mu = \epsilon C b$, where ϵ is the species attenuation coefficient and C is the concentration. As the dye solubility in oil is very low, C is vertically uniform and very small. Mathematically, the Beer-Lambert law can be reduced to a linear relation by Taylor expansion when the attenuation coefficient μ is small. The linear relation provides a good fit to the measured data when $b \leq 0.76$ mm (Fig. 4-8A). All experiments fall in this range. We note that the linearized Beer-Lambert law is applicable when there is a layer of water in the cell. The fluid-fluid interface may introduce refraction and reflection effects in the light intensity. References (Zhao *et al.*, 2016) and (Levaché & Bartolo, 2014) compared the total volume that is inferred by the light intensity (Beer-Lambert's law) and injection rate and showed the error is within 3%. This small error is negligible compared to the error bar we use in Fig. 3 in the manuscript.

The linearized Beer-Lambert's law allows us to convert the measured light intensity to the residual oil amount spatial-temporally ($h_{\text{oil}}(x, y, t)$). We define the film

thickness as the averaged depth of residual oil over the pore body area between posts, and to the bottom of the rough plate. Note that we calculate the local displacement-front velocity at the same location. In Fig. 4-8B, we show the time series of pore-averaged oil thickness ($\overline{h}_{\text{oil}}(t)$), from a typical rough-cell experiment where the oil films are simultaneously deposited on the rough and smooth surfaces behind the displacement front (parameters: $B = 0.5$ mm, $b = 0.08$ mm, $\text{Ca}_{\text{inj}} = 0.22$). We note that the residual films on the two plates often dewet at different times, which indicates there is a period of time when the residual oil only exists on one plate. It is relatively straightforward to distinguish the plate on which the film dewets first, because the shape of the film on the rough surface is always distorted by the pillars while that on the smooth side is not affected by the geometry. In the case shown in Fig. 4-8B, the thin film dewets first on the top smooth plate from stage **b** to **c**, and then the thick film dewets on the bottom rough plate from stage **c** to **d**. The formation of a dewetting rim increases the oil thickness during the transition period. In Fig. 4-8C, we show an example where the wetting transition is triggered only on the rough surface and no film is left on the smooth surface. In this case, it becomes straightforward that $h_{\text{film}}^{\text{rough}}$ is calculated by averaging the $\overline{h}_{\text{oil}}(t)$ over stage **b**.

In a smooth cell, the thin film of defending fluid is formed on both top and bottom plates, which is identical and symmetric around the middle plane of the cell. The film thickness is simply obtained by diving the averaged oil amount in stage **b** by 2.

The above-mentioned measurement introduces errors from the space and time variation of film thickness. We set the error bars as the standard deviation of $\overline{h}_{\text{oil}}$ in stage **b**, which accounts for the maximum variation in both space and time.

Experimental Characterization of Local Displacement-Front Velocity and Dewetting Dynamics

We measure the displacement distance l swept by the advancing fluid-fluid front in direction normal to the front between two time frames t and $t + \Delta t$. The local velocity v is then calculated as $v = \frac{l}{\Delta t}$.

To characterize the dewetting dynamics, we track the area S of a dewetting droplet

by first making the image stacks binary and then using the function "Analyze Particle" in ImageJ. The square root of S is the equivalent dewetting radius r_d. Thin-film dewetting (Fig. 4-9A) follows sublinear dynamics ($r_d \sim t^\alpha$, with $\alpha < 1$), in contrast with the classic thick-film dewetting (Fig. 4-9B) at constant velocity ($r_d \sim t$).

Experimental Identification of Thick Films

An important element of our experimental analysis is the ability to discern the presence of thick oil films, that is, films of the defending fluid that are thicker than the height of the posts. The evolution of the entrained film behind the displacement front is shown in Fig. 2G, and the evolution of the dewetting rim is shown in Fig. 2H. We can unequivocally assert that this involves the presence of a thick film because the residual oil drains from the top of the posts to the throats in between posts, which indicates that the entrained film is thicker than the posts (Fig. 4-10).

4.6.2 Geometric Criterion for the Formation of Thin Films

We investigate the 3D configuration of the thin film using `Surface Evolver`, which is a finite element solver that minimizes the overall energies of the fluid-fluid-solid system (Brakke, 1992). Specifically, we construct one triangular domain with three one-sixth sectors of surrounding posts (red color in Fig. 4-11A). The water-oil interface (green color) is initially flat and hanging at the edge of the neighboring posts. The minimization of two energies — water-oil surface tension $\gamma = 13$ mN/m and prescribed Laplace pressure P_{Lap} — is carried out iteratively until the relative change is less than 10^{-8}. Fig. 4-11B shows an example of the oil meniscus configuration where post height $b = 0.08$ mm and Laplace pressure $P_{\text{Lap}} = 28.32$ Pa (equivalent to gap thickness $B = 0.5$ mm). We define the local angle θ_{edge} using the two points closest to the post edge, shown in Fig. 4-11C. To measure penetration length δh, we place an circular patch in the center of pore body and obtain the water-oil interface height at all points in this circular pore domain $z_{\text{pore}}(x, y)$. An averaged penetration length is then calculated as $\delta h = b - \overline{z}_{\text{pore}}$, where $\overline{z}$ denotes mean value. This definition

is consistent with the experimental measurement method. We compute θ_{edge} and δh for a fixed post height $b = 0.08$ mm and varying pressure, which corresponds to different gap thickness, shown in Fig. 4-11D and 4-11E respectively. The simulation results indicate that $\theta_{\text{edge}} < 180° - \theta_E$ when $P_{\text{Lap}} < 47.2$ Pa. This critical Laplace pressure 47.2 Pa corresponds to the gap thickness $B^* = 0.3$ mm. Thus $B = B^*$ is the geometric criterion for depinning. Combined with the definition of roughness factor ($r = 1 + \frac{4\phi_s b}{d}$), we arrive at the first term in Eq. (1) in the manuscript:

$$r^* = \frac{4\phi_s B^*}{d}\frac{b}{B} + 1 \tag{4.5}$$

where we define $\beta_1 = \frac{4\phi_s B^*}{d} = 0.87$. We experimentally measure the penetration length δh for the same $b = 0.08$ mm and different values of B (black dots in Fig. 4-11E). The `Surface Evolver` simulation agrees well with experimental data.

Next, we derive a semi-analytical relation between penetration length δh and post height B. For the sake of simplicity, we describe the curved oil-water interface as a cap with two identical radii r_{wo}. The pressure balance leads to $\frac{2\gamma}{r_{\text{wo}}} = P_{\text{Lap}} = 2\gamma\cos\theta/B$. From the geometry we relate the radius of curvature to penetration length: $\delta h = r_{\text{wo}} - \sqrt{r_{\text{wo}}^2 - (m/2)^2}$, where m is a fitted parameter equivalent to pore body size in 3D. Therefore the relation between δh and B must be of the form:

$$\delta h = \frac{B}{\cos\theta} - \sqrt{\Big(\frac{B}{\cos\theta}\Big)^2 - \Big(\frac{m}{2}\Big)^2}. \tag{4.6}$$

We obtain $m = 0.379$ mm by least-squares fitting. The semi-analytical model is shown as blue dashed line in Fig. 4-11E. By setting $\delta h = b$, we obtain a geometric criterion $b = \frac{B}{\cos\theta} - \sqrt{\Big(\frac{B}{\cos\theta}\Big)^2 - \Big(\frac{m}{2}\Big)^2}$ for the oil meniscus to touch the bottom surface. Combined with the definition of roughness factor ($r = 1 + \frac{4\phi_s b}{d}$) again, we arrive at the second term in Eq. (1) in the manuscript:

$$r^{**} = \frac{2m\phi_s}{d}\Big(\frac{2}{\cos\theta}\frac{B}{b} - 1\Big)^{-1/2} + 1 \tag{4.7}$$

where we define $\beta_2 = \frac{2m\phi_s}{d} = 0.55$. The degree of roughness has to be larger than

both criteria (Eq. 4.5 and 4.7) for the thin films to form.

4.6.3 Surface Energy Calculation and Static Apparent Contact Angle

Here we show the calculation of surface energy for different states and introduce the definition of static apparent contact angle on the rough surface.

When the displacement takes the dewetted state (Wenzel state, see sketch in Fig. 4-12A), the variation in surface energy from the front advancing a distance dx is: $dE_W = r(\gamma_{\rm sw} - \gamma_{\rm so})dx + \gamma\cos\theta_g dx$, where θ_g is the equivalent contact angle on the rough surface (Wenzel, 1936). This change in surface energy includes the following terms: (1) the oil-solid interface being replaced by water-solid interface, $r(\gamma_{\rm sw}-\gamma_{\rm so})dx$; and (2) the change of water-oil surface area as water invades, $\gamma\cos\theta_g$.

When the displacement takes the coated state (Cassie state, see sketch in Fig. 4-12B), where water advances above the post pattern while the defending oil entrains below as a film, the energy variation is: $dE_C = (1-\phi)(\gamma_{\rm sw} - \gamma_{\rm so})dx + \phi\gamma dx + \gamma\cos\theta_g dx$ (Quéré, 2008). It includes the following terms: (1) the oil-solid interface being replaced by water-solid interface in the top area of posts, $(1-\phi)(\gamma_{\rm sw} - \gamma_{\rm so})dx$; (2) the creation of new water-oil interface between posts, $\gamma\phi dx$; and (3) the change of water-oil surface area as water invades, $\gamma\cos\theta_g$.

The dewetted state (Wenzel state) is selected if it has lower energy variation ($dE_W < dE_C$). Then the static apparent contact angle of the water phase within the post pattern can be determined using Wenzel's law: $\cos\theta^* = r\cos\theta_E$. Analogously, the coated state (Cassie state) is selected if its associated energy variation is lower ($dE_C < dE_W$). The phase invading within the post pattern is equivalent to a completely non-wetting phase, as it does not touch the side surface of posts and the bottom walls. Hence, the apparent contact angle of water phase in the coated state can be viewed as $\theta^* = 180°$. Fig. 4-12D shows the static apparent contact angle of water phase under different roughness geometries, as determined by the aforementioned arguments.

Under criterion $r > r_{c,2}$ (Fig. 4-12D and Eq. (2) in the manuscript), the apparent contact angle of oil phase within the post pattern becomes 0 as water phase contact angle becomes $\theta^* = 180°$. This can be derived by analogy to hemi-wicking (Quéré, 2008) (see sketch in Fig. 4-12C). For an oil film progressing through the posts by a distance dx, the surface energy variation includes: (1) the water-solid interface being replaced by oil-solid interface for the area of posts' side and bottom wall, $(\gamma_{so} - \gamma_{sw})[r - (1 - \phi)]dx$; and (2) the creation of new water-oil interface, $\gamma\phi dx$. We then arrive at the expression for the surface energy variation in the hemi-wicking regime: $dE_h = (\gamma_{so} - \gamma_{sw})[r - (1 - \phi)]dx + \gamma\phi dx$. We note that $dE_h < 0$ when $r > r_{c,2}$. Therefore, the progression of oil into the post pattern is always favorable if the criterion is satisfied, and thus oil within the roughness is, under these conditions, equivalent to a completely wetting fluid.

4.6.4 Meniscus Shape

Boundary Value h^*

To determine the boundary value h^* for the meniscus shape, we first compute the meniscus profile at equilibrium without viscous forces. We set Ca = 0 in Eq. (3) in the manuscript: $\frac{d^2\theta}{ds^2} = 0$, which governs the equilibrium interface shape together with geometric relation $dz/ds = \sin\theta$. We integrate the differential equations over the entire channel (from $z = 0$ to $z = b + B$). Specifically, the boundary conditions are: $\theta|_{s=0} = \theta^*$, $z|_{s=0} = 0$, $\theta|_{s=1} = \theta_E$ and $z|_{s=1} = B + b$. Fig. 4-13A shows the result for the case $b = 0.08$ mm; $B = 0.5$ mm. The apparent contact angle on the rough surface for $b = 0.08$ mm is $\theta^* = 132°$. From its $z - \theta$ relation Fig. 4-13B, we extract that $z(\theta = 90°) = 0.55(B + b)$. Therefore, $h^* = 0.55(B + b)$.

Wetting Transition Threshold

After obtaining the boundary value h^*, we are ready to compute the meniscus profiles under different values of Ca. To do so, we integrate Eq. (3) in the manuscript with geometric relation $dz/ds = \sin\theta$ from the contact line $z = 0$ to $z = h^*$. The detailed

boundary conditions are stated in the manuscript. Fig. 4-13C shows the results for the same case $b = 0.08$ mm; $B = 0.5$ mm. As Ca increases, the fluid-fluid interface deforms from its equilibrium state. This distortion can be quantified by the dynamic apparent contact angle θ_{app}, which is defined as $\theta(s)$ where the interface curvature is minimum. θ_{app} increases with increasing Ca, until it approaches 180° at a critical Ca_c, at which no stable solution to the differential equations can be obtained [Fig. 4-13D]. Ca_c marks the onset of wetting transition ($\text{Ca}_c = 0.08$ in this case)

4.6.5 Thin Film Draining Velocity is Smaller than the Displacement Front Velocity

We estimated the thin film dewetting velocity by conducting a force analysis on a control volume. A simplified scenario is depicted in Fig. 4-14. A short section of thin film is already formed behind the displacement front, as the velocity is above the wetting transition threshold. The left edge of the control volume (upstream) is selected behind the contact line while the right edge (downstream) is chosen immediately behind the displacement front. The top and bottom boundaries are chosen to be slightly higher than the post top and lower than the solid surface, respectively. The interfacial force (per unit width) between solid-oil $F_\gamma^{so} = r\gamma_{so}$ and oil-water $F_\gamma^{wo} = \gamma\phi$ are driving the motion, while interfacial force between solid-water $F_\gamma^{sw} = r\gamma_{sw}$ is opposing the motion, where $r = \phi + \frac{4(1-\phi)h}{d}$ is the roughness factor, as defined in the manuscript. Combined with the Young-Laplace equation $\gamma_{so} + \gamma\cos\theta_E = \gamma_{sw}$, we arrive at the expression for the total interfacial force $F_\gamma = F_\gamma^{wo} + F_\gamma^{so} - F_\gamma^{sw} = \gamma(\phi - r\cos\theta_E)$. The friction force $F_v = b\Delta P$ induced by the motion of residual oil inside the film is acting in the direction opposite to that of flow, where ΔP is the pressure drop along the thin film. As the movement of oil is confined in the roughness, we approximate it as porous media flow and describe it using Darcy's law $v_{\text{tf}} = -\frac{k}{\mu_o}\frac{\Delta P}{\Delta l}$, where $k = \frac{b^2\phi}{3\tau}$ is the 2D porous-media permeability, v_{tf} is the mean oil velocity inside the residual film and Δl is the length of the film. Note that $k_s = b^2/3$ is the permeability on smooth surface that is derived from Stokes equation, which is reduced by the available pore space

in the 2D post pattern (porosity ϕ) and the more tortuous flow paths (tortuosity τ). τ is determined by the porosity value based on the relation proposed in Ref. (Duda *et al.*, 2011): $\tau = 1.8$ in our case. Equating F_γ and F_v gives the velocity of a section of thin film:

$$v_{\mathrm{tf}} = \frac{b\gamma\phi}{3\mu_o\tau\Delta l}(\phi - r\cos\theta). \tag{4.8}$$

Note that the thin-film draining velocity decays with increasing thin-film length. The largest draining velocity $v_{\mathrm{tf,max}}$ occurs when the thin film is shortest, which is one pore unit $\Delta l = 1$ mm.

The fluid-fluid front advancing velocity is calculated as $v_{\mathrm{front}} = Q/(2\pi r(B + \phi b))$, where r is the distance of the displacement front. Given the critical flow rate $Q_{\mathrm{c,tf}}$ that triggers the wetting transition at the injection port, the front velocity becomes lowest when it reaches the outlet of the cell $v_{\mathrm{front,min}} = 2Q_{\mathrm{c,tf}}/(\pi L(B + \phi b))$. This smallest front velocity is much larger than the maximum draining velocity of thin film $v_{\mathrm{front,min}} > v_{\mathrm{tf,max}}$, for any gap thickness B and post height b used in our study. Thus, the entrained thin film cannot catch up and merge with the advancing fluid-fluid front.

4.6.6 Transition from Thin to Thick Film: Modification of Bretherton's Law

Similar to the original derivation of Bretherton's law (Bretherton, 1961), we also use the lubrication approximation to describe film flow on the rough surface. The depth of the defending fluid above the posts is not comparable to the post height in the transition from thin-film to thick-film regime. Thus it is reasonable to further assume that the flow in between the posts is horizontal, and that it is governed by Darcy's law:

$$\overline{u}_{x,\mathrm{rough}} = -\frac{k}{\mu_o}\frac{dP}{dx}, \tag{4.9}$$

where $\overline{u}_{x,\mathrm{rough}}$ is a depth-averaged horizontal velocity. The equivalent permeability is taken as $k = \frac{h^2}{3}\frac{\phi}{\tau}$, that is, the permeability of a film on a smooth surface, $h^2/3$,

reduced by the effects of having less available space (porosity $\phi = 0.42$ in our study) and more tortuous flow paths (tortuosity $\tau = 1.8$ in our case). Thus, the flux on the rough surface is written as:

$$q_{\text{rough}} = \overline{u}_{x,\text{rough}} h = -\frac{h^3}{3\mu_o}\frac{\phi}{\tau}\frac{dP}{dx}. \tag{4.10}$$

Note that this flux is still linearly proportionally to the pressure gradient, with a coefficient modified by the constant value ϕ/τ compared with the expression in Bretherton's paper (Eq. (7) in Ref. (Bretherton, 1961)). The rest of the derivation then follows Bretherton's arguments: (1) the driving pressure is given by the Laplace pressure: $p = \gamma\frac{d^2y}{dx^2}$; (2) use continuity constraint and assume steady state; (3) match the flat film region with the spherical region. Finally, we arrive at the modified Bretherton law:

$$h_{\text{film}} = \frac{b+B}{2} 1.34 \left(\frac{\tau}{\phi}\text{Ca}\right)^{\frac{3}{2}}.$$

It indicates that the presence of a surface rough does not change Bretherton's scaling but modifies the prefactor, in agreement with the arguments in Ref. (Keiser *et al.*, 2019). By setting $h_{\text{film}} = b$, we would arrive at the equation in the manuscript: $\text{Ca}_{\text{c,Tf}} = \frac{\phi}{\tau}\left[\frac{b}{0.67(b+B)}\right]^{3/2}$.

4.6.7 Wetting transition and film dewetting on the smooth plate

A thin film of defending fluid is deposited on the top smooth plate in our microfluidic setup when the flow rate is above a wetting transition threshold. The presence of the bottom rough surface makes the fluid-fluid interface asymmetric across the cell. The turning point, at which the local slope of the interface is $\pi/2$, shifts towards the top smooth plate (see Figs. 4-13A,B). The wetting transition for a thin film to appear on the smooth plate in our setup is delayed with respect to that in a confined system where the other side is also smooth. According to our experimental data (Movie S5, where the parameters are: $\text{Ca}_{\text{inj}} = 0.0145$, $b = 0.08$ mm and $B = 0.5$ mm), a liquid

film forms on the rough surface without any film left on the smooth surface. However, this Ca_{inj} is already larger than the predicted threshold for a smooth cell by Eq. (3) in the original manuscript.

The viscous dewetting of thin films on the top smooth plate follows classic dynamics (Redon *et al.*, 1991; De Gennes *et al.*, 2004): a dewetting rim forms next to the dewetting front and the dewetting front velocity is constant: $Ca_{dewet,smooth} = \frac{\theta_E^3}{6\ln}$, where ln is a dimensionless cut-off length that ranges from 10 to 20. It is at least 10 times faster than the thin-film dewetting on a rough surface. The latter one is estimated in Eq. 4.8 in the SI Appendix.

We note that the dewetting nucleation sites on smooth and rough plates are random and might appear in different locations. The zoomed-in videos (Movies S1, S2 and S3) capture only part of the cell. If the nucleation site on the smooth plate is closer to the observation window, we may then observe dewetting on the smooth side first. To clarify this point, we now include another video that records the whole field-of-view of the cell (see Movie S4, from which Fig. 1C in the manuscript is obtained). This video shows that dewetting occurs earlier on the rough plate at some locations (marked with blue rectangles) and on the smooth plate at other locations (marked with yellow rectangles).

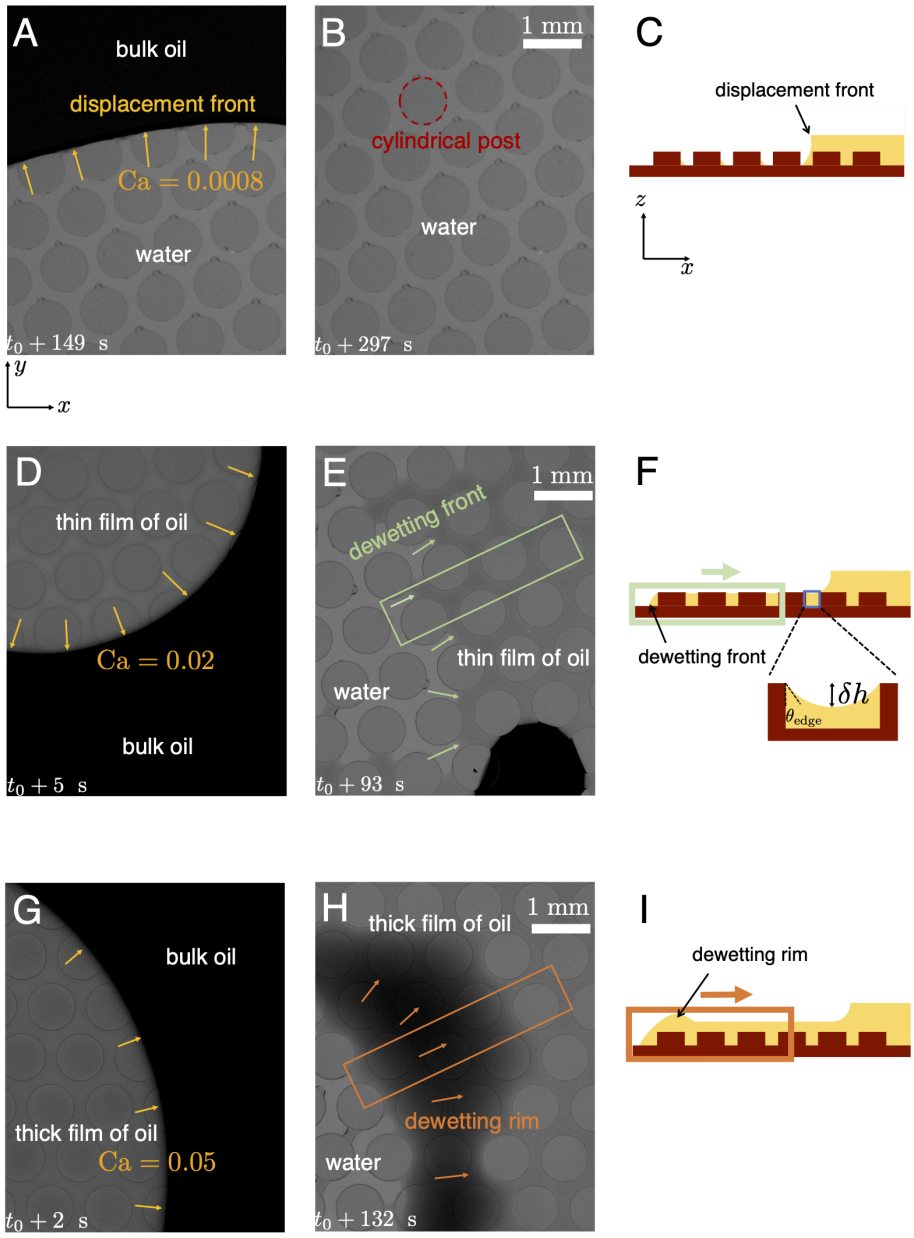

Figure 4-2: Experimental demonstration of different fluid-fluid displacement regimes on the same geometry, with $b = 0.08$ mm; $B = 0.5$ mm. (A)-(B) show complete displacement regime, here for local capillary number Ca ≈ 0.0008. They show the moments when water is displacing oil, and when oil has been completely displaced. (C) is the side-view schematic of complete displacement. (D)-(E) show the thin-film regime, here for local capillary number Ca ≈ 0.02. They show the moments when water is displacing oil leaving the thin film trapped behind the fluid-fluid front, and during dewetting of residual thin film. (F) is the side-view schematic of thin-film dewetting. (G)-(H) show the thick-film regime, here for local capillary number Ca ≈ 0.05. They show the moments when water is displacing oil with the thick film trapped behind the front, and during dewetting of the residual thick film. (I) is the side-view schematic of thick-film dewetting.

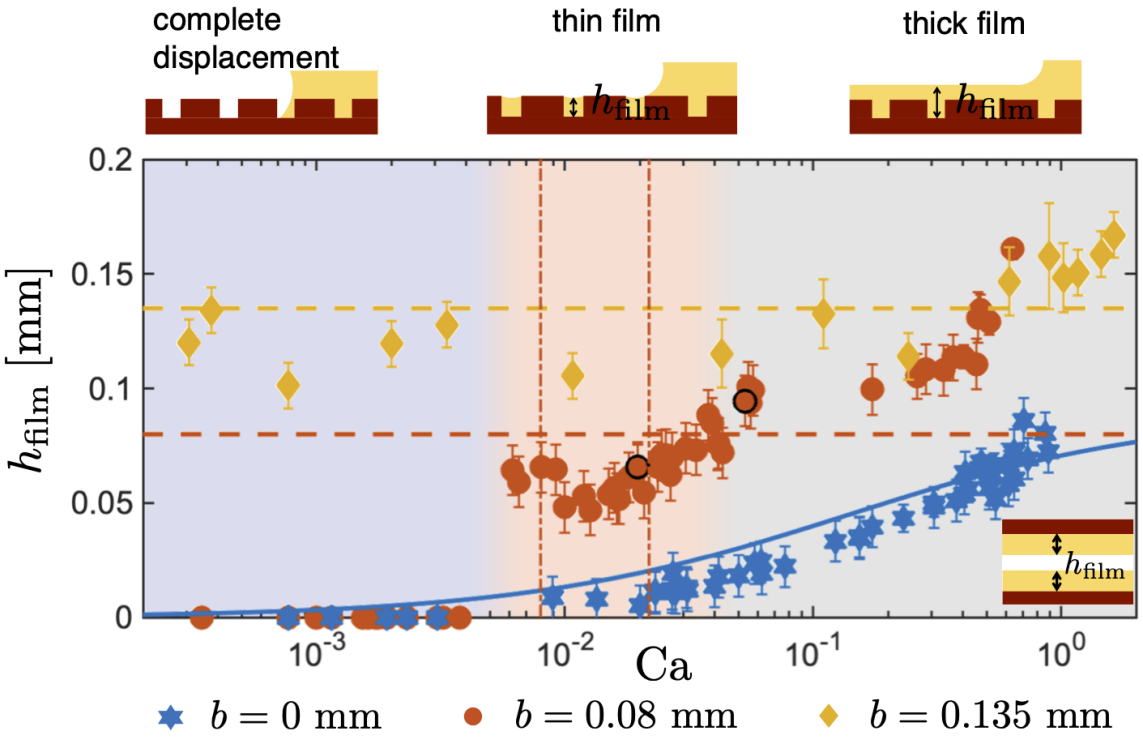

Figure 4-3: Experimentally measured local capillary number of the displacement front Ca vs. film thickness h_{film}, for gap height $B = 0.5$ mm. We show data for a smooth cell ($b = 0$, blue symbols) and two different post heights ($b = 0.08$ mm, red symbols; and $b = 0.135$ mm, yellow symbols). Circled red dots are the measurements for Fig. 4-2D (left) and Fig. 4-2G (right). The blue solid line is the extended Bretherton law (Klaseboer *et al.*, 2014): $\frac{h_{\mathrm{film}}}{B/2} = \frac{0.643(3\mathrm{Ca})^{2/3}}{1+2.79\times0.643\times(3\mathrm{Ca})^{2/3}}$. The vertical dashed lines, from left to right side, represent the $\mathrm{Ca}_{\mathrm{c,tf}}$ that sets the transition from complete displacement to thin film, and $\mathrm{Ca}_{\mathrm{c,Tf}}$ that sets the transition to thick film for the $b = 0.08$ mm case. The critical threshold for transitions for the smooth case $b = 0$ and the rough case $b = 0.135$ mm are shown in Fig. S9.

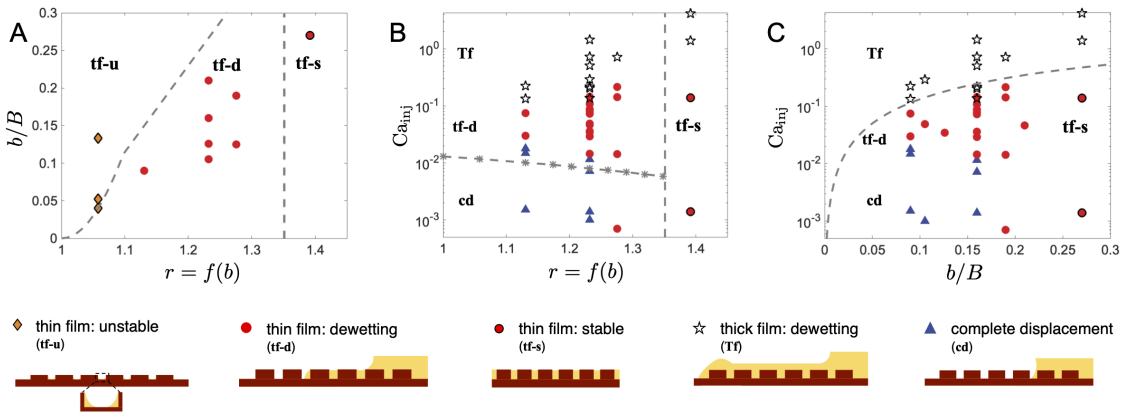

Figure 4-4: Phase diagrams of the different displacement regimes in the experiments. The diagrams demonstrate how the interplay between the degree of surface roughness (r), the vertical aspect ratio (b/B) and the injection capillary number ($\mathrm{Ca_{inj}}$) impact the wetting transition and fluid trapping. (A) Geometric criteria of the stability of thin films. The left dashed line represents $r_{c,1}$ (Eq. 4.1). When $r < r_{c,1}$, the thin film is unstable and cannot be form under any flow conditions. The vertical dashed line represents $r_{c,2}$ (Eq. 4.2), which is determined by the roughness factor only. When $r > r_{c,2}$, the thin film is stable and does not dewet. (B) Transition from complete displacement to thin film as $\mathrm{Ca_{inj}} > \mathrm{Ca_{inj,tf}} = \mathrm{Ca_{c,tf}}$ (Eq. 4.3). To the right of the vertical dashed line ($r = r_{c,2}$), the transition occurs at $\mathrm{Ca_{inj}} \to 0$. (C) Transition from thin film to thick film as $\mathrm{Ca_{inj}} > \mathrm{Ca_{inj,Tf}} = \frac{L}{4w_{\mathrm{inj}}}\mathrm{Ca_{c,Tf}}$ (Eq. 4.4).

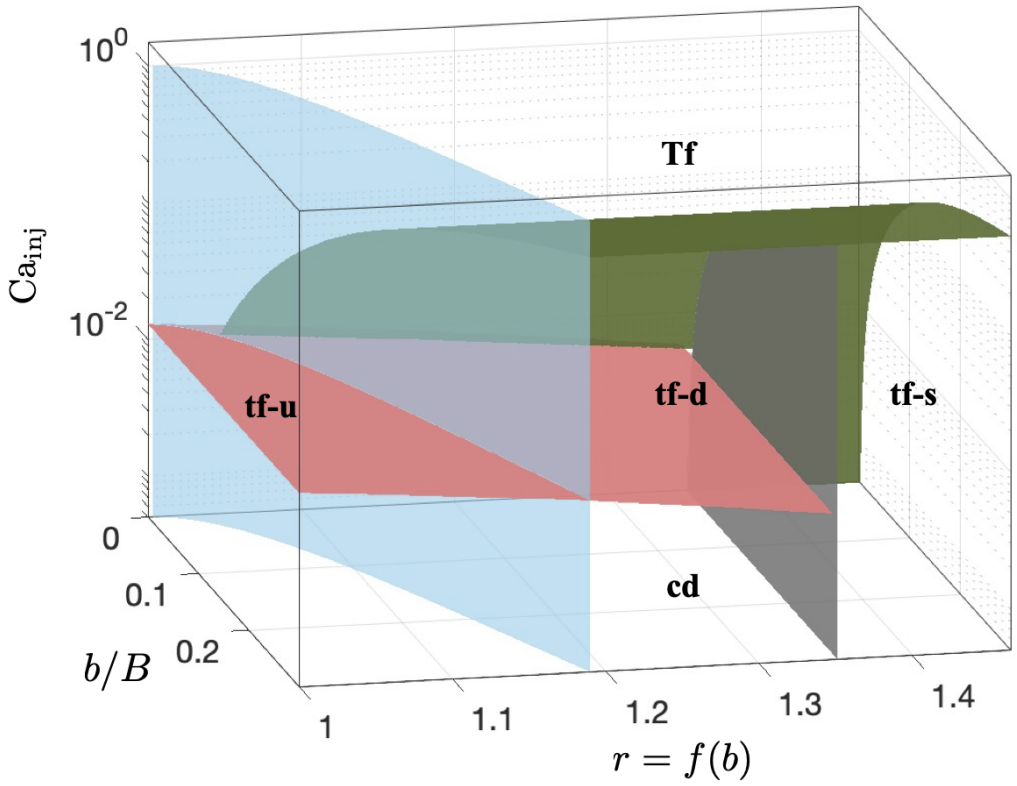

Figure 4-5: Phase diagram of the different drainage regimes in a rough microfluidic cell. Shown are the transitions among the five regimes (cd: complete displacement; tf-u: thin-film unstable; tf-d: thin-film dewetting; tf-s: thin-film stable; Tf: thick film) in the 3-dimensional parameter space that define geometry (b/B), roughness (r) and injection capillary number ($\mathrm{Ca_{inj}}$). The data points in Fig. 4 are included in the 3D phase diagram (see Fig. S10 in the SI Appendix).

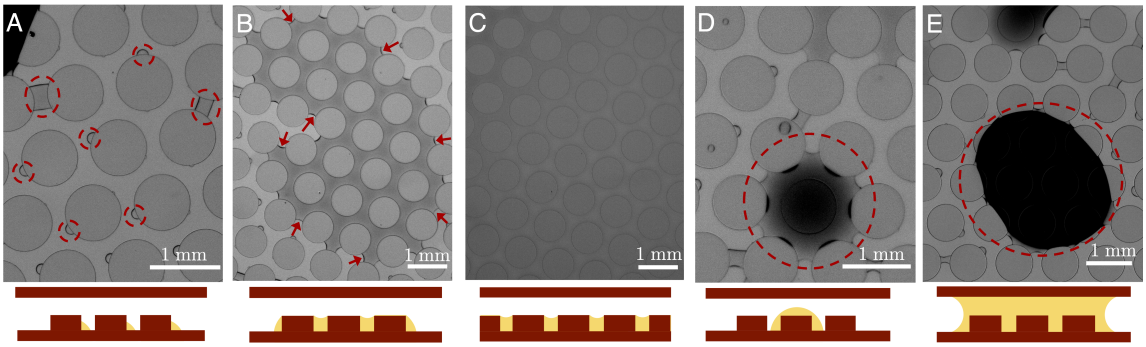

Figure 4-6: Late-time morphologies of undisplaced fluid and corresponding side-view schematics. They are observed in the thin-film dewetting regime (A-B), thin-film stable regime (C) and thick-film regime (D-E), respectively. (A) Residual micro-droplets attached to the corner of the post and throat-bridges connecting the neighboring posts. Experiment parameters for the image: $b = 0.08$ mm; $B = 0.5$ mm; $\mathrm{Ca}_{\mathrm{inj}} = 0.11$. (B) Residual lubrication film where the undisplaced oil fills a patch of pores without covering the top of the posts. Experiment parameters: $b = 0.08$ mm; $B = 0.5$ mm; $\mathrm{Ca}_{\mathrm{inj}} = 0.16$. (C) Residual lubrication film filling the pores of the whole cell. It forms when the thin film is energetically stable and does not dewet. Experiment parameters: $b = 0.08$ mm; $B = 0.5$ mm; $\mathrm{Ca}_{\mathrm{inj}} = 0.28$. (D) Residual liquid cap that covers an entire post. Experiment parameters: $b = 0.08$ mm; $B = 0.5$ mm; $\mathrm{Ca}_{\mathrm{inj}} = 0.28$. (E) Residual liquid bridge that channelizes the top and bottom surfaces resulting in blockage of flow path. Experiment parameters: $b = 0.135$ mm; $B = 0.5$ mm; $\mathrm{Ca}_{\mathrm{inj}} = 0.14$.

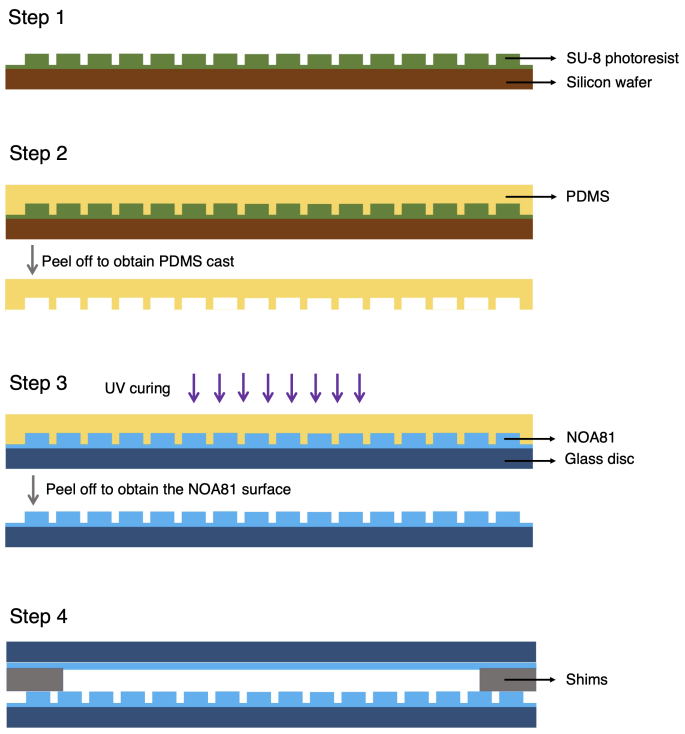

Figure 4-7: Fabrication process of the Hele-Shaw cells used in our experiments. Modified from Ref. (Zhao *et al.*, 2016).

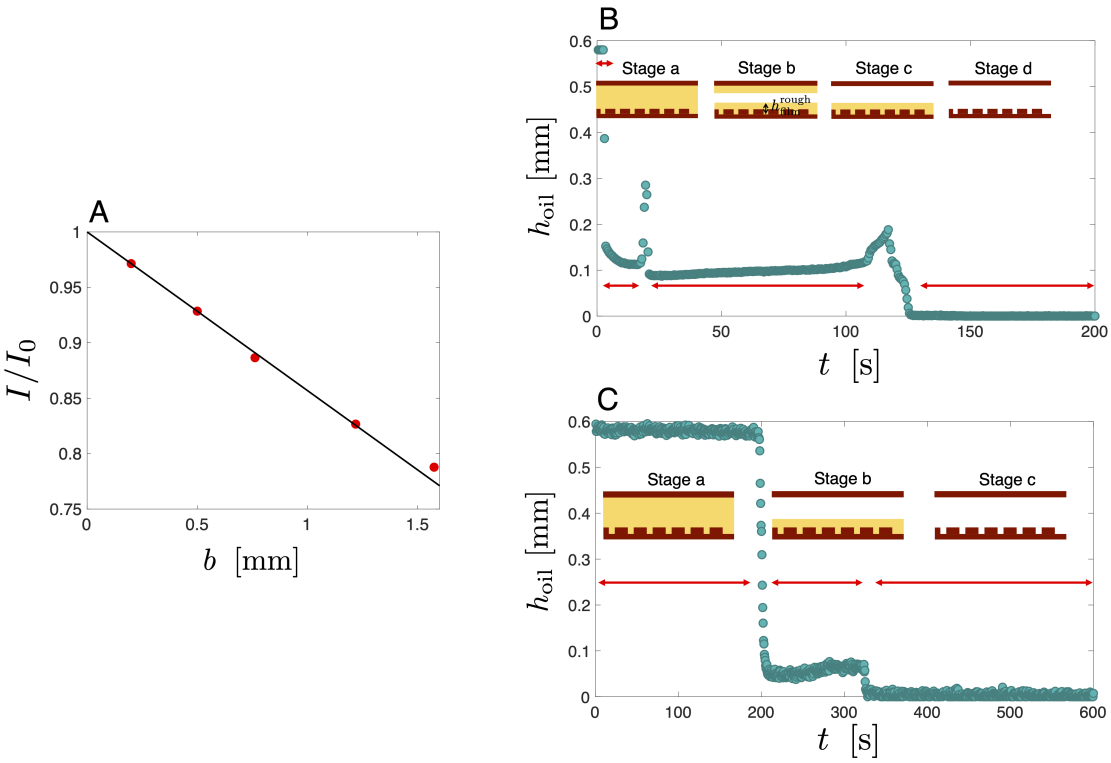

Figure 4-8: Quantification of the oil film thickness. (A) Transmitted light measured at different gap thickness b (red circles) and straight-line fit, valid for low b values (black solid line). Examples of the pore-averaged oil thickness h_{oil} as a function of time and the fluid configurations at specific periods, where films are simultaneously deposited on the rough and smooth surfaces (B) and films are only deposited on the rough surface (C).

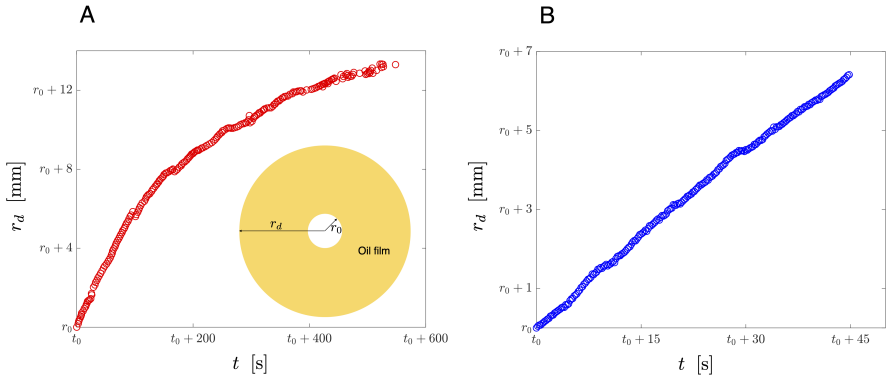

Figure 4-9: Examples of equivalent dewetting front radius r_d evolving with time t for thin-film droplets (A) and thick-film droplets (B).

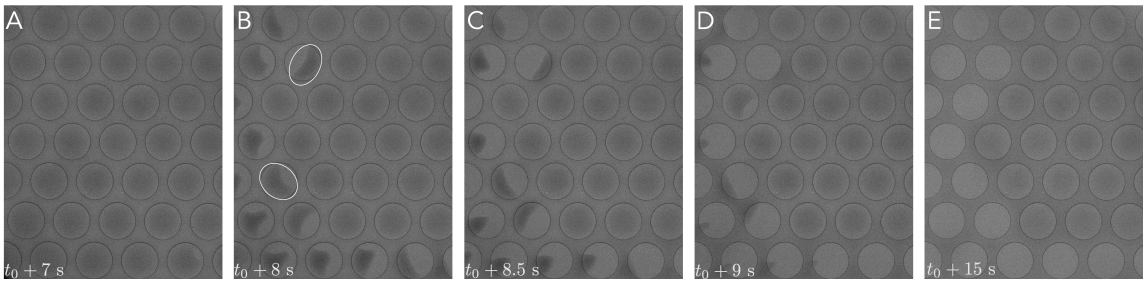

Figure 4-10: Sequence of images from the same experiment as Fig. 2G-H in the manuscript, showing that the oil in the entrained thick film drains from the top of the posts to the throats between posts.

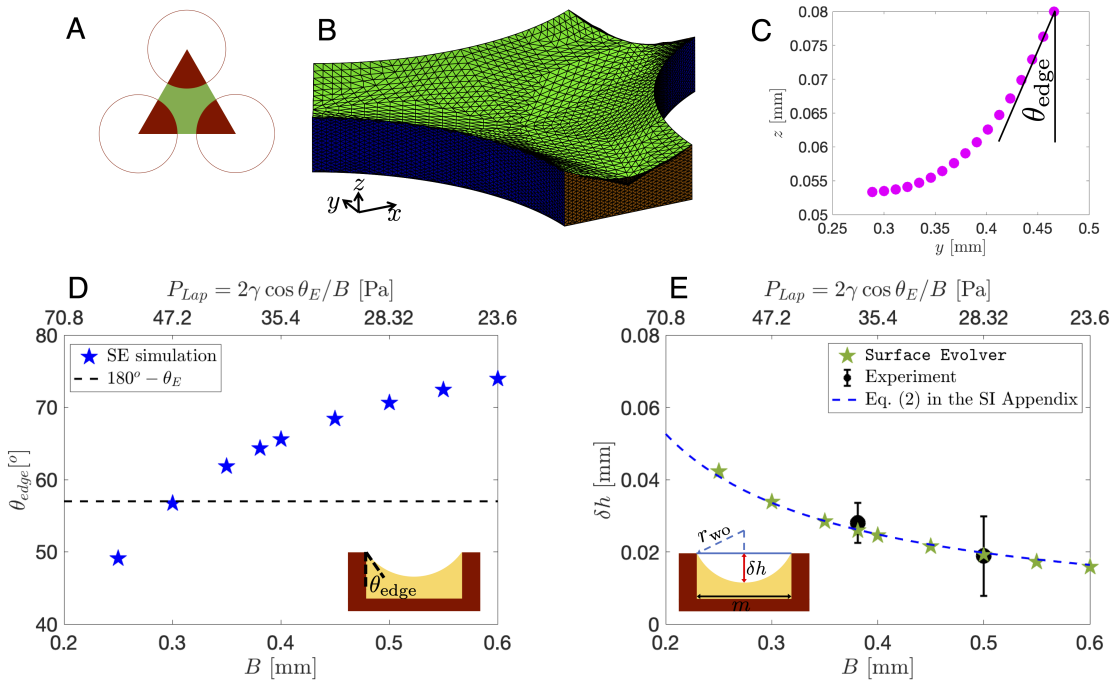

Figure 4-11: 3D configuration of thin film in one triangular cell and the calculation of penetration length δh and local angle at the edge θ_{edge}. (A) Top view of the geometry setup in `Surface Evolver`. (B) Simulated shape of thin film in 3D, where $b = 0.08$ mm and $P_{\text{Lap}} = 28.32$ Pa, corresponding to $B = 0.5$ mm. Blue color shows the contacting area between post and oil. Brown color shows the symmetry plane of oil phase. Green color shows the curved water-oil interface. (C) The measurement of the angle at which the interface meets the post's edge. (D) `Surface Evolver` simulated θ_{edge} as a function of B. The top axis shows the Laplace pressure related to B. (E) δh as a function of B. The least-squares fitted parameter $m = 0.379$ mm.

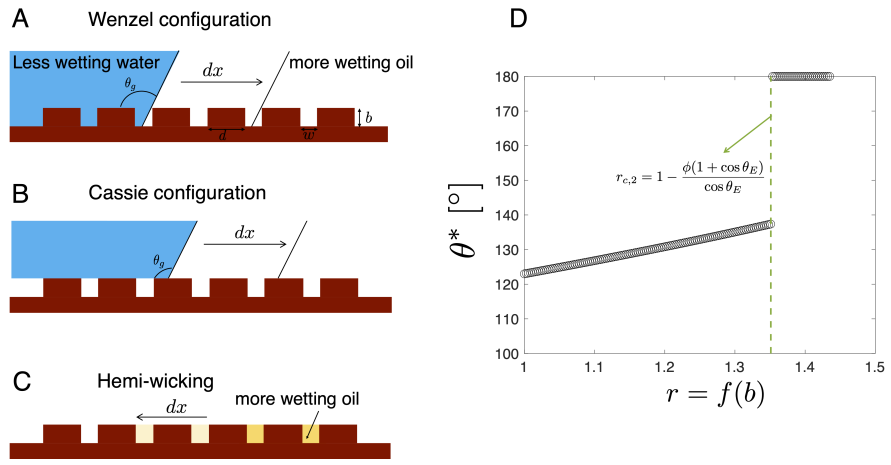

Figure 4-12: (A) - (C) Sketch of Wenzel state, Cassie state and hemi-wicking, respectively. They are adopted from Ref. (Quéré, 2008). (D) Apparent contact angle for the invading phase under different degree of roughness $r = 1 + \frac{4(1-\phi)b}{d}$.

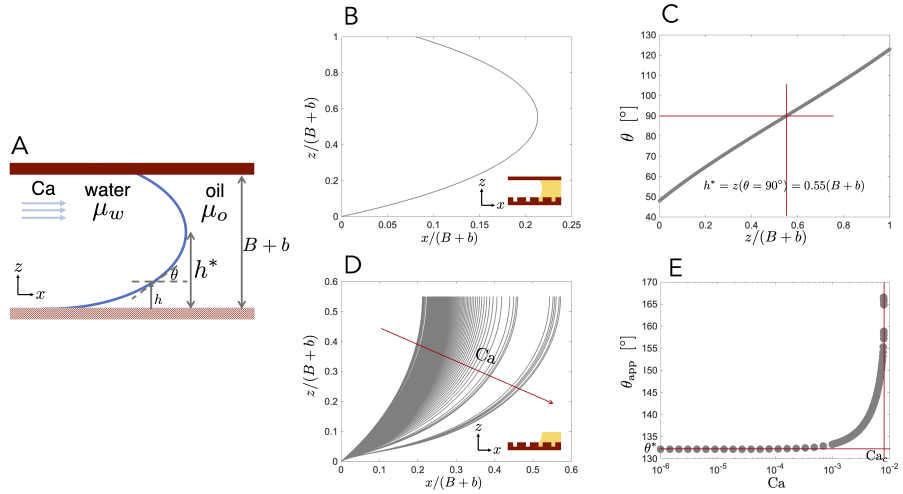

Figure 4-13: (A) Schematic of the interface shape across the cell. The bottom rough surface intersects the fluid interface at a slope of static apparent contact angle θ^*. While the top smooth surface intersects the fluid interface at equilibrium contact angle θ_E. At $h = h^*$, the local interface slope $\theta = \pi/2$. Solution to the meniscus shape for the case $b = 0.08$ mm; $B = 0.5$ mm: (B) Meniscus shape in the entire channel at equilibrium; (C) Relation between slope θ and height z for the interface shown in (A); (D) Computed meniscus shape as Ca increases; (E) Apparent contact angle increases with Ca, shown here for the same parameters in (C).

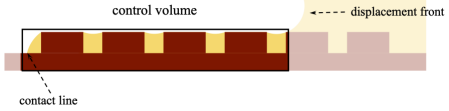

Figure 4-14: Sketch of control volume in analyzing thin film dewetting velocity.

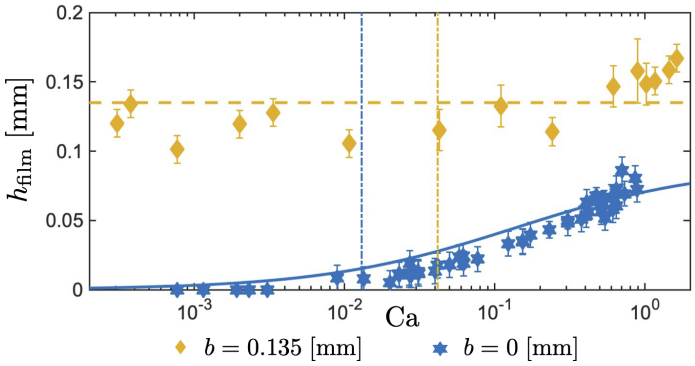

Figure 4-15: Critical threshold for the transitions between displacement regimes. The blue dashed line indicates the transition from complete displacement to thin film ($\mathrm{Ca}_{\mathrm{c,tf}}$) for the $b = 0$ case. The yellow dashed line indicates the transition from thin film to thick film ($\mathrm{Ca}_{\mathrm{c,Tf}}$) for the $b = 0.135$ mm case.

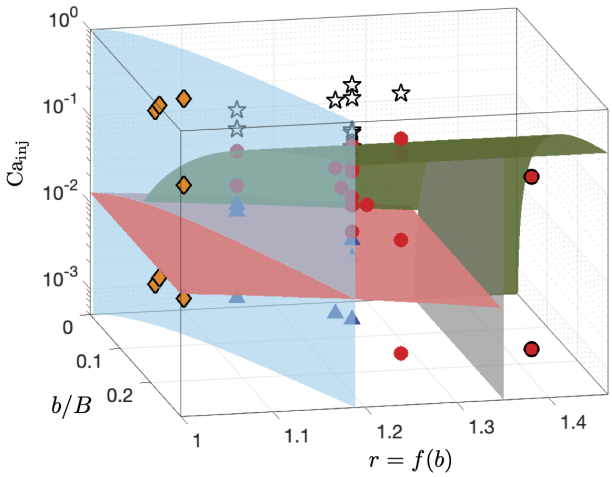

Figure 4-16: Phase diagram of the different drainage regimes in a rough microfluidic cell. The data points are same with those in Fig. 4 of manuscript.

Table 4.1: Experimental parameters and the dimensionless numbers used in Fig. 4

	Experimental parameters			Dimensionless numbers *		
	injection rate Q [ml/hr]	post height b [mm]	gap thickness B [mm]	$\mathrm{Ca}_{\mathrm{inj}}$	b/B	r
thin film unstable	0.5	0.02	0.15	2.4×10^{-3}	0.13	1.058
	10	0.02	0.15	4.9×10^{-2}	0.13	1.058
	100	0.02	0.15	4.9×10^{-1}	0.13	1.058
	1	0.02	0.381	2×10^{-3}	0.053	1.058
	100	0.02	0.381	2×10^{-1}	0.053	1.058
	1	0.02	0.5	1.5×10^{-3}	0.04	1.058
	100	0.02	0.5	1.5×10^{-1}	0.04	1.058
thin film dewetting	10	0.08	0.5	1.45×10^{-2}	0.16	1.232
	20	0.08	0.5	2.9×10^{-2}	0.16	1.232
	25	0.08	0.5	3.62×10^{-2}	0.16	1.232
	50	0.08	0.5	7.25×10^{-2}	0.16	1.232
	55	0.08	0.5	7.97×10^{-2}	0.16	1.232
	60	0.08	0.5	8.7×10^{-2}	0.16	1.232
	75	0.08	0.5	1.09×10^{-2}	0.16	1.232
	100	0.08	0.5	1.45×10^{-1}	0.16	1.232
	0.5	0.095	0.5	7×10^{-4}	0.19	1.276
	10	0.095	0.5	1.43×10^{-2}	0.19	1.276
	100	0.095	0.5	1.43×10^{-1}	0.19	1.276
	150	0.095	0.5	2.15×10^{-1}	0.19	1.276
	50	0.08	0.76	4.87×10^{-2}	0.105	1.232
	20	0.045	0.5	2.98×10^{-2}	0.08	1.131
	50	0.045	0.5	7.45×10^{-2}	0.08	1.131
	30	0.08	0.635	3.47×10^{-2}	0.126	1.232
	25	0.08	0.381	4.66×10^{-2}	0.21	1.232
thin film stable	1	0.135	0.5	1.4×10^{-3}	0.27	1.392
	100	0.135	0.5	1.39×10^{-1}	0.27	1.392
thick film dewetting	95	0.08	0.5	1.38×10^{-1}	0.16	1.232
	140	0.08	0.5	2.03×10^{-1}	0.16	1.232
	150	0.08	0.5	2.17×10^{-1}	0.16	1.232
	350	0.08	0.5	5.07×10^{-1}	0.16	1.232
	500	0.08	0.5	7.25×10^{-1}	0.16	1.232
	1000	0.08	0.5	1.45	0.16	1.232
	500	0.095	0.5	7.2×10^{-1}	0.19	1.276
	300	0.08	0.76	3×10^{-1}	0.105	1.232
	90	0.045	0.5	1.34×10^{-1}	0.08	1.131
	150	0.045	0.5	3×10^{-1}	0.08	1.131
	1000	0.135	0.5	1.39	0.27	1.392
	3000	0.135	0.5	4.2	0.27	1.392
complete displacement	1	0.08	0.5	1.5×10^{-3}	0.16	1.232
	5	0.08	0.5	7.2×10^{-3}	0.16	1.232
	8	0.08	0.5	1.16×10^{-2}	0.16	1.232
	1	0.045	0.5	1.5×10^{-3}	0.08	1.131
	10	0.045	0.5	1.5×10^{-2}	0.08	1.131
	12	0.045	0.5	1.8×10^{-2}	0.08	1.131
	1	0.08	0.76	1×10^{-3}	0.105	1.232

Chapter 5

Forced imbibition in a microfluidic fracture

5.1 Introduction

Immiscible fluid–fluid displacement in geometric confinement occurs in many natural and engineering processes, including water infiltration into soil (Hill & Parlange, 1972; Cueto-Felgueroso & Juanes, 2008), enhanced oil recovery (Orr Jr & Taber, 1984), fuel cell water management (Yang *et al.*, 2004), and microfluidics (Stone *et al.*, 2004).

The vast majority of the research on fluid-fluid displacement has focused on the drainage regime where the invading fluid is less wetting to the solid surface than the defending fluid, and we now have a fairly good understanding of the patterns forming on both macroscopic and microscopic scales. The fluid invasion pattern on the macroscopic scale has been shown to exhibit three regimes ranging from viscous fingering, capillary fingering to compact displacement, depending on the balance of viscous and capillary forces (Saffman & Taylor, 1958; Bretherton, 1961; Chen & Wilkinson, 1985; Lenormand *et al.*, 1988). While on the scale of a single pore, a recent study has demonstrated a rate-dependent dynamics with complete displacement at low displacement rates and incomplete displacement at sufficiently high displacement rates, due to the presence of moving contact lines (Zhao *et al.*, 2018). The transition between these two regimes is accompanied by the formation of thin films of the defending liquid

on the solid surface, which later dewet from the substrate (Zhao *et al.*, 2018). The geometrical confinement finally leads to the interface pinch-off and the formation of disconnected bubbles and drops (Zhao *et al.*, 2018; Pahlavan *et al.*, 2019). Later, (Qiu *et al.*, 2023) further extended the study of drainage to a rough confinement and show that the roughness induces two types of liquid films entrained on the solid surfaces: the classical Bretherton "thick film", and a new type of "thin film" that is confined within the roughness (Qiu *et al.*, 2023). Each type is characterized by distinct stability criteria and dewetting dynamics, leading to distinct late-time morphologies of the undisplaced (trapped) fluid (Qiu *et al.*, 2023).

In contrast with the robust observations in the drainage regime, experiments on imbibition, where the invading fluid is more wetting to the solid surface than the defending fluid, has gained less attention. Among them, the experimental observations are mainly for viscously favorable displacement, that is the displacement of more wetting and more viscous fluid to the less viscous and less wetting fluid, in the context from spontaneous imbibition (Washburn, 1921; Delannoy *et al.*, 2019; Ruiz-Gutiérrez *et al.*, 2022) and constant-rate imbibition (Hoffman, 1975; Fermigier & Jenffer, 1991) in a smooth capillary tube, to the roughening statistics of the imbibition front in a disordered medium (He *et al.*, 1992; Dubé *et al.*, 1999; Soriano *et al.*, 2002; Geromichalos *et al.*, 2002; Soriano *et al.*, 2005).

Only untill recently the viscously unfavorable displacement, where the invading phase is more wetting and less viscous than then defending fluid, has been studied. Ref. (Levaché & Bartolo, 2014) conducted experiments in a smooth Hele-Shaw cell where the plates are coated with a layer of NOA81 polymer material. They show that, above a critical flow rate, the fluid-fluid interface destablizes and the wetting fluid preferentially advances along the solid walls. This rate-dependent transition of leading film formation is completely different from the above-mentioned observations in drainage regime by (Zhao *et al.*, 2018). Later, studies by (Zhao *et al.*, 2016) and (Odier *et al.*, 2017) investigated the viscously unfavorable imbibition in microfluidic porous media, where arrays of posts interconnecting the top and bottom plates of smooth Hele-Shaw cells. They reported a similar phenomena where wetting liquid

forms a leading film and propagates throughout the lattice (Zhao *et al.*, 2016; Odier *et al.*, 2017), which significantly changes the characteristics of pattern formation in porous media (Zhao *et al.*, 2016).

Most real surfaces are rough. However, the interplay between wetting and surface roughness, and its consequences on the macroscopic imbibition patterns remain unexplored. In this work, we investigate the influence of roughness on the displacement of more wetting and less viscous fluid into another less wetting and more viscous fluid (viscously-unfavorable strong imbibition) in a microfluidic device. This microfluidic consists of a flat surface on one plate and a precisely controlled pattern on the other plate, as an analogue for a rough fracture.

Our main results are a visual phase diagram of the displacement pattern as a function of capillary number and the degree of surface roughness. At weak roughness, the fluid invasion pattern transitions to fractal front as capillary number increases, including tip-splitting fingering and then dendritic fingering. At strong roughness, we observe a reversed trend of pattern formation: increasing capillary number leads to compact invasion front. We show that the remarkable transition is caused by corner flow, which allows the wetting fluid to spontaneously coats the perimeters of posts above a critical post height. We further show that, the spontaneously coating is dominated by the continuous thin-film formation above a critical Ca. Further increasing Ca to a second critical threshold, the wetting fluid invades not only the roughness layer but also the gap layer due to the competition between capillary force and viscous friction within the post pattern. We then theoretically explain the crossovers among the observed regimes. Our results demonstrate the powerful control of the interplay between roughness and wetting on fluid-fluid displacement in rough confinements that may influence the long-term mixing and reactivity in natural fractured media.

5.2 Experimental setup

We conduct our experiments in radial Hele-Shaw cells (Fig. 5-1A), consisting of two parallel circular plates, separated by spacers of thickness B. We make one plate's

surface rough by patterning it with a six-fold symmetric lattice of cylindrical posts of height b. The spatial distribution of the surface roughness is fixed by the pore throat $w = 0.2$ mm and post diameter $d = 0.8$ mm. The injection port is at the center of the rough plate and is surrounded by a circular region of diameter $w_{\text{inj}} = 4.4$ mm without posts (Fig. 5-1B). We fabricate the rough plate and smooth plate of the flow cells with a photocurable polymer (NOA81, Norland Optical Adhesives). By exposing the NOA81 surface to high-energy UV radiation for 30 minutes, we find the static contact angle of water immersed in silicone oil is $\theta_E = 10 \pm 5^\circ$ (Zhao *et al.*, 2016). The fabrication processes of our microfluidic cells can be found in our previous work in ref. (Qiu *et al.*, 2023).

In each experiment, the cell is first saturated with silicone oil with viscosity $\mu_o =$ 500 mPa·s. Then, deionized water ($\mu_w = 0.99$ mPa) is injected into the cell at a constant injection rate Q. We characterize the displacement dynamics of each experiment using the injection capillary number $\text{Ca} = \frac{v_{\text{inj}}\mu_o}{\gamma}$, where $v_{\text{inj}} = \frac{Q}{\pi w_{\text{inj}}(B+b\phi)}$ is defined at the entrance of the post pattern and $\gamma = 13$ mN/m is the interfacial tension between silicone oil and water. In this study, we mainly investigate the role of two variables: (1) the injection rate (Ca) and (2) the degree of the surface roughness (post height b). We use three representative values of gap thickness (B = 0.1 mm, 0.15 mm and 0.5 mm).

5.3 Results and discussion

We demonstrate the remarkable control of surface roughness on the forced imbibition patterns via an experimental phase diagram obtained under two values of post height b and three capillary numbers that span three order of magnitude, as is shown in Fig. 5-2. Due to the smaller viscosity of the invading fluid, the displacement front is subject to the viscous fingering instability (Saffman & Taylor, 1958; Paterson, 1981; Homsy, 1987), which may exhibit different morphology depending on the cell anisotropy and flow rate (Godbey *et al.*, 1985). In terms of the two-dimensional pattern formation, we observe that fractal dimension of the displacement front decreases as capillary

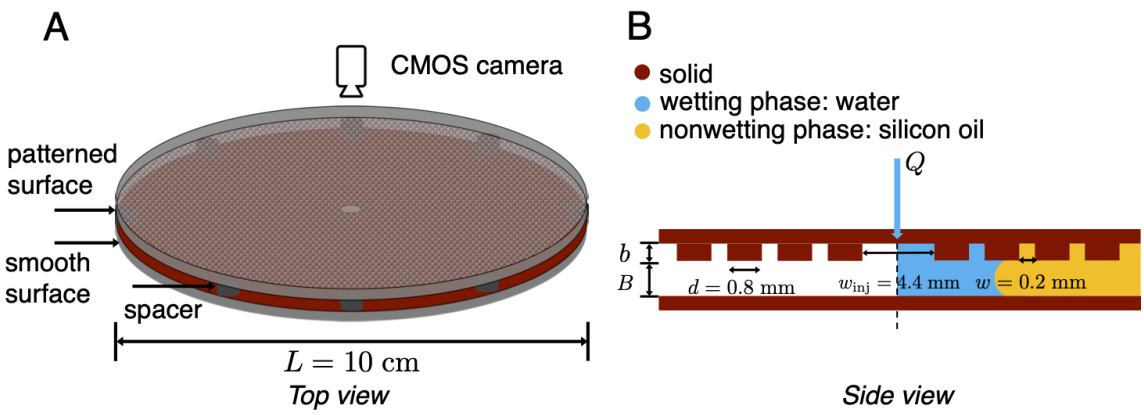

Figure 5-1: We inject water into a rough Hele-Shaw cell filled with viscous silicone oil at constant injection rate Q. (A) Schematic figure of the experimental system. We take images of the experiment from above with a CMOS camera, measuring the gap-averaged oil saturation at high spatial and temporal resolution after calibration of the light intensity. (B) Cross-section of the rough Hele-Shaw cell. The rough plate is patterned with a six-fold symmetric lattice of cylindrical posts with post diameter $d = 0.8$ mm and pore throat $w = 0.2$ mm. The fluid is injected at the center of the cell, within a post-free circular region of diameter $w_{\text{inj}} = 4.4$ mm.

.

number increases for weak roughness (Fig. 5-2A1-3). However, this relation for strong roughness is reversed where the fractal dimension decreases with Ca (Fig. 5-2B1-3). We will show that the difference of 2D patterns is closely linked to the 3D nature of advancing meniscus in the pore scale.

To gain the physical insights of displacements in three-dimension, we color code the displacement pattern using the gap-averaged water saturation via light-intensity calibration. In Fig. 5-2, the saturation profile reveals three types of preferential paths across the cell gap: (1) *complete invasion*, marked by yellow, where invading fluid advances by fully filling across the whole channel including roughness layer and gap layer; (2) *thick-film invasion*, marked by orange, where the invading fluid fully covers the roughness layer but partially fills the gap layer; (3) *thin-film invasion*, marketed by red, where the invading fluid only advances between the posts on the roughness layer. Here we uncover and theoretically analyze the 2D and 3D behaviors in Fig. 5-2 following the order: (1) the influence of roughness on the displacement pattern at low Ca (A1 $\rightarrow$ B1); (2) the influence of capillary number on the displacement pattern at

weak roughness (A1 → A3); (3) the influence of capillary number on the displacement pattern at strong roughness (B1 → B3).

5.3.1 Complete invasion to thin-film invasion at low capillary numbers

At low capillary numbers, we observe a dramatic change in both the macroscopic displacement pattern and the pore-scale displacement mechanism as we increases the roughness degree. Specifically, the invading fluid advances across the whole channel and displacement front is relatively smooth for weak roughness (Fig. 5-2A1). While the invading phase advances by sequentially coating the neighboring posts in roughness layer, which leads to a more ramified front for strong roughness (Fig. 5-2B1).

Given the low displacement rates where the viscous forces are negligible, the flow is governed exclusively by the capillary force. In our flow cell, the post intersecting the top plate forms corners that provides capillary suction to drive the invading fluid advancing within the roughness layer (Fig. 5-3A). This is similar to *corner flow* phenomena in porous media flow (Zhao *et al.*, 2016; Primkulov *et al.*, 2018, 2021) and spontaneous imbibition in angular capillary tube (Weislogel & Lichter, 1998; Bico & Quéré, 2002). The amount of capillary suction depends on the roughness geometry.

To quantify this process, we compute the three-dimensional shape of water-oil meniscus in a corner (Fig. 5-3A), described by the differential equation (Primkulov *et al.*, 2018):

$$\frac{dz/dr}{r(1+(dz/dr)^2)^{1/2}} + \frac{d^2z/dr^2}{(1+(dz/dr)^2)^{3/2}} = \frac{P_{c,r}}{\gamma}, \tag{5.1}$$

where $P_{c,r}$ is the capillary pressure. We prescribe the boundary conditions on the top plate and on the side wall of the post based on two facts:

- Before the meniscus reaches the post edge ($z|_{r=d/2} > 0$), the contact angle on the side wall and top plate should always satisfy the static contact angle:

$$dz/dr|_{r=d/2} = \tan(\pi/2 - \theta_E), \quad dz/dr|_{r=d/2+w} = \tan\theta_E. \tag{5.2}$$

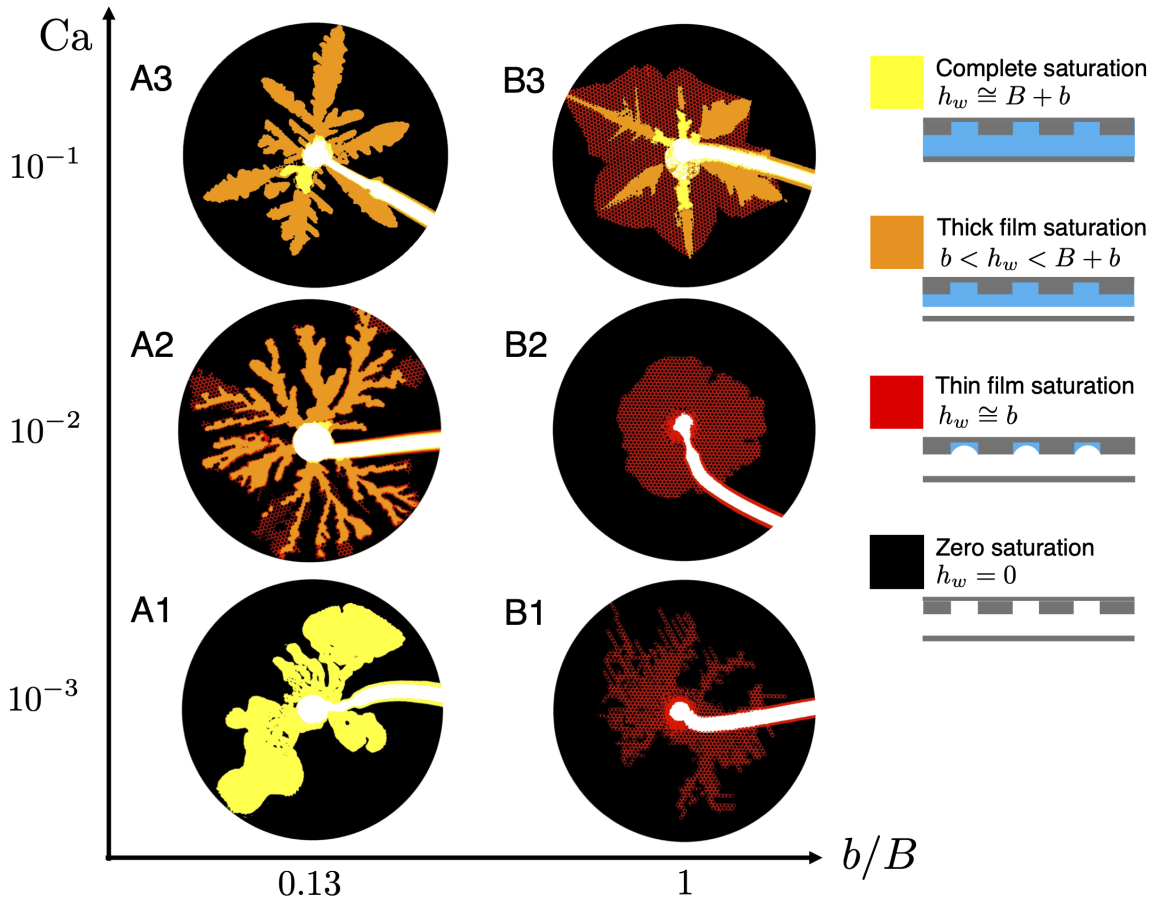

Figure 5-2: Forced imbibition patterns for different degrees of roughness (left to right: b = 0.02 mm, b = 0.15 mm) and capillary numbers. Here the gap thickness is fixed as $B = 0.15$ mm. These patterns are captured at the time when the invading fluid reaches the flow cell radius of 70 mm. The colormap shows the gap-averaged saturation of the invading phase: yellow indicates that water fully saturates across both roughness and gap layers, local thickness of which is $h_w \cong B+b$; orange indicates water fully saturates across the roughness layer but partially saturates across the gap layer, with $b < h_w < B + b$; red indicates that water saturates the roughness layer only, with $h_w \cong b$; black indicates the places that have not been displaced.

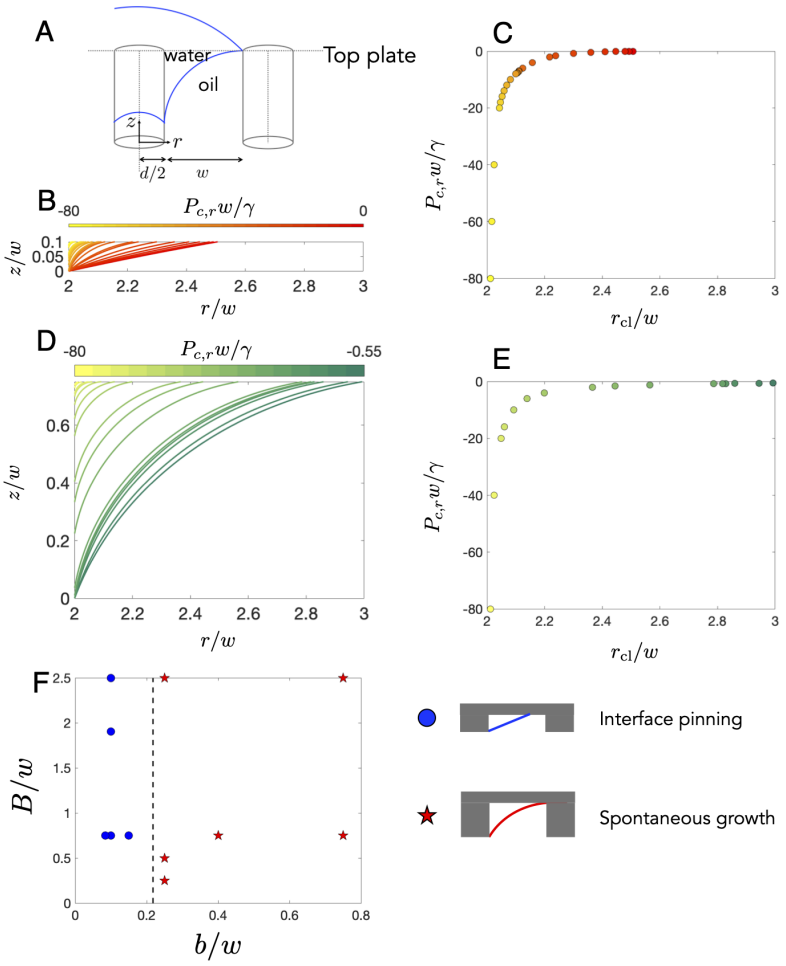

Figure 5-3: (A) Three-dimensional schematic of oil-water meniscus moving from the corner of one post (left) to that of the neighboring post (right). The origin of the axisymmetric coordinate used in Eq. 5.1 is at the center of left post. (B) Computed profiles for oil-water meniscus in the corner of a post with height $b = 0.02$ mm, with decreasing absolute values of capillary pressure $|P_{c,r}|$. These profiles demonstrate the spontaneous growth process from the left side. Before the meniscus reaches the next post, the driven capillary pressure becomes zero indicating the interface pinning. (C) The location of the contact line on the top plate r_{cl} vs. the imposed $P_{c,r}$. Same parameter as in (B). (D) Computed profiles for oil-water meniscus in the corner of a post with height $b = 0.15$ mm, with decreasing absolute values of capillary pressure $|P_{c,r}|$. These profiles demonstrate the spontaneous growth process can sustain until the meniscus reaches the next post, without pinning. (E) Same parameter as in (D). (F) Experimental phase diagram of spontaneous wicking (as is shown in Fig. 5-2B1) and interface pinning (as is shown in Fig. 5-2A1) observed at low capillary numbers. The dashed line is the theoretical prediction from Eq. 5.1

.

- If the meniscus reaches the edge ($z_{r=d/2} = 0$), the contact line is pinned but the contact angle is free to deviate from its static value. While the contact angle on the top plate remains unchanged. Thus the boundary conditions become:

$$z_{r=d/2} = 0, \quad dz/dr|_{r=d/2+w} = \tan\theta_E. \tag{5.3}$$

We numerically integrate Eq. 5.1 from $r = d/2$ using MATLAB `ODE45` and find the solutions with a shooting algorithm (see the details in Appendix 5.4.1). Note that the post diameter (d) and distance between post (w) are fixed in our experiments. Fig. 5-3B shows the solutions of water-oil meniscus profile for post height $b = 0.02$ mm. The growth of water-oil meniscus from the corner of a post (left in Fig. 5-3B) is accompanied by the decreasing of capillary pressure $|P_{c,r}|$. After the contact line on the side wall reaches the edge of post and gets pinned, the contact line on the top plate is still free to extend, which results in further decreasing of $|P_{c,r}|$. This process can be visualized by tracking the location of contact line on the top plate z_{cl} as a function of the driven capillary pressure, shown in Fig. 5-3C. In this case, $|P_{c,r}|$ becomes zero far before the meniscus reaches the neighboring post ($z_{\mathrm{cl}} < d/2 + w$). It indicates that spontaneous coating in the roughness layer cannot occur. While for a higher post $b = 0.15$ mm, the solutions in Fig. 5-3D and E show that capillary pressure is nonzero even when the contact line on the top plate has reached the neighboring post. It demonstrates the occurrence of spontaneous coating.

The macroscopic manifestation of spontaneous coating in the pore scale (Fig. 5-3D) is the formation of "chains" of coated posts, as is shown in Fig. 5-2B1. Such pattern exhibits high fractal dimension and lower displacement efficiency. With smaller post height (Fig. 5-3B), the coating cannot occur. In this case, as the invading fluid advances slowly, the two water-oil menisci around a pore body and the meniscus in the gap layer may come to coalesce. This is similar to the cooperative pore filling in porous media that usually occurs when the invading fluid is intermediately wetting (Cieplak & Robbins, 1990; Holtzman & Segre, 2015; Zhao *et al.*, 2016; Primkulov *et al.*, 2021). The coalescence promotes the full saturation of water across the whole

channel and also smoothens the displacement front, as is shown in Fig. 5-2A1. We thus determine the criterion that onsets the transition from complete invasion (Fig. 5-2A1) to thin-film, fractal-front invasion (Fig. 5-2B1) at low capillary numbers by setting $P_c = 0$ in Eq. 5.1 and using the boundary conditions in Eq. 5.3 (see the details in Appendix 5.4.1). The solution gives a critical post height $b^* = 0.043$ mm, above which the spontaneous coating occurs and thin-film fractal-front pattern emerges. It matches well with our experimental observations, as is shown in Fig. 5-3F.

5.3.2 Rate-dependent selection of fingering morphology for weak roughness

For weak roughness, we observe the transition to tip-splitting viscous fingering (Fig. 5-2A2) at intermediate capillary number, and then to the dendritic viscous fingering (Fig. 5-2A3) at high Ca. The tip-splitting instability occurs as the finger grows by repeated splitting on the tip which results in a highly branching pattern. This is a generic type of instability that has been extensively studied in the context of smooth Hele-Shaw cell, but without considering the wetting condition (Paterson, 1981; Ben-Jacob *et al.*, 1986). In our study where the invading fluid is more wetting, we observe a layer of thin film surrounding the fingering branches (Fig. 5-2A2). This phenomena is similar to observations by Ref. (Levaché & Bartolo, 2014) which studied the displacement process of more wetting water displaces more viscous oil but in a smooth and reclinear Hele-Shaw cell. They show that the invading phase preferentially advances along the solid wall as a leading film above a critical flow rate.

However, at sufficiently high Ca, the thin films disappear and the tip-splitting instability is dominated by the dendrite fingering with six-fold symmetric pattern that directly reflects the underlying symmetry of the roughness layer (Fig. 5-2A3). The 2D fingering pattern transition from tip-splitting to dendrite growth has been known to result from the anisotropy in the flow cells (Godbey *et al.*, 1985; Couder *et al.*, 1986; Sarkar & Jasnow, 1989; Almgren *et al.*, 1993; Yokoyama *et al.*, 1994; Zhang *et al.*, 2021). The anisotropy, which is the post pattern in our study, stablizes the ad-

vancing front and prevents it from splitting (Godbey *et al.*, 1985; Zhang *et al.*, 2021). The dendritic patterns have also been observed in systems including electrochemical transport (Grier *et al.*, 1986, 1987; Sawada *et al.*, 1986), solidification (Langer, 1980; Utter *et al.*, 2001) and non-Newtonian fluid flow (Buka *et al.*, 1986; Zhang *et al.*, 2023).

5.3.3 Rate-dependent transition of preferential invasion path for strong roughness

For strong roughness, the invading fluid keeps advancing along the roughness layer as a thin film when the Ca increases to a intermediate value (Fig. 5-2B2). However, the displacement pattern becomes compact instead of being ramified by the chains of coated pasts, as those observed in low Ca (Fig. 5-2B1). We rationalize this transition by comparing the local velocity of the displacement front v_{local} with the speed of spontaneous coating v_{coat}. When the front velocity is smaller than the spontaneous coating velocity $v_{\text{local}} < v_{\text{coat}}$, the interface dynamics is dominated by the formation of coating chains. While for $v_{\text{local}} > v_{\text{coat}}$, the invading fluid advances by filling the pore space in the roughness layer that leads to a radially stable front. Here the coating speed $v_{\text{coat}} = 0.5$ mm/s is measured on multiple locations from the experiment shown in Fig. 5-2B1. Since water displaces oil radially outward, the local front velocity is maximum near the injection center (v_{inj}) and decays away from it. For the thin-film fractal-front pattern in Fig. 5-2B1, we find $v_{\text{inj}} = 0.15$ mm/s smaller than the v_{coat}, which agrees with our argument. Besides, for the experiment in Fig. 5-2B2, we find at the incipient stage $v_{\text{inj}} = 3.11$ mm/s is larger than v_{coat} and thus thin-film compact-front invasion emerges. As the front advances to the cell radius around 40 mm, the local front velocity decays to $v_{\text{local}} = 0.2$ mm/s which triggers the formation of coated chains (see the time lapsed images in Fig. 5-5).

Further increasing to sufficiently high Ca (Fig. 5-2A3), the thin-film compact-front invasion continues to emerge since the local front velocity would be larger than the coating velocity through out the displacement. Remarkably, the invading phase

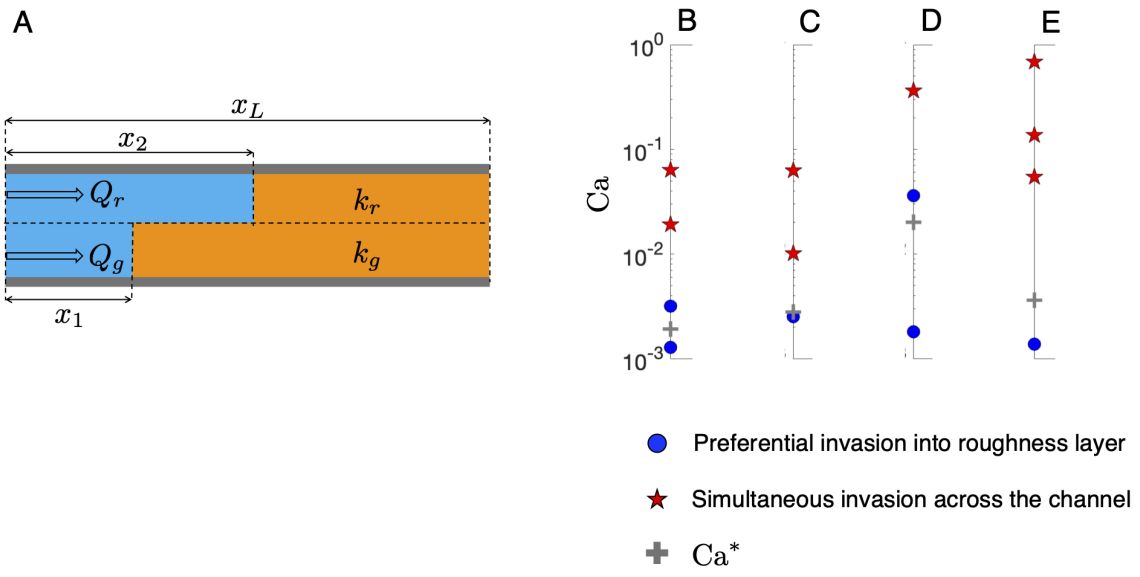

Figure 5-4: (A) Schematic of the *pore-doublet* model for imbibition in a microfluidic fracture with strong roughness. Experimental phase diagrams of preferential flow into roughness layer (as is shown in Fig. 5-2B2) and simultaneous invasion (as is shown in Fig. 5-2B3) for the parameters $b = 0.05$ mm, $B = 0.1$ mm (B); $b = 0.08$ mm, $B = 0.15$ mm (C); $b = 0.15$ mm, $B = 0.15$ mm (D); $b = 0.15$ mm, $B = 0.5$ mm (E). The red stars denotes the simultaneous invasion while blue dots denotes the preferential invasion to roughness layer. The gray markers indicate the theoretical prediction from Eq. 5.5.

simultaneously advances through the gap layer that increases the water saturation. Due to the high confinement $b/B = 1$ in Fig. 5-2A3, the water-oil interface in the gap layer exhibits the six-fold dendritic shape.

We rationalize the transition from preferential invasion into the roughness layer, as a thin film, to simultaneous invasion across the whole channel using a *pore-doublet* model of heterogeneous porous media (Lu *et al.*, 2020, 2021). We consider that the displacement in the roughness layer and gap layer is independent from each other (see the sketch in Fig. 5-4A). At low flow rate, the wetting phase prefers to imbibe into roughness layer because of the higher capillary pressure. While at high flow rate, the viscous force dominates and the wetting phase would prefer to invade the gap layer because of its higher permeability. Thus, whether the preferential flow in the roughness layer can sustain depends on the combination of capillary pressure, permeability, fluids' viscosity and flow rate. We analyze the pressure distribution in

each layer and each fluid using Darcy's law:

$$\frac{\partial P_{ij}}{\partial x} = -\frac{\mu_j}{k_i}\frac{Q_i}{2\pi x H_i}, \tag{5.4}$$

where x is the distance from the injection port, $i \in \{r, g\}$ denotes different layer and $j \in \{w, o\}$ denotes different fluid, P is the pressure, μ is the viscosity, k is the permeability and Q is the volumetric flow rate. The displacement in these two layers are coupled in two aspects: (1) the pressure in the inlet and outlet should be equal; (2) the total flow rate is fixed $Q = Q_r + Q_g$. See the detailed discription in Appendix 5.4.2.

To obtain the critical flow rate below which the roughness layer is the preferential flow path, we perform a linear stability analysis of the model equations at the initial stage of imbibition $x_0 = w_{\text{inj}}/2$ (see the definition of geometry in Fig. 5-1). We perturb the fluid-fluid interface in the rough layer by a small number $x_2 = x_1 + \epsilon x_0$ and determine the condition under which the perturbation grows or decays. See the detailed analysis in the Appendix 5.4.2. The results of linear stability analysis show that the preferential invasion into roughness layer occurs for $\text{Ca} < \text{Ca}^*$. Otherwise, we would observe the simultaneous invasion when $\text{Ca} > \text{Ca}^*$:

$$\text{Ca}^* = \frac{2(P_{c,r} - P_{c,g})}{\ln(X)\left(\frac{\phi}{k_r} - \frac{1}{k_g}\right) w_{\text{inj}}\gamma}, \tag{5.5}$$

where $X = L/w_{\text{inj}}$. The capillary pressure in the roughness layer $P_{c,r}$ is obtained by using the static oil-water meniscus shape shown in Fig. 5-3. To the first-order approximation, we take the capillary pressure in the gap layer as zero $P_{c,g} = 0$ since the gap layer is not always fully saturated due to the fact that our injection port is located in the top plate. We approximate the permeability in the gap layer as $k_g = B^2/3$ while in the roughness layer as $k_r = (\phi b^2)/(3\tau)$, where $\tau = 1.2$ is the tortuosity coefficient. This prediction matches well with our experiments conducted under different values of post height and gap thickness, as is shown in Fig. 5-4B-E.

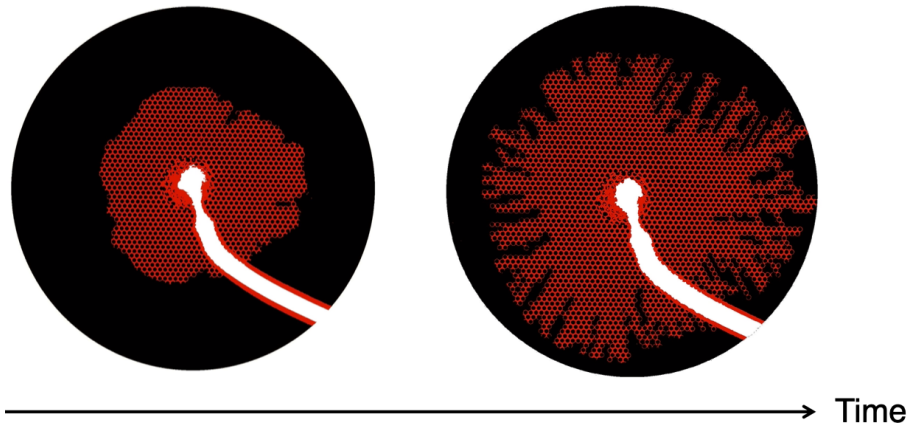

Figure 5-5: Sequence of images from the experiment shown in Fig. 5-2B2, showing the transition from thin-film compact-front pattern to thin-film fractal-front pattern.

5.4 Supplemental materials

5.4.1 Static water-oil meniscus shape in a corner: numerical schemes

5.4.2 Pore doublet model

Theoretical model

Here we build up the theoretical model to quantitatively understand the displacement dynamics in a microfluidic cell with strong roughness. We follow a similar derivation to that of the imbibition in a stratified porous media (Lu *et al.*, 2020, 2021).

For a constant-rate displacement, the law of mass conservation could be expressed as:

$$Q_g + Q_r = Q, \tag{5.6}$$

where Q is the imposed injection rate, Q_g is the flow rate in the gap layer:

$$Q_g = 2\pi H x_1 \frac{dx_1}{dt}, \tag{5.7}$$

and Q_r is the flow rate in the rougness layer:

$$Q_r = 2\pi h\phi x_2 \frac{dx_2}{dt} \tag{5.8}$$

Then we analyze the pressure distribution by integrating Eq. 5.4 from x_0 to x_L and including a term of capillary pressure drop. For the displacement in the gap layer, we arrive at:

$$P_0 = \frac{\mu_w}{2\pi H k_g}\int_{x_0}^{x_1}\frac{Q_g}{x}dx + \frac{\mu_o}{2\pi H k_g}\int_{x_1}^{x_L}\frac{Q_g}{x}dx - P_{c,g}. \tag{5.9}$$

Similarly, the pressure distribution in the roughness layer is expressed as:

$$P_0 = \frac{\mu_w}{2\pi h k_r}\int_{x_0}^{x_2}\frac{Q_r}{x}dx + \frac{\mu_o}{2\pi h k_r}\int_{x_2}^{x_L}\frac{Q_r}{x}dx - P_{c,r} \tag{5.10}$$

Given that the pressure in the inlet should be equal to each other, we subtract Eq. 5.10 from Eq. 5.9:

$$\begin{aligned} 0 =& \frac{\mu_w}{2\pi}\int_{x_0}^{x_1}\left(\frac{Q_g}{xHk_g} - \frac{Q_r}{xhk_r}\right)dx \\ &+ \frac{\mu_w}{2\pi}\int_{x_1}^{x_2}\left(\frac{\mu_o}{\mu_w}\frac{Q_g}{xHk_g} - \frac{Q_r}{xhk_r}\right)dx \\ &+ \frac{\mu_o}{2\pi}\int_{x_2}^{x_L}\left(\frac{Q_g}{xHk_g} - \frac{Q_r}{xhk_r}\right)dx \\ &+ (P_{c,r} - P_{c,g}). \end{aligned} \tag{5.11}$$

The displacement dynamics is described by coupling Eq. 5.6, 5.7, 5.8 and 5.11.

Linear stability analysis

To predict the flow rate below which the roughness layer is the preferential path, we perform linear stability analysis to the above equations (Lu *et al.*, 2020, 2021). We first linearize the equations given a small perturbation:

$$x_2 = x_1 + \epsilon x_0, \tag{5.12}$$

where ϵ is the perturbation amplitude and $x_0 = w_{\text{inj}}/2$ is the initial location of the interfaces (see the definition in Fig. 5-1B). Combine Eq. 5.6, 5.7, 5.8 and 5.12, we arrive at:

$$2\pi H x_1 \frac{dx_1}{dt} + 2\pi h\phi x_1 \frac{dx_1}{dt} + 2\pi h\phi x_1 x_0 \frac{d\epsilon}{dt} + 2\pi h\phi x_0 \epsilon \frac{dx_1}{dt} + 2\pi h\phi x_0^2 \epsilon \frac{d\epsilon}{dt} = Q. \quad (5.13)$$

Note that we analyze the dynamics at the initial stage $x_1 = x_0$ only. Neglecting the higher order $0(\epsilon^2)$ terms, we then obtain linearized equations for mass conservation:

$$Q_g = 2\pi H x_0 \frac{dx_1}{dt}, \quad (5.14)$$

$$Q_r = 2\pi h\phi x_0 (1+\epsilon) \frac{dx_2}{dt}, \quad (5.15)$$

where

$$\frac{dx_1}{dt} = \frac{Q - 2\pi h\phi x_0^2 \frac{d\epsilon}{dt}}{2\pi(H + h\phi)x_0 + 2\pi h\phi x_0^2 \epsilon}, \quad (5.16)$$

and

$$\frac{dx_2}{dt} = \frac{Q + 2\pi H x_0^2 \frac{d\epsilon}{dt}}{2\pi(H + h\phi)x_0 + 2\pi h\phi x_0 \epsilon}. \quad (5.17)$$

Substituting these equations back to Eq. 5.11, we arrive at the equation:

$$\begin{aligned} 0 = & \frac{\mu_o \ln(L) Q}{2\pi(H + h\phi) + 2\pi h\phi\epsilon} \frac{1}{k_g} \\ & - \frac{(\mu_w \ln(1+\epsilon) + \mu_o \ln(L/(1+\epsilon)))}{2\pi(H + h\phi) + 2\pi h\phi\epsilon} \frac{\phi(1+\epsilon)}{k_r} Q \\ & - \frac{\mu_o x_0^2 \ln(L)}{(H + h\phi) + h\phi\epsilon} \frac{h\phi}{k_g} \frac{d\epsilon}{dt} \\ & - \frac{(\mu_w \ln(1+\epsilon) + \mu_o \ln(L/(1+\epsilon)))}{(H + h\phi) + h\phi\epsilon} \frac{\phi(1+\epsilon) H x_0^2}{k_r} \frac{d\epsilon}{dt} \\ & + (P_{c,r} - P_{c,g}), \end{aligned} \quad (5.18)$$

where $L = x_L/x_0$. To the leading order ($\epsilon \to 0$), the equation is reduced to:

$$\frac{\mu_o \ln(L) \phi x_0^2}{(H + h\phi)} \left(\frac{h}{k_g} + \frac{H}{k_r} \right) \frac{d\epsilon}{dt} = \frac{\mu_o \ln(L) Q}{2\pi(H + h\phi)} \left(\frac{1}{k_g} - \frac{\phi}{k_r} \right) + (P_{c,r} - P_{c,g}). \quad (5.19)$$

Since the coefficient in front of $d\epsilon/dt$ is always positive, the perturbation will grow if:

$$\frac{\mu_o \ln(L) Q}{2\pi(H + h\phi)} \left(\frac{1}{k_g} - \frac{\phi}{k_r} \right) + (P_{c,r} - P_{c,g}) > 0. \tag{5.20}$$

Thus we obtain the critical flow rate:

$$Q^* = \frac{(P_{c,r} - P_{c,g})(2\pi(H + h\phi))}{\mu_o \ln(L) \left(\frac{\phi}{k_r} - \frac{1}{k_g} \right)}, \tag{5.21}$$

which could be written in the form of capillary number:

$$\mathrm{Ca}^* = \frac{(P_{c,r} - P_{c,g})\mu_o}{\mu_o \ln(L) \left(\frac{\phi}{k_r} - \frac{1}{k_g} \right) x_0 \gamma}. \tag{5.22}$$

Chapter 6

Summary and future work

In this Thesis, we combine laboratory experiments, mathematical modeling and hydrodynamic theories to investigate fluid-fluid displacement in porous media on both microscopic and macroscopic scales. While we have made several exciting new discoveries, we have arrived at observations that merit further investigation. In this chapter, we summarize our results and outline interesting next steps.

Part I of this Thesis focuses on the dynamics of moving interface and contact line at the scale of a single capillary.

In chapter 2, we present a phase-field model with a self-consistent formulation of fluid-solid surface energy and a formulation to account for the nonequilibrium conditions near the contact line. We demonstrate the ability of our model to simulate both static and dynamic configurations of two-phase flow in a capillary tube, including equilibrium slugs, spontaneous imbibition, wetting transition and interface pinch-off. The following items would be interesting extensions of our phase-field model:

1 Our phase-field model could be used to establish a phase diagram of fluid-fluid displacement patterns in the partial wetting regime in terms of three dimensionless parameters: wettability (θ_e), viscosity ratio (η) and capillary number (Ca). Specifically, we will quantify the critical Ca that leads to the onset of the wetting transition as a function of η and θ_e. This effort will advance our understanding of pore-scale displacements. Moreover, we will characterize the

interface pinch-off and bubble formation beyond the wetting transition, which have a direct application to the generation of droplets/bubbles/emulsions in microfluidic devices (Agresti *et al.*, 2010; Anna, 2016).

2 The nonequilibrium boundary condition in our phase-field model introduces a model parameter $\mathcal{S}$ that controls the relaxation time of fluid-fluid interfaces near the solid wall. Here we find the value of this parameter through the comparison with the experiment at one wettability condition $\theta_e = 112°$. The next step is to better constrain this parameter for a wide range of wettabilities.

In Chapter 3, we experimentally and theoretically study the shape of a moving interface in a prewetted capillary tube. We demonstrate that, in a confined geometry with a smooth surface, the wetting transition universally occurs via deformation of the interface and formation of a trailing film. We rationalize the emergence of the sharp, trailing-film type of wetting transition by means of a minimal-ingredients model that exhibits bifurcated solutions. We further provide experimental evidence that the pilot-film type of wetting transition, reported in a recent study (Levaché & Bartolo, 2014), is caused by solid surface roughness. The following discussions could serve as a guide for future work in this area:

3 The minimal-ingredients model produces bifurcated solutions at one capillary number. The upper branch of the solution leads to a more distorted fluid-fluid interface shape, compared to the lower branch. The next step here is to analyze the total energy in the system, including interfacial energy and viscous dissipation, to understand which branch is energetically more stable.

4 The static minimal-ingredients model presented here can capture the interfacial configurations below the wetting transition threshold. Beyond the wetting transition, however, the physical system is observed to be in a time-dependent state. Thus, the next step is to incorporate a time-dependent term into the theoretical model to capture the experimentally observed states.

5 We observe the pilot-film type of wetting transition in a capillary tube with rough surfaces. This observation needs detailed investigations from two points of view: (1) experimentally, the roughness inside the tube should be characterized in detail in order to understand at which roughness degree and precursor film thickness the pilot film emerges; (2) theoretically, a minimal-ingredients model should be developed that could produce the pilot-film type of wetting transition.

6 Following the above-mentioned investigations, we will incorporate surface roughness into our phase-filed model, which is expected to produce stick-slip motion at sufficiently low Ca and pilot film at sufficiently high Ca.

Part II of this Thesis investigates the influence of surface roughness on fluid-fluid displacement patterns in confined geometries. We do so by conducting experiments on patterned microfluidic cells with precisely controlled structured surface.

In chapter 4, we focus on the drainage regime. We show that surface roughness induces two types of liquid films entrained on the solid surfaces behind the displacement front: the classical Bretherton "thick film", and a new type of "thin film" that is confined within the roughness. We delineate these distinct displacement regimes in the form of a phase diagram and explore theoretically the crossovers among the regimes. We then show the different hydrodynamic regimes lead to different late-time morphologies of trapped defending fluid. The following discussion could serve as a guide for future work in this area:

7 The thin-film dewetting does not follow the classic viscous dewetting on a smooth surface (Redon *et al.*, 1991). Specifically, the thin-film dewetting velocity is not constant. The next step is to experimentally and theoretically determine the dynamics of thin-film dewetting on a structured surface.

In chapter 5, we focus on the imbibition regime. We show that roughness induces two markedly different imbibition processes: complete invasion at weak roughness and post-coating at strong roughness. We further show that the formation of a leading film stablizes the displacement front as the flow rate increases, which would otherwise—

that is, in a smooth confinement—become fractal. The following question could serve as a guide for future work in this area:

8 Our microfluidic cell is patterned with a regular array of cylindrical posts. How does the fluid-fluid displacement process change in fractured media with a more realistic (e.g., self-affine) roughness distribution?

Bibliography

Agresti, Jeremy J, Antipov, Eugene, Abate, Adam R, Ahn, Keunho, Rowat, Amy C, Baret, Jean-Christophe, Marquez, Manuel, Klibanov, Alexander M, Griffiths, Andrew D & Weitz, David A 2010 Ultrahigh-throughput screening in drop-based microfluidics for directed evolution. *Proceedings of the National Academy of Sciences* **107** (9), 4004–4009.

Akai, Takashi, Bijeljic, Branko & Blunt, Martin J 2018 Wetting boundary condition for the color-gradient lattice Boltzmann method: Validation with analytical and experimental data. *Advances in Water Resources* **116**, 56–66.

Al-Housseiny, Talal T, Tsai, Peichun A & Stone, Howard A 2012 Control of interfacial instabilities using flow geometry. *Nature Physics* **8** (10), 747–750.

Alizadeh Pahlavan, Amir, Cueto-Felgueroso, Luis, McKinley, Gareth H & Juanes, Ruben 2015 Thin films in partial wetting: internal selection of contact-line dynamics. *Physical Review Letters* **115** (3), 034502.

Almgren, Robert, Dai, Wei-Shen & Hakim, Vincent 1993 Scaling behavior in anisotropic hele-shaw flow. *Physical review letters* **71** (21), 3461.

Anderson, Daniel M, McFadden, Geoffrey B & Wheeler, Adam A 1998 Diffuse-interface methods in fluid mechanics. *Annual Review of Fluid Mechanics* **30** (1), 139–165.

Anna, Shelley Lynn 2016 Droplets and bubbles in microfluidic devices. *Annual Review of Fluid Mechanics* **48** (1), 285–309.

Aussillous, Pascale & Quéré, David 2000 Quick deposition of a fluid on the wall of a tube. *Physics of Fluids* **12** (10), 2367–2371.

Bazant, Martin Z, Choi, Jaehyuk & Davidovitch, Benny 2003 Dynamics of conformal maps for a class of non-laplacian growth phenomena. *Physical Review Letters* **91** (4), 045503.

Bell, James Munsie & Cameron, FK 1906 The flow of liquids through capillary spaces. *The Journal of Physical Chemistry* **50** (8), 658–674.

Ben-Jacob, Eshel, Deutscher, G, Garik, Peter, Goldenfeld, Nigel D & Lareah, Y 1986 Formation of a dense branching morphology in interfacial growth. *Physical review letters* **57** (15), 1903.

Ben-Jacob, Eshel & Garik, Peter 1990 The formation of patterns in non-equilibrium growth. *Nature* **343** (6258), 523–530.

Ben Said, Marouen, Selzer, Michael, Nestler, Britta, Braun, Daniel, Greiner, Christian & Garcke, Harald 2014 A phase-field approach for wetting phenomena of multiphase droplets on solid surfaces. *Langmuir* **30** (14), 4033–4039.

Benzi, R, Sbragaglia, M, Bernaschi, M & Succi, S 2011 Phase-field model of long-time glasslike relaxation in binary fluid mixtures. *Physical Review Letters* **106** (16), 164501.

Bico, Jose & Quéré, David 2002 Rise of liquids and bubbles in angular capillary tubes. *Journal of colloid and Interface Science* **247** (1), 162–166.

Bischofberger, Irmgard, Ramachandran, Radha & Nagel, Sidney R 2014 Fingering versus stability in the limit of zero interfacial tension. *Nature Communications* **5** (1), 1–6.

Brakke, Kenneth A 1992 The surface evolver. *Experimental Mathematics* **1** (2), 141–165.

Bretherton, Francis Patton 1961 The motion of long bubbles in tubes. *Journal of Fluid Mechanics* **10** (2), 166–188.

Briant, AJ, Wagner, AJ & Yeomans, JM 2004 Lattice Boltzmann simulations of contact line motion. I. Liquid-gas systems. *Physical Review E* **69** (3), 031602.

Briant, AJ & Yeomans, JM 2004 Lattice Boltzmann simulations of contact line motion. II. Binary fluids. *Physical Review E* **69** (3), 031603.

Buka, Agnes, Kertész, János & Vicsek, Tamás 1986 Transitions of viscous fingering patterns in nematic liquid crystals. *Nature* **323** (6087), 424–425.

Cahn, John W 1977 Critical point wetting. *The Journal of Chemical Physics* **66** (8), 3667–3672.

Cahn, John W & Hilliard, John E 1958 Free energy of a nonuniform system. I. Interfacial free energy. *The Journal of Chemical Physics* **28** (2), 258–267.

Carlson, Andreas, Do-Quang, Minh & Amberg, Gustav 2009 Modeling of dynamic wetting far from equilibrium. *Physics of Fluids* **21** (12), 121701.

Carlson, Andreas, Do-Quang, Minh & Amberg, Gustav 2011 Dissipation in rapid dynamic wetting. *Journal of Fluid Mechanics* **682**, 213–240.

Chan, Tak Shing, Snoeijer, Jacco H & Eggers, Jens 2012 Theory of the forced wetting transition. *Physics of Fluids* **24** (7), 072104.

Chan, Tak Shing, Srivastava, S, Marchand, A, Andreotti, B, Biferale, L, Toschi, F & Snoeijer, Jacobus Hendrikus 2013 Hydrodynamics of air entrainment by moving contact lines. *Physics of Fluids* **25** (7), 074105.

Chen, Jing-Den & Wilkinson, David 1985 Pore-scale viscous fingering in porous media. *Physical Review Letters* **55** (18), 1892.

Cieplak, Marek & Robbins, Mark O 1988 Dynamical transition in quasistatic fluid invasion in porous media. *Physical review letters* **60** (20), 2042.

Cieplak, Marek & Robbins, Mark O 1990 Influence of contact angle on quasistatic fluid invasion of porous media. *Physical Review B* **41** (16), 11508.

Cirillo, Emilio NM, Ianiro, Nicoletta & Sciarra, Giulio 2016 Compacton formation under Allen–Cahn dynamics. *Proceedings of the Royal Society A: Mathematical, Physical and Engineering Sciences* **472** (2188), 20150852.

Couder, Y, Cardoso, O, Dupuy, D, Tavernier, P & Thom, W 1986 Dendritic growth in the saffman-taylor experiment. *Europhysics Letters* **2** (6), 437.

Cox, RG 1986 The dynamics of the spreading of liquids on a solid surface. Part 1. Viscous flow. *Journal of Fluid Mechanics* **168**, 169–194.

Cueto-Felgueroso, Luis & Juanes, Ruben 2008 Nonlocal interface dynamics and pattern formation in gravity-driven unsaturated flow through porous media. *Physical Review Letters* **101** (24), 244504.

Cueto-Felgueroso, Luis & Juanes, Ruben 2012 Macroscopic phase-field model of partial wetting: bubbles in a capillary tube. *Physical Review Letters* **108** (14), 144502.

Cueto-Felgueroso, Luis & Juanes, Ruben 2014 A phase-field model of two-phase hele-shaw flow. *Journal of Fluid Mechanics* **758**, 522–552.

Daccord, Gerard, Nittmann, Johann & Stanley, H Eugene 1986 Radial viscous fingers and diffusion-limited aggregation: Fractal dimension and growth sites. *Physical Review Letters* **56** (4), 336–339.

De Gennes, Pierre-Gilles, Brochard-Wyart, Françoise, Quéré, David & others 2004 *Capillarity and wetting phenomena: drops, bubbles, pearls, waves*. Springer.

Delannoy, Joachim, Lafon, Suzanne, Koga, Yukina, Reyssat, Étienne & Quéré, David 2019 The dual role of viscosity in capillary rise. *Soft Matter* **15** (13), 2757–2761.

DiCarlo, David A 2013 Stability of gravity-driven multiphase flow in porous media: 40 years of advancements. *Water Resources Research* **49** (8), 4531–4544.

Diewald, Felix, Kuhn, Charlotte, Heier, Michaela, Horsch, Martin, Langenbach, Kai, Hasse, Hans & Müller, Ralf 2017 Surface wetting with droplets: A phase field approach. *Proceedings in Applied Mathematics and Mechanics* **17** (1), 501–502.

Ding, Hang & Spelt, Peter DM 2007 Wetting condition in diffuse interface simulations of contact line motion. *Physical Review E* **75** (4), 046708.

Dubé, M, Rost, M, Elder, KR, Alava, Mikko, Majaniemi, S & Ala-Nissila, T 1999 Liquid conservation and nonlocal interface dynamics in imbibition. *Physical review letters* **83** (8), 1628.

Duda, Artur, Koza, Zbigniew & Matyka, Maciej 2011 Hydraulic tortuosity in arbitrary porous media flow. *Physical Review E* **84** (3), 036319.

Eggers, Jens 2004 Hydrodynamic theory of forced dewetting. *Physical Review Letters* **93** (9), 094502.

Eggers, Jens 2005 Existence of receding and advancing contact lines. *Physics of Fluids* **17** (8), 082106.

Esmaeilzadeh, Soheil, Qin, Zhipeng, Riaz, Amir & Tchelepi, Hamdi A 2020 Wettability and capillary effects: Dynamics of pinch-off in unconstricted straight capillary tubes. *Physical Review E* **102** (2), 023109.

Fan, Lewen, Fang, Haiping & Lin, Zhifang 2001 Simulation of contact line dynamics in a two-dimensional capillary tube by the lattice Boltzmann model. *Physical Review E* **63** (5), 051603.

Fermigier, Marc & Jenffer, Patrice 1991 An experimental investigation of the dynamic contact angle in liquid-liquid systems. *Journal of Colloid and Interface Science* **146** (1), 226–241.

Gao, Peng, Liu, Ao, Feng, James J, Ding, Hang & Lu, Xi-Yun 2019*a* Forced dewetting in a capillary tube. *Journal of Fluid Mechanics* **859**, 308–320.

Gao, Tao, Mirzadeh, Mohammad, Bai, Peng, Conforti, Kameron M & Bazant, Martin Z 2019*b* Active control of viscous fingering using electric fields. *Nature Communications* **10** (1), 1–8.

de Gennes, Pierre-Gilles 1980 Dynamics of fluctuations and spinodal decomposition in polymer blends. *The Journal of Chemical Physics* **72** (9), 4756–4763.

Gennes, Pierre-Gilles, Brochard-Wyart, Françoise, Quéré, David & others 2004 *Capillarity and wetting phenomena: drops, bubbles, pearls, waves*. Springer.

Geromichalos, Dimitrios, Mugele, Frieder & Herminghaus, Stephan 2002 Nonlocal dynamics of spontaneous imbibition fronts. *Physical review letters* **89** (10), 104503.

Giefer, P, Kyrloglou, A & Fritsching, U 2023 Impact of wettability on interface deformation and droplet breakup in microcapillaries. *Physics of Fluids* **35** (4), 042110.

Godbey, R, Goldenfeld, Nigel D, Koplik, J, Levine, H, Mueller, T & Sander, LM 1985 Experimental demonstration of the role of anisotropy in interfacial pattern formation. *Physical review letters* **55** (12), 1315.

Grier, D, Ben-Jacob, E, Clarke, Roy & Sander, L-M_ 1986 Morphology and microstructure in electrochemical deposition of zinc. *Physical review letters* **56** (12), 1264.

Grier, David G, Kessler, David A & Sander, LM 1987 Stability of the dense radial morphology in diffusive pattern formation. *Physical review letters* **59** (20), 2315.

He, Shanjin, Kahanda, Galathara LMKS & Wong, Po-zen 1992 Roughness of wetting fluid invasion fronts in porous media. *Physical review letters* **69** (26), 3731.

Herminghaus, Stephan 2000 Roughness-induced non-wetting. *EPL (Europhysics Letters)* **52** (2), 165.

Hill, David E & Parlange, J-Y 1972 Wetting front instability in layered soils. *Soil Science Society of America Journal* **36** (5), 697–702.

Hoffman, Richard L 1975 A study of the advancing interface. I. Interface shape in liquid – gas systems. *Journal of Colloid and Interface Science* **50** (2), 228–241.

Hoffman, Richard L 1983 A study of the advancing interface: II. Theoretical prediction of the dynamic contact angle in liquid-gas systems. *Journal of Colloid and Interface Science* **94** (2), 470–486.

Holtzman, Ran & Segre, Enrico 2015 Wettability stabilizes fluid invasion into porous media via nonlocal, cooperative pore filling. *Physical Review Letters* **115** (16), 164501.

Homsy, George M 1987 Viscous fingering in porous media. *Annual Review of Fluid Mechanics* **19** (1), 271–311.

Huang, Rongzong, Li, Qing & Adams, Nikolaus A 2022 Surface thermodynamics and wetting condition in the multiphase lattice Boltzmann model with self-tuning equation of state. *Journal of Fluid Mechanics* **940**, A46.

Huh, C & Mason, SG 1977 The steady movement of a liquid meniscus in a capillary tube. *Journal of Fluid Mechanics* **81** (3), 401–419.

Huh, Chun & Scriven, L. E. 1971 Hydrodynamic model of steady movement of a solid/liquid/fluid contact line. *Journal of Colloid and Interface Science* **35** (1), 85–101.

Jacqmin, David 1999 Calculation of two-phase Navier–Stokes flows using phase-field modeling. *Journal of Computational Physics* **155** (1), 96–127.

Jacqmin, David 2000 Contact-line dynamics of a diffuse fluid interface. *Journal of Fluid Mechanics* **402**, 57–88.

Jasnow, David & Vinals, Jorge 1996 Coarse-grained description of thermo-capillary flow. *Physics of Fluids* **8** (3), 660–669.

Joseph, Pierre & Tabeling, Patrick 2005 Direct measurement of the apparent slip length. *Physical Review E* **71** (3), 035303.

Juel, Anne, Pihler-Puzović, Draga & Heil, Matthias 2018 Instabilities in blistering. *Annual Review of Fluid Mechanics* **50** (1), 691–714.

Kamrin, Ken, Bazant, Martin Z & Stone, Howard A 2010 Effective slip boundary conditions for arbitrary periodic surfaces: the surface mobility tensor. *Journal of Fluid Mechanics* **658**, 409–437.

Kang, Qinjun, Zhang, Dongxiao & Chen, Shiyi 2004 Immiscible displacement in a channel: simulations of fingering in two dimensions. *Advances in Water Resources* **27** (1), 13–22.

Keiser, Ludovic, Keiser, Armelle, L'estimé, Manon, Bico, José & Reyssat, Étienne 2019 Motion of viscous droplets in rough confinement: paradoxical lubrication. *Physical Review Letters* **122** (7), 074501.

Kim, Junseok 2005 A continuous surface tension force formulation for diffuse-interface models. *Journal of Computational Physics* **204** (2), 784–804.

Klaseboer, Evert, Gupta, Raghvendra & Manica, Rogerio 2014 An extended Bretherton model for long taylor bubbles at moderate capillary numbers. *Physics of Fluids* **26** (3), 032107.

Krevor, Samuel, De Coninck, Heleen, Gasda, Sarah E, Ghaleigh, Navraj Singh, de Gooyert, Vincent, Hajibeygi, Hadi, Juanes, Ruben, Neufeld, Jerome, Roberts, Jennifer J & Swennenhuis, Floris 2023 Subsurface carbon dioxide and hydrogen storage for a sustainable energy future. *Nature Reviews Earth & Environment* **4** (2), 102–118.

Kusumaatmaja, Halim, Hemingway, Ewan J & Fielding, Suzanne M 2016 Moving contact line dynamics: from diffuse to sharp interfaces. *Journal of Fluid Mechanics* **788**, 209–227.

Kusumaatmaja, H & Yeomans, JM 2007 Modeling contact angle hysteresis on chemically patterned and superhydrophobic surfaces. *Langmuir* **23** (11), 6019–6032.

Langer, James S 1980 Instabilities and pattern formation in crystal growth. *Reviews of modern physics* **52** (1), 1.

Latva-Kokko, M & Rothman, Daniel H 2005 Static contact angle in lattice Boltzmann models of immiscible fluids. *Physical Review E* **72** (4), 046701.

Latva-Kokko, M & Rothman, Daniel H 2007 Scaling of dynamic contact angles in a Lattice-Boltzmann model. *Physical Review Letters* **98** (25), 254503.

Ledesma-Aguilar, Rodrigo, Hernández-Machado, Aurora & Pagonabarraga, Ignacio 2013 Theory of wetting-induced fluid entrainment by advancing contact lines on dry surfaces. *Physical Review Letters* **110** (26), 264502.

Lee, Hyundo, Gupta, Ankur, Hatton, T Alan & Doyle, Patrick S 2017 Creating isolated liquid compartments using photopatterned obstacles in microfluidics. *Physical Review Applied* **7** (4), 044013.

Lenormand, Roland, Touboul, Eric & Zarcone, Cesar 1988 Numerical models and experiments on immiscible displacements in porous media. *Journal of Fluid Mechanics* **189**, 165–187.

Lenormand, Roland, Zarcone, Cesar & Sarr, A 1983 Mechanisms of the displacement of one fluid by another in a network of capillary ducts. *Journal of Fluid Mechanics* **135**, 337–353.

Levaché, Bertrand & Bartolo, Denis 2014 Revisiting the Saffman-Taylor experiment: imbibition patterns and liquid-entrainment transitions. *Physical Review Letters* **113** (4), 044501.

Li, Shuwang, Lowengrub, John S, Fontana, Jake & Palffy-Muhoray, Peter 2009 Control of viscous fingering patterns in a radial hele-shaw cell. *Physical Review Letters* **102** (17), 174501.

Lindner, Anke, Bonn, Daniel, Poiré, Eugenia Corvera, Amar, Martine Ben & Meunier, Jacques 2002 Viscous fingering in non-newtonian fluids. *Journal of Fluid Mechanics* **469**, 237–256.

Lu, Nancy B, Amchin, Daniel B & Datta, Sujit S 2021 Forced imbibition in stratified porous media: Fluid dynamics and breakthrough saturation. *Physical Review Fluids* **6** (11), 114007.

Lu, Nancy B, Pahlavan, Amir A, Browne, Christopher A, Amchin, Daniel B, Stone, Howard A & Datta, Sujit S 2020 Forced imbibition in stratified porous media. *Physical Review Applied* **14** (5), 054009.

Lucas, Richard 1918 Ueber das Zeitgesetz des kapillaren Aufstiegs von Flüssigkeiten. *Kolloid-Zeitschrift* **23** (1), 15–22.

Magaletti, F, Picano, Francesco, Chinappi, M, Marino, Luca & Casciola, Carlo Massimo 2013 The sharp-interface limit of the Cahn–Hilliard/Navier–Stokes model for binary fluids. *Journal of Fluid Mechanics* **714**, 95–126.

Måløy, Knut Jørgen, Feder, Jens & Jøssang, Torstein 1985 Viscous fingering fractals in porous media. *Physical Review Letters* **55** (24), 2688.

Meakin, Paul & Tartakovsky, Alexandre M 2009 Modeling and simulation of pore-scale multiphase fluid flow and reactive transport in fractured and porous media. *Reviews of Geophysics* **47** (3), RG3002.

Mirzadeh, Mohammad & Bazant, Martin Z 2017 Electrokinetic control of viscous fingering. *Physical review letters* **119** (17), 174501.

Odier, Céleste, Levaché, Bertrand, Santanach-Carreras, Enric & Bartolo, Denis 2017 Forced imbibition in porous media: A fourfold scenario. *Physical Review Letters* **119** (20), 208005.

Oron, Alexander, Davis, Stephen H & Bankoff, S George 1997 Long-scale evolution of thin liquid films. *Reviews of Modern Physics* **69** (3), 931.

Orr Jr, FM & Taber, JJ 1984 Use of carbon dioxide in enhanced oil recovery. *Science* **224** (4649), 563–569.

Pahlavan, A Alizadeh, Cueto-Felgueroso, L, Hosoi, Anette E, McKinley, Gareth H & Juanes, Ruben 2018 Thin films in partial wetting: Stability, dewetting and coarsening. *Journal of Fluid Mechanics* **845**, 642–681.

Pahlavan, Amir Alizadeh, Cueto-Felgueroso, Luis, McKinley, Gareth H & Juanes, Ruben 2015 Thin films in partial wetting: internal selection of contact-line dynamics. *Physical Review Letters* **115** (3), 034502.

Pahlavan, Amir A, Stone, Howard A, McKinley, Gareth H & Juanes, Ruben 2019 Restoring universality to the pinch-off of a bubble. *Proceedings of the National Academy of Sciences* **116** (28), 13780–13784.

Paterson, Lincoln 1981 Radial fingering in a hele shaw cell. *Journal of Fluid Mechanics* **113**, 513–529.

Pihler-Puzović, D, Illien, Pierre, Heil, Matthias & Juel, Anne 2012 Suppression of complex fingerlike patterns at the interface between air<? format?> and a viscous fluid by elastic membranes. *Physical review letters* **108** (7), 074502.

Popescu, Mihail Nicolae, Ralston, John & Sedev, Rossen 2008 Capillary rise with velocity-dependent dynamic contact angle. *Langmuir* **24** (21), 12710–12716.

Priezjev, Nikolai V 2007 Effect of surface roughness on rate-dependent slip in simple fluids. *The Journal of Chemical Physics* **127** (14), 144708.

Primkulov, BK, Chui, JYY, Pahlavan, AA, MacMinn, CW & Juanes, R 2020*a* Characterizing dissipation in fluid-fluid displacement using constant-rate spontaneous imbibition. *Physical Review Letters* **125** (17), 174503.

Primkulov, BK, Pahlavan, AA, Bourouiba, Lydia, Bush, John WM & Juanes, Ruben 2020*b* Spin coating of capillary tubes. *Journal of Fluid Mechanics* **886**, A30.

Primkulov, Bauyrzhan K, Pahlavan, Amir A, Fu, Xiaojing, Zhao, Benzhong, MacMinn, Christopher W & Juanes, Ruben 2021 Wettability and lenormand's diagram. *Journal of Fluid Mechanics* **923**, A34.

Primkulov, Bauyrzhan K, Talman, Stephen, Khaleghi, Keivan, Rangriz Shokri, Alireza, Chalaturnyk, Rick, Zhao, Benzhong, MacMinn, Christopher W & Juanes, Ruben 2018 Quasistatic fluid-fluid displacement in porous media: Invasion-percolation through a wetting transition. *Physical Review Fluids* **3** (10), 104001.

Prokopev, Sergei, Vorobev, Anatoliy & Lyubimova, Tatiana 2019 Phase-field modeling of an immiscible liquid-liquid displacement in a capillary. *Physical Review E* **99** (3), 033113.

Qian, Tiezheng, Qiu, Chunyin & Sheng, Ping 2008 A scaling approach to the derivation of hydrodynamic boundary conditions. *Journal of Fluid Mechanics* **611**, 333–364.

Qian, Tiezheng, Wang, Xiao-Ping & Sheng, Ping 2003 Molecular scale contact line hydrodynamics of immiscible flows. *Physical Review E* **68** (1), 016306.

Qian, Tiezheng, Wang, Xiao-Ping & Sheng, Ping 2004 Power-law slip profile of the moving contact line in two-phase immiscible flows. *Physical Review Letters* **93** (9), 094501.

Qian, Tiezheng, Wang, Xiao-Ping & Sheng, Ping 2006 A variational approach to moving contact line hydrodynamics. *Journal of Fluid Mechanics* **564**, 333–360.

Qiu, Yu, Xu, Ke, Pahlavan, Amir A & Juanes, Ruben 2023 Wetting transition and fluid trapping in a microfluidic fracture. *Proceedings of the National Academy of Sciences* **120** (22), e2303515120.

Queralt-Martín, María, Pradas, M, Rodríguez-Trujillo, Romen, Arundell, M, Poiré, E Corvera & Hernández-Machado, Aurora 2011 Pinning and avalanches in hydrophobic microchannels. *Physical Review Letters* **106** (19), 194501.

Quéré, David 2002 Fakir droplets. *Nature Materials* **1** (1), 14–15.

Quéré, David 2008 Wetting and roughness. *Annual Review of Materials Research* **38** (1), 71–99.

Redon, C, Brochard-Wyart, F & Rondelez, F 1991 Dynamics of dewetting. *Physical Review Letters* **66** (6), 715.

Rothstein, Jonathan P 2010 Slip on superhydrophobic surfaces. *Annual review of fluid mechanics* **42**, 89–109.

Ruiz-Gutiérrez, Élfego, Armstrong, Steven, Lévêque, Simon, Michel, Célestin, Pagonabarraga, Ignacio, Wells, Gary G, Hernández-Machado, Aurora & Ledesma-Aguilar, Rodrigo 2022 The long cross-over dynamics of capillary imbibition. *Journal of Fluid Mechanics* **939**, A39.

Saffman, Philip Geoffrey & Taylor, Geoffrey Ingram 1958 The penetration of a fluid into a porous medium or Hele-Shaw cell containing a more viscous liquid. *Proceedings of the Royal Society of London. Series A. Mathematical and Physical Sciences* **245** (1242), 312–329.

Sarkar, Subir K & Jasnow, David 1989 Viscous fingering in an anisotropic hele-shaw cell. *Physical Review A* **39** (10), 5299.

Sawada, Yasuji, Dougherty, A & Gollub, Jerry P 1986 Dendritic and fractal patterns in electrolytic metal deposits. *Physical review letters* **56** (12), 1260.

Seiwert, Jacopo, Clanet, Christophe & Quéré, David 2011 Coating of a textured solid. *Journal of Fluid Mechanics* **669**, 55–63.

Seppecher, Pierre 1996 Moving contact lines in the Cahn-Hilliard theory. *International Journal of Engineering Science* **34** (9), 977–992.

Siebold, Alain, Nardin, Michel, Schultz, Jacques, Walliser, André & Oppliger, Max 2000 Effect of dynamic contact angle on capillary rise phenomena. *Colloids and Surfaces A: Physicochemical and Engineering Aspects* **161** (1), 81–87.

Snoeijer, Jacco H 2006 Free-surface flows with large slopes: Beyond lubrication theory. *Physics of Fluids* **18** (2), 021701.

Snoeijer, Jacco H & Andreotti, Bruno 2013 Moving contact lines: scales, regimes, and dynamical transitions. *Annual Review of Fluid Mechanics* **45** (1), 269–292.

Snoeijer, Jacco H, Delon, Giles, Fermigier, Marc & Andreotti, Bruno 2006 Avoided critical behavior in dynamically forced wetting. *Physical Review Letters* **96** (17), 174504.

Soriano, J, Mercier, A, Planet, R, Hernández-Machado, A, Rodríguez, MA & Ortín, J 2005 Anomalous roughening of viscous fluid fronts in spontaneous imbibition. *Physical review letters* **95** (10), 104501.

Soriano, J, Ramasco, JJ, Rodríguez, MA, Hernández-Machado, A & Ortín, J 2002 Anomalous roughening of hele-shaw flows with quenched disorder. *Physical review letters* **89** (2), 026102.

Spelt, Peter DM 2005 A level-set approach for simulations of flows with multiple moving contact lines with hysteresis. *Journal of Computational physics* **207** (2), 389–404.

Stokes, JP, Weitz, DA, Gollub, Jerry P, Dougherty, A, Robbins, MO, Chaikin, PM & Lindsay, HM 1986 Interfacial stability of immiscible displacement in a porous medium. *Physical Review Letters* **57** (14), 1718.

Stone, HA, Stroock, Abraham D & Ajdari, A 2004 Engineering flows in small devices. *Annual Review of Fluid Mechanics* **36** (1), 381–411.

Sui, Yi, Ding, Hang & Spelt, Peter DM 2014 Numerical simulations of flows with moving contact lines. *Annual Review of Fluid Mechanics* **46**, 97–119.

Szulczewski, Michael L, MacMinn, Christopher W, Herzog, Howard J & Juanes, Ruben 2012 Lifetime of carbon capture and storage as a climate-change mitigation technology. *Proceedings of the National Academy of Sciences* **109** (14), 5185–5189.

Utter, B, Ragnarsson, R & Bodenschatz, E 2001 Alternating tip splitting in directional solidification. *Physical review letters* **86** (20), 4604.

Verschueren, Maykel, Van De Vosse, FN & Meijer, HEH 2001 Diffuse-interface modelling of thermocapillary flow instabilities in a Hele-Shaw cell. *Journal of Fluid Mechanics* **434**, 153–166.

Vinogradova, Olga I & Belyaev, Aleksey V 2011 Wetting, roughness and flow boundary conditions. *Journal of Physics: Condensed Matter* **23** (18), 184104.

Voinov, OV 1976 Hydrodynamics of wetting. *Fluid Dynamics* **11** (5), 714–721.

Wang, Xiao-Ping, Qian, Tiezheng & Sheng, Ping 2008 Moving contact line on chemically patterned surfaces. *Journal of Fluid Mechanics* **605**, 59–78.

Washburn, Edward W 1921 The dynamics of capillary flow. *Physical Review* **17** (3), 273.

Weislogel, Mark M & Lichter, Seth 1998 Capillary flow in an interior corner. *Journal of Fluid Mechanics* **373**, 349–378.

Wenzel, Robert N 1936 Resistance of solid surfaces to wetting by water. *Industrial & Engineering Chemistry* **28** (8), 988–994.

Whitesides, George M 2006 The origins and the future of microfluidics. *Nature* **442** (7101), 368–373.

Witelski, Thomas P 1998 Equilibrium interface solutions of a degenerate singular Cahn-Hilliard equation. *Applied Mathematics Letters* **11** (5), 127–133.

Wu, Pingkeng, Nikolov, Alex D & Wasan, Darsh T 2017 Capillary rise: validity of the dynamic contact angle models. *Langmuir* **33** (32), 7862–7872.

Yan, YY & Zu, YQ 2007 A lattice Boltzmann method for incompressible two-phase flows on partial wetting surface with large density ratio. *Journal of Computational Physics* **227** (1), 763–775.

Yang, C, Tartaglino, U & Persson, BNJ 2006 Influence of surface roughness on superhydrophobicity. *Physical Review Letters* **97** (11), 116103.

Yang, XG, Zhang, FY, Lubawy, AL & Wang, CY 2004 Visualization of liquid water transport in a pefc. *Electrochemical and Solid-State Letters* **7** (11), A408.

Yokoyama, Jun, Kitagawa, Yoshiyuki, Yamada, Hideaki & Matsushita, Mitsugu 1994 Dendritic growth of viscous fingers under linear anisotropy. *Physica A: Statistical Mechanics and its Applications* **204** (1-4), 789–799.

Yue, Pengtao & Feng, James J 2011 Wall energy relaxation in the Cahn–Hilliard model for moving contact lines. *Physics of Fluids* **23** (1), 012106.

Yue, Pengtao, Zhou, Chunfeng & Feng, James J 2010 Sharp-interface limit of the Cahn–Hilliard model for moving contact lines. *Journal of Fluid Mechanics* **645**, 279–294.

Zhang, Jiaqi & Yue, Pengtao 2020 A level-set method for moving contact lines with contact angle hysteresis. *Journal of Computational Physics* **418**, 109636.

Zhang, Qing, Amooie, Amin, Bazant, Martin Z & Bischofberger, Irmgard 2021 Growth morphology and symmetry selection of interfacial instabilities in anisotropic environments. *Soft Matter* **17** (5), 1202–1209.

Zhang, Qing, Zhou, Shuang, Zhang, Rui & Bischofberger, Irmgard 2023 Dendritic patterns from shear-enhanced anisotropy in nematic liquid crystals. *Science Advances* **9** (2), eabq6820.

Zhao, Benzhong, MacMinn, Christopher W & Juanes, Ruben 2016 Wettability control on multiphase flow in patterned microfluidics. *Proceedings of the National Academy of Sciences* **113** (37), 10251–10256.

Zhao, Benzhong, Pahlavan, Amir Alizadeh, Cueto-Felgueroso, Luis & Juanes, Ruben 2018 Forced wetting transition and bubble pinch-off in a capillary tube. *Physical Review Letters* **120** (8), 084501.

Zheng, Zhong, Kim, Hyoungsoo & Stone, Howard A 2015 Controlling viscous fingering using time-dependent strategies. *Physical Review Letters* **115** (17), 174501.

Zhou, Min-Yao & Sheng, Ping 1990 Dynamics of immiscible-fluid displacement in a capillary tube. *Physical Review Letters* **64** (8), 882.

Zimmerman, Robert W & Bodvarsson, Gudmundur S 1996 Hydraulic conductivity of rock fractures. *Transport in Porous Media* **23**, 1–30.